Effects of platform-induced pitching motion on the aerodynamics of a FOWT rotor

S.B. Rengarajan

Delft University of Technology

Effects of platform-induced pitching motion on the aerodynamics of a FOWT rotor

by

S.B. Rengarajan

Student Name	Student Number
S.B. Rengarajan	5256747

Supervisors:	Prof. Carlos S. Ferreira (Supervisor)
	Dr. Wei Yu (Daily supervisor)
Committee:	Prof. Carlos S. Ferreira (Chair)
	Dr. Wei Yu (Daily Supervisor)
	Dr.ir. A.H. van Zuijlen (External)
Institution:	Delft University of Technology
Place:	Faculty of Aerospace Engineering, Delft

Preface

Anyone who has hustled on the same problem for about an year should know how tiring the process of successfully completing a thesis project is. Even though the project you work on is the most interesting thing in the world for you to do, repeating the same hustle everyday continuously for an year definitely takes a toll on your motivation levels. In such cases, constant academic and moral support from people around us will be the primary driving force. I would like to use this letter to thank the ones that stood by my side through these days and helped me conclude this project successfully.

I would first like to thank Dr. Wei Yu for her continuous support and feedback on the thesis's progress. The valueable inputs and suggestions from her side shaped up my thesis which was all over the place when I started. I would like to thank professor Carlos S. Ferreira for proposing this topic and helping me understand the research value of such a topic. Apart from the academic inputs and feedback, the vastness of the CFD software led to a lot of hiccups throughout the project. I would like to thank my Ph.D. supervisors Mr. Rention Pasolari and Mr. Anand Parinam for dedicating time amidst their already busy schedule.

More than the academic inputs, it was my morale that needed constant reinforcement. I would like to thank my parents for providing constant support throughout my time in the Netherlands which made sure to land quite a few hard blows on my confidence levels. All thanks to them that I was able to pursue this very ambitious dream of mine and make it come true despite the harsh backlashes. Lastly, I would like to thank my friends Pratyush and Sreedharan for constantly being by my side through my times of hardships and never letting my very thin thread of sanity loose.

S.B. Rengarajan
Delft, April 2023

Summary

The hunt for new methods to harness wind energy is at an all-time high as wind energy quickly overtakes other renewable energy sources. Deep waters are promising alternatives with higher average wind speed (thus, higher yields) and also due to lesser availability of land on shore. Even though the design of the blades and rotor of a FOWT is largely similar to that of onshore counterparts, they are mounted on floating platforms, unlike the fixed platforms on onshore wind turbines. Due to the excitation from wind and waves, these foundations are made to oscillate in all six degrees of freedom. As observed by [1] pitch and surge motions have the most significant effects out of all the possible types of motions. This study tries to continue the path started by [2] by simulating a pitching wind turbine using an actuator disk CFD model to comprehend the aerodynamics of a pitching rotor and compare it with that of a surging rotor. This study can also be considered a continuation of the actuator disk study of the surging motion.

The primary objective of this thesis is to understand the differences between the aerodynamics of a surging and a pitching wind turbine using an actuator disk model. To create this model, a computational domain with a dynamic mesh using Arbitrary Mesh Interface (AMI) method. The actuator disk is made to pitch sinusoidally with prescribed pitching frequency and amplitude. The cases chosen to study in this project are the same cases simulated in [2]. This gives an objective view of the differences in the aerodynamics of a pitching and a surging wind turbine. In order to identify the effects of motion and thrust prescription separately, three different types of actuator disk models were created. Using the first model, which simulates a pitching actuator disk with constant thrust, the effects of pitch motion are captured. The second model which simulates a still actuator disk with dynamic loading gives the effects of change in thrust on the rotor. The last model, which is a combination of the first two with a pitching actuator disk under dynamic loading, attempts to simulate a more realistic pitching actuator.

On comparing the surge and pitch motions of the actuator disk, the stark difference observed is the meandering in wake due to flow shear and asymmetric tip vortex shedding. At high thrust and low-frequency cases, turbulent wake states are also visible in the wake. Along with the flow shear, the tilt of the actuator disk gives rise to strong vortices that are shed normally to the flow due to a gradient in axial force on the actuator. These vortices are shed throughout the cycle and reach their highest magnitudes when the actuator is at the mean position. At higher frequencies, they are nearly as strong as the tip vortices and introduce non-linear effects on the induction field. They also tend to introduce varied dynamic responses based on the radial location. The induction field corresponding to the lower part of the actuator assumes a negative phase delay while the upper parts assume a positive phase delay. These vortices have the strongest influence when the actuator is pitching with constant thrust, with less noticeable influence when the actuator disk is pitching with dynamic thrust, and do not have a significant influence when the actuator disk is still.

On comparing the induction field predicted using CFD method with the dynamic inflow model [3], it can be seen that whenever the influence of the vortices that arise due to the load imbalance is high, the CFD results deviate from dynamic inflow results. Similar behaviour is observed when they are compared with the surge results. Except for timestamps when the actuator disk is in the mean position, the magnitude of the induction field corresponding to the pitching cases is higher than the surging cases. Therefore, when a dynamic inflow model needs to be designed for a pitching FOWT, it is very important to take the effect of these vortices into account.

Even though actuator disk results provide a representative view of the pitching dynamics, it is recommended to use an actuator line model with airfoil data to properly capture the effects of these vortices and their influence on the induction field. When an actuator line with airfoil data is used, its influence on inflow angle, the loading on the actuator, and thus the strength of these vortices can be more accurately captured.

Thus, this project provides a comprehensive view of the effects of platform pitching motion on a FOWT and its differences with respect to the surging dynamics. This project also confirms that an actuator disc model is capable of reproducing the effects of pitching in a FOWT. Using the insights provided in this thesis, a better dynamic inflow can be developed for use in industries.

Contents

Nomenclature

Abbreviations

Abbreviation	Definition
TWS	Turbulent Wake State
VRS	Vortex Ring State
PIV	Particle Image Velocimetry
BEMT	Blade Element Momentum Theory
GDW	General Dynamic Wake
VLM	Vortex Lattice Model
FVM	Free Vortex Model
SFVM	Semi Free Vortex Model
CFD	Computational Fluid Dynamics
AoA	Angle of Attack
DNS	Direct Numerical Simulations
LES	Large Eddy Simulations
RANS	Reynolds Averaged Navier Stokes
RPM	Rotations Per Minute
CD	Computational Domain
SST	Shear Stress Transport

Symbols

Symbol	Definition	Unit
U_∞	Freestream Velocity	[m/s]
U_r	Velocity at rotor	[m/s]
R	Radius of wind turbine rotor	[m]
r	Radial position of blade element	[m]
B	Number of blades	[-]
C_T	Thrust coefficient	[-]
C_P	Power coefficient	[-]
f_{tip}	Prandtl tip loss factor	[-]
f_{hub}	Prandtl hub loss factor	[-]
a	Axial induction factor	[-]
a'	Tangential induction factor	[-]
W	Relative velocity w.r.t. blade cross section	[m/s]
K	Coleman constant (factor of non-uniform induction)	[-]
A_p	Amplitude of platform pitching	[^{o}]
H_{hub}	Hub height	[m]
Re	Reynolds number	[-]
F	External force field	[N]
α	Angle of attack	[^{o}]
ρ	Density of flow	[kg/m^3]
λ	Yaw angle of incoming flow	[^{o}]
Ω	Angular velocity of rotor	[rad/s]
Ψ	Azimuthal position of blade	[^{o}]
Γ	Circulation	[-]

Symbol	Definition	Unit
ω_p	Platform pitch frequency	[Hz]
Φ	Inflow angle	[^{o}]
χ	Wake skew angle	[^{o}]

List of Figures

List of Tables

1
Introduction

Following the Paris agreement, where nations worldwide unanimously agreed to "keep the temperature rise well below 2^{o}C above the pre-industrial levels"[20], the transition from non-renewable sources such as fossil fuels to renewable sources has been ever-increasing. Along with that, following the European Green deal[21], Europe wishes to become the first climate-neutral continent by 2050. With bigger milestones set year after year, the need to accelerate the pace of transitions also increases. Fortunately, we have a plethora of renewable sources to choose from, which includes wind, solar, hydro, geothermal, et cetera. Out of those, wind energy already contributes to nearly 15% of the total energy production in Europe and is also the cheapest source of energy currently[22].

With wind energy rapidly becoming a dominant source of renewable energy, the search for different opportunities and alternatives to harness energy from wind resources is peaking. Since wind turbines suffer a significant loss in power production when turbines are placed close to each other, infamously known as wake losses, wind farms take up large amounts of space with an increase in the number of wind turbines. The wind farm sites also need to be carefully chosen as wind resource quality is of primal importance for optimal energy production. We also need to take care of environmental and social factors such as noise constraints when setting up a farm onshore. This leads to lesser availability of space as wind energy gets more popular and forces engineers to look elsewhere to set up wind farms.

In contrast to on-shore resources, harnessing energy abroad has a number of benefits. The overall surface roughness at the sea surface is lower than onshore due to the lack of turbulence triggers like trees and building structures. This opens the door for several beneficial impacts on wind speeds. (as far as energy harvesting is considered). Higher and more consistent wind speeds with lower turbulence levels and zero visual or acoustic impacts on people are all characteristics of offshore sites. Since offshore wind farms are stationed literally in the middle of the sea, they might look unpractically expensive at the first glance. However, it has been proven to be more economically viable than onshore sites at certain locations [23]. Japan, China, USA, Norway, etc. come under the list of countries that show higher potential in the region of deep waters [24]. Owing to commercial viability and stressing threat due to climate change, FOWTs have attracted significant interest among researchers. In the subsequent sections of the report, a deep study of the observations made with regard to the aerodynamics of a FOWT is presented and discussed.

1.1. Technological challenges

It is the platform on which the wind turbine is mounted that distinguishes offshore wind turbines from their onshore counterparts. An offshore platform, unlike the onshore foundations, does not have a rigid connection with the ground and will be floating on the surface of the water with mooring lines fastening them to the ground to prevent drifting. The idea of using floating foundations for offshore wind turbines was first introduced by Heronemus[25], way back in 1972. However, the first ever commercial implementation of floating wind turbines was done in the year of 2007, which marks the technological complexity of these floating structures.

Since these platforms float on the water, they are not as rigid as an onshore foundation. They tend to move in all six degrees of freedom (Surge, Sway, Heave, Roll, Pitch, and Yaw)[26]. Out of these six, three motions are translational in nature. Heaving in the vertical direction, swaying in the lateral direction, and surging in the axial direction are the translatory degrees of freedom. The remaining three motions involve a rotational movement of the wind turbine structure. Yawing about the vertical axis, Pitching about the lateral axis, and rolling about the axial are the rotational degrees of freedom. Figure 1.1[4] gives a visual illustration of these six motion types for a better comprehension.

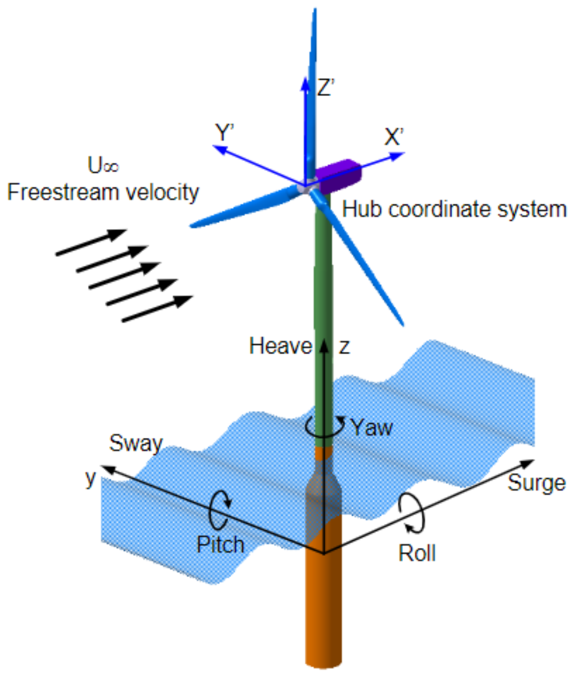

Figure 1.1: Platform motions experienced by an FOWT [4]

Since the FOWTs need to be installed in the middle of the sea, they need to mount onto floating foundations. The four popular types of floating foundations are semi-submersible platforms, spar-Buoy platforms, barge platforms, and tension-leg platforms. The inclusion of the dynamics of these floating structures while modeling the wind turbine will be beneficial so that the hydrodynamic response of the platforms due to wave excitations can also be modeled instead of prescribing them. Such research was conducted by Sebastian et al. [26], where he used an engineering aero-hydro-servo tool - FAST[27] to explicitly studied the aerodynamic, hydrodynamic, and the structural response. Since an engineering model was used in this research, the results captured cannot be entirely trusted, but it was capable of hinting that unsteady effects will arise due to platform excitation. This research on FOWTs encouraged a lot of researchers to study the aerodynamic effects that arise from research on platform motions. In the next few years, a number of researchers involved themselves in studying the effects of these unsteady aerodynamic effects using higher fidelity analyses such as [24] [28] [29] [13]. Since the idea of floating wind turbines is fairly new to the community, it is essential to understand the effects of the platform motions individually before analyzing more complex interactions.

In a study done by Lee H. et. al [30], the aerodynamic effects of individual platform motions are studied. The study concluded that not all six motions have the same effect on the performance of this rotor. Platform-induced pitching [1] and surging motions are shown to have the most significant effects on the FOWT's power and thrust response. This is because these two types of motions tend to introduce a movement in the streamwise direction. Therefore, they change the relative velocity and result in more

Table 1.1: Publications that deal with effects of pitching and surging platform motions in the near past (2016-2021)
Abbreviations: CFD - Blade-resolved CFD, FVM - Free Vortex Method, GDW - General Dynamic Wake

Publisher	Year	Turbine motion	Methodology
Ferreira C. et al.[3]	2021	Surge	SFVM
Shi W. et al.[17]	2021	Pitch	CFD
Rezaeiha and Micallef[31]	2020	Surge	CFD Actuator disk
Corniglion et al.[32]	2020	Surge	FVM, CFD-Actutator line
Schliffke et al.[33]	2020	Surge	Experimental
Ortolani et al.[19]	2020	Pitch	FAST, CFD
Mancini et al.[34]	2020	Surge	Experimental and numerical
Rodriguez and Jawors[35]	2020	Pitch	FVM
Kyle et al.[36]	2020	Surge	CFD
Kopperstad et al.[37]	2020	Surge	CFD - Actuator disk
Kim and Shin[38]	2020	Pitch, Surge	Experimental and numerical
Ahn and Shin[39]	2020	Pitch, Surge	Experimental and numerical
Fang et al.[40]	2020	Pitch	CFD
Lienard at al.[29]	2019	Pitch, Surge	CFD
Bezzina et al.[41]	2019	Surge	CFD - Actuator disk
Sant and Micallef[42]	2019	Surge	FAST, CFD - Actuator disk, GDW
Shen at al.[13]	2018	Pitch, Surge	FVM
Wen et al.[43]	2018	Pitch	FVM
Lin et al.[44]	2018	Pitch, Surge	CFD
Tran and Kim[45]	2016	Surge	CFD
Farrugia et. al[46]	2016	Surge	FVM

dynamic inflow wind speeds. This in turn affects the angle of attack and thus significantly affects the response of the rotor.

Even though both pitching and surging platform motions have gotten a similar amount of research interest in the community, pitch motion has not been studied as much as surging motion. Table 1.1 gives us an overview of major research on the aerodynamics of FOWTs subject to platform motions and the methodology used. Please note that the table contains a selected list of research done in the past and does not contain an exhaustive list of publications of platform motions. It is presented to give the reader an impression of the current FOWT research trend.

1.2. Thesis overview

Earlier in this chapter, several researchers stressed the fact that the platform motions have effects on the rotor performance which cannot be undermined. Lee H. et al. [30] presented in their research that the surge has the most significant effects on the rotor performance compared to motions in other DOFs. From Table 1.1, we can observe that the number of research done on pitching is lesser than the research done on surging motions, even though they might seem equal in number. Therefore, this thesis will focus on studying the aerodynamic effects pitching motion has on the wind turbine rotor.

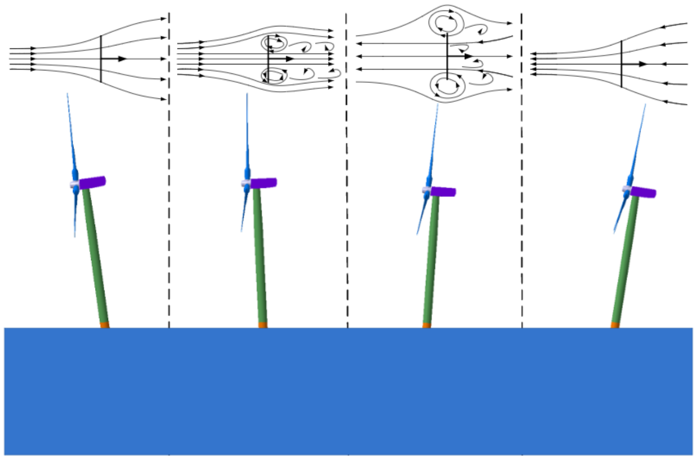

Figure 1.2: FOWT under pitching platform motions and resulting effects on wake states [5]

In this project, the main aim is to simplify and speed up the high-fidelity CFD analyses on the effects floating platform motions have on rotor aerodynamics with emphasis on the actuator's induction field and near wake aerodynamics. Since blade-resolved CFD models consume a lot of time for pre-processing, the primary aim of this project is to check the capability of actuator disk models in predicting the aerodynamics (the induction field, primarily) of a pitching wind turbine. Following that, a comparative study between the aerodynamics of a pitching actuator and a surging actuator is done. This is done to understand better the unsteady effects that arise in the case of a pitching FOWT. This study also helps us derive a dynamic inflow model for a pitching actuator disk similar to Carlos's dynamic inflow model for surging wind turbines [3]. Since tilting of the rotor is an important characteristic of a pitching wind turbine, the applicability of yaw correction models to pitching wind turbine analyses will be examined. Evaluation of BEM correction models was done because BEM tools are capable of producing useful results for industrial purposes and the theme of the thesis is to speed up the analyses of wind turbines under platform-induced motions.

1.3. Research Questions, Objectives and Sub-goals

The research goals were slightly modified as the project progressed to add more research value. Instead of trying to capture the tip effects using an actuator line model (as planned earlier), it was decided to do a deeper comparative analysis between the aerodynamics of a surging wind turbine and a pitching wind turbine and focus more on the dynamic response due to the pitching motion.

1.3.1. Research Questions

- To investigate the influence of pitching platform motion on rotor aerodynamics using actuator disk CFD model of a pitching FOWT.
  - Can these actuator disk models be utilized for studying the aerodynamics of a pitching FOWT? If that's the case, which model better predicts the aerodynamics of pitching FOWTs?
- What are the essential differences between a pitching actuator disk and a surging actuator disk with respect to the induction field and near wake aerodynamics?
  - What effect does the tilting of the actuator disk have on the aerodynamics of a pitching actuator disk?
  - Can the dynamic inflow model developed for surging wind turbines [3] be used for pitching cases also? If not, what needs to be considered for developing a new dynamic inflow model?
- How accurate are the yaw correction models to be applied for pitching actuator disk cases?

This report will present the methodology used to answer the research questions formulated above. Chapter 2 will present the crux of past researches done on similar topics. It is be followed by Chapter 3 where the process of actuator disk, actuator line and BEM correction models' model development will be explained in detail. Chapter 4 contains a discussion regarding the results obtained from actuator disk and actuator line CFD simulations. In the end, Chapter 5 will provide conclusive remarks based on the research findings and also suggestions for future work on similar subjects.

2
Literature study

This chapter starts with discussing the background study done to understand the problem and also to determine the type of tools (including the fidelity, the complexity of the model, etc.). Section 2.1 contains the description of the possible effects that can arise due to the dynamic motion of FOWTs and Section 2.2 presents the tools that are available currently to conduct the aerodynamic analyses. Following these, a discussion on the past research done on pitching wind turbines is discussed in Section 2.4. This section provides novel findings that have been brought out by the research community in an effort to understand the effects of pitch motion on FOWT's performance and aerodynamics.

2.1. Unsteady effects due to platform motions

The aerodynamics of a FOWT is fundamentally different from a HAWT that is fixed in the ground because of the unsteady effects induced by platform motions. Sebastian and Lackner [26] highlights the main differences between the inflows of a FOWT rotor and a HAWT rotor as:

- A HAWT that is fixed to the ground will mostly experience a steady inflow unless there is an inherent instability in the inflow. Even though fixed bottom HAWTs experience non-uniform effects due to external factors, a FOWT is expected to experience the combined effect of the unsteadiness in inflow and also the unsteadiness that rises because of the unsteadiness in the sea.
- Assuming that the atmospheric flow is stable enough, the platform-induced motion of the FOWT rotor leads to shear in the wind flow around the rotor. These are particularly noticeable in cases with an angular motion of the rotor such as pitching and yawing.
- Along with the wind shear, the translatory and rotatory components of the platform-induced motion give rise to changes in the magnitude and direction of wind speed. This leads to more complex rotor-wake interactions.

The following relation can be used to calculate the inflow velocity in the case of a FOWT under unsteady operating conditions is given by:

$$\mathbf{V}_{\text{inflow}} = \mathbf{V}_{\infty} - \Omega \times \mathbf{r} + \mathbf{V}_{\text{ind,wake}} + \mathbf{V}_{\text{platform}} \tag{2.1}$$

$$\begin{aligned} \mathbf{V}_{\text{platform}} = & \left(V_{\text{heave}} + \dot{\theta}_{\text{pitch}}\, z - \dot{\theta}_{\text{roll}}\, y\right) \hat{\mathbf{i}} \\ & + \left(V_{\text{sway}} + \dot{\theta}_{\text{roll}}\, x - \dot{\theta}_{\text{yaw}}\, z\right) \hat{\mathbf{j}} \\ & + \left(V_{\text{surge}} + \dot{\theta}_{\text{yaw}}\, y - \dot{\theta}_{\text{pitch}}\, x\right) \hat{\mathbf{k}} \end{aligned} \tag{2.2}$$

where $\dot{\theta}_{\text{roll}}$, $\dot{\theta}_{\text{yaw}}$, $\dot{\theta}_{\text{pitch}}$ denote the angular velocities of the corresponding rotational components of platform motions.

Along with the rotor kinematics, it is essential to know the unsteady effects that have been observed in the research done so far. The operating states of a rotor can be categorised into four. They are:

- Propeller state
- Windmill state
- Turbulent wake state
- Propeller brake state

Researchers in the past have provided multiple ways to predict the occurrence of such complex wake states. However, the popular method employed by researchers is to use the values of rotor averaged induction values. Stoddard et al. [47] were the first researchers to introduce this method to classify the wake states. Figure 2.1 shows the same classification and how the trend of rotor-averaged induction factors that correspond to these wake states. As can be seen from the figure, at $a \leq 0$, the rotor

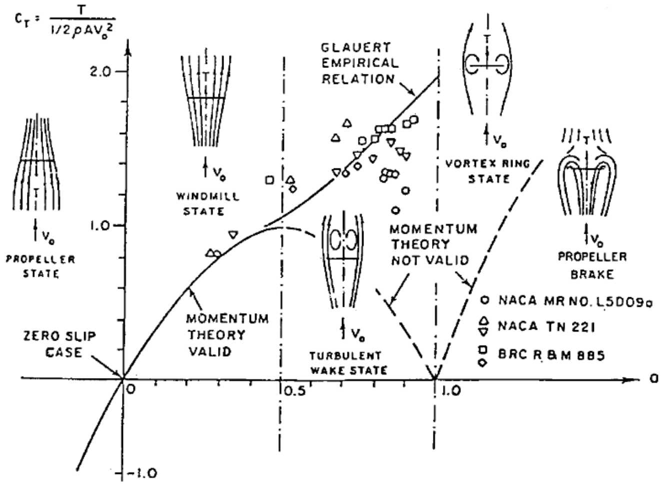

Figure 2.1: Occurrence of different wake states based on the value of axial induction factors [6]

speeds up the flow and thus operates in a 'propeller state'. In the range of $0 \leq a \leq 0.5$ which is the most commonly occurring operating state, the rotor will operate in a 'windmill state'. In this state, the flow is slowed down as it crosses the rotor but still does not recirculate and the assumption of momentum theory does not break down. At higher values of inductions, i.e. $0.5 \leq a \leq 1$, the rotor is heavily loaded. This state is called the 'Turbulent wake state'. In this range, one can observe a great reduction in wind speeds and also areas of recirculation in the wake region. In this state, a significant amount of rotor wake interactions can be observed. It should be noted that due to recirculation in the wake, the assumptions of momentum theory will break down. This is the reason that empirical corrections such as Glauert's correction [48] are being applied in such cases of heavily loaded rotors. An induction value of $a = 1$ signifies the 'Vortex Ring State (VRS)'. This is the state where the flow is trapped at the rotor and there is complete blockage of flow. At $a > 1$, one can observe flow reversal near the rotor itself and this will lead to the occurrence of 'propeller brake state'. Along with using axial inductions to predict the operating state of a wind turbine, there are several other methods to identify these states too.

Further research was conducted on analysing operating states such as TWS and VRS to understand the mechanism by which they arise. Sorensen et al. [7] studied the mechanism by prescribing uniform load on an actuator disk. TWS occurred at high C_T values such as $C_t = 1.2$. These high values of C_T are not frequently occurring in onshore wind turbines. However, C_t values can reach this range more frequently due to the added velocity components due to platform-induced motions. Visualization of streamlines near the tip of the rotor at $C_t = 1.2$ shows that TWS is essentially a transient phenomenon. It is noticed that TWS stabilises to reach VRS or Propeller brake state depending on how high the values of C_T are. Figure 2.2 gives a visual representation of this transient phenomenon. It was also observed that VRS can occur more frequently as the amplitude of platform motion increases [28].

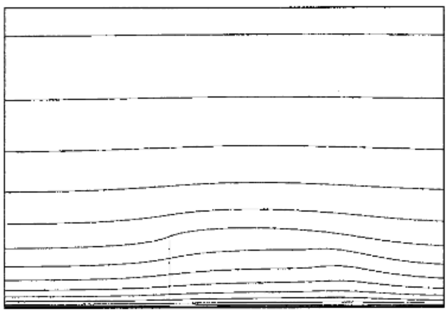

(a) t_1

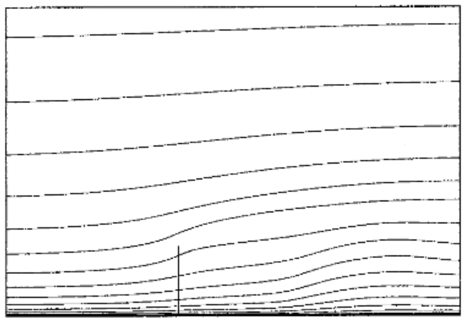

(b) t_2

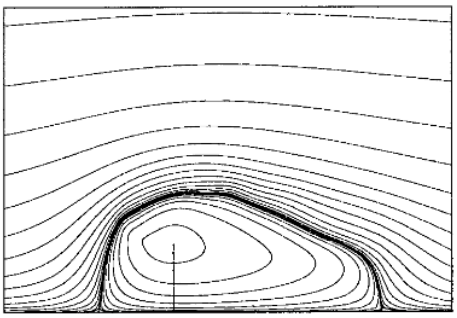

(c) t_3

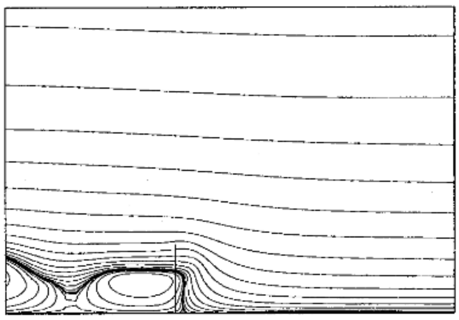

(d) t_4

Figure 2.2: Evolution of TWS at different time steps [7]

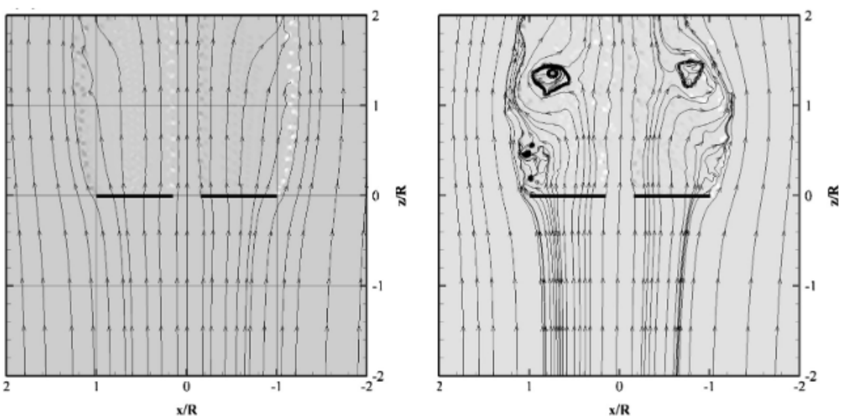

Figure 2.3: Comparison of Vorticity field and streamlines between a fixed (left) and a pitching (right) FOWT.[8]

2.2. Types of methodologies

Based on the methodology used to solve for the aerodynamics of a rotor, the solvers can be broadly categorised into three divisions. They can be categorised into momentum-based (BEMT), vorticity-based, and finite volume (CFD) models. In this part, a brief introduction to these methodologies along with examples of instances where these models are used is provided.

2.2.1. Blade Element Momentum method

BEMT-based models are one of the simplest and cheapest models used to analyse the aerodynamics of a rotor. They take a simplistic approach by making simplifying assumptions on the flow physics and the geometry of the rotor. Thus, they need to be calibrated or developed using the data obtained from higher fidelity simulations such as experiments or CFD simulations. Therefore, before any of these models can be used, it is necessary to understand the simplifying assumptions made. The essential simplifying assumptions made by these models along with their impact on their capabilities are given below:

- **Inviscid flow**: A FOWT's wake will be fairly turbulent and also will have significant shear. Thus, assuming the flow to be inviscid can be quite detrimental to the quality of the results. Important viscous effects, such as the dissipation of turbulence and wake meandering, won't be taken into consideration when modeling the wake when the flow is believed to be inviscid.
- **Uniform inflow**: In this assumption, the flow is assumed to have a constant wind velocity. Thus, changes in the magnitude and direction of the wind flow are not inherently considered in the calculations. In essence, all the blade elements are assumed to experience an inflow that has a constant wind speed that does not vary with time. However, in the case of a FOWT experiencing platform pitching motion, the wind speed constantly varies with time and space.
- **Axial inflow**: This is a particularly harmful assumption for FOWTs because a FOWT will be operating in tilted inflow conditions for a significant time during its operation. Therefore, BEM models as they are, are not suitable for FOWT analyses. The results need to be corrected using empirical models derived from high fidelity results. Researchers have thus developed and are continuously improving them to correct for the non-axial inflow. These models are called the 'Yaw correction models or skewed wake correction models' such as [49][50][51][52][53], to correct for the radial flows on rotor.

Blade Element Momentum Theory assumes the rotor to be a semi-permeable actuator disk with the assumptions mentioned earlier. The values of this 'permeability' is determined by calculating the axial and radial induction factors. The expression for calculating the induction factor is calculated is given by:

$$a = 1 - \frac{U_r}{U_\infty} \tag{2.3}$$

A BEM-based solver discretizes the actuator disk into individual elements thus simplifying the actuator disk geometry into multiple annuli. Figure 2.4 provides an illustration of the components of velocity of inflow. The figure also illustrates the tangential and normal components of aerodynamic forces on the blade. The solver starts solving for the forces on the rotor by initializing the values of a and a'.

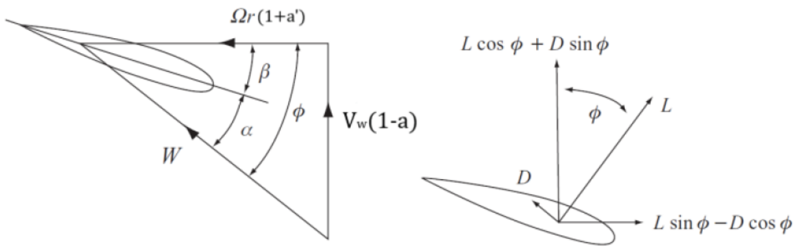

Figure 2.4: Vectors denoting the components of velocity and forces on a blade element [9]

Upon initializing them, the induced velocities at each element are calculated and are resolved into components normal and parallel to the airfoil's chord. With the information on the velocity components, the inflow angle of attack α is calculated. With the knowledge of the angle of attack and velocities, the aerodynamic forces on the blade element are calculated with the help of airfoil polar data. The lift and drag forces are calculated from the respective coefficients using the relations given below:

$$dL = \frac{1}{2}\rho {V_r}^2 C_l dr \tag{2.4}$$

$$dD = \frac{1}{2}\rho {V_r}^2 C_d dr \tag{2.5}$$

The summation of the axial component of these forces gives us the overall thrust produced by the rotor, which is non-dimensionalized to obtain the thrust coefficient C_t. The aerodynamic forces, i.e. the lift and drag forces at the airfoil element are calculated using:

$$dF_{ax} = dT = dLcos\phi + dDsin\phi \tag{2.6}$$

The values of the thrust coefficient calculated using airfoil polar data are then compared with the thrust coefficient calculated using the induction factors. Thus a relation between axial inductions and thrust forces can also be formed and is given in Equation 2.8. After this step, the thrust calculated using airfoil polar data is compared with the thrust calculated using induction factors. If the value of error is more than the desired level of accuracy, the induction factors are corrected accordingly to carry out another iteration of the force calculations. This process continues until the values predicted by airfoil data and axial induction factors are equal. A numerical convergence is achieved only when the values of C_t calculated using the relations Equation 2.7 and Equation 2.8 are equal.

$$C_T = \frac{T}{\frac{1}{2}\rho A_d {U_\infty}^2} \tag{2.7}$$

$$C_T = 4a_{avg}(1 - a_{avg}) \tag{2.8}$$

Due to the simplifying assumptions made by BEM theory, the model can produce accurate results only for a small subset of flow conditions. To make the results more accurate and to make the model more widely applicable, a set of empirical corrections need to applied on the results predicted. They are: Glauert's correction for heavily loaded rotors [54] which is applied for rotors experiencing high values of thrusts ($C_t > 0.5$). To predict the radial distribution of forces properly, tip and hub loss corrections [55] are essential. They account for finite blade effects due to tip and root vortices from the end of the blades.

Engineering correction models

These correction models have been incrementally updated in the past depending on the application. However, they have not been explicitly checked for applicability on FOWT applications. Therefore, this study will attempt to check the applicability of some of the original models and a few updated ones to be applied to pitching FOWT rotors. It should be noted that not all the models mentioned here will be tested. A precise list of the models tested is provided in Chapter 3.

- **Correction for heavily loaded rotors**: BEMT's assumption of continuous streamtube breaks down when the rotor is heavily loaded. For the cases with induction field reaching values of $a \geq 0.5$, a flow reversal can be observed in the wake. This state of operation is called Turbulent Wake State (TWS). The flow outside of the wake (stream tube) is entrained into the wake when the rotor is imposing high thrusts. To correct the induction field values, Glauert proposed an empirical correction for the relation between thrust values and the inductions. The version proposed by Glauert initially, assumed a uniform axial induction. But this assumption will tend to break down in most real-life scenarios.

  Buhl et al.[56] proposed a newer correction model that includes the tip-loss correction factors, given by Equation 2.9.

  $$C_T = \frac{8}{9} + \left(4F - \frac{40}{9}\right)a + \left(\frac{50}{9} - 4F\right)a^2 \tag{2.9}$$

  where F is Prandtl's tip-loss correction factor and C_T is the thrust coefficient.
- **Tip and hub loss corrections**: BEM solvers assume the rotor to be a continuous disk that does not have finite tip vortices. However, to obtain a realistic prediction of the induction field, the calculated induction needs to be corrected for finite tip effects, especially near the blade tip and hub region. This correction can be directly applied to the momentum theory predicted results of axial and radial induction factors (a and a'). Prandtl's tip loss correction factor is given by the Equation 2.10.

  $$F = \frac{2}{\pi}\cos^{-1} e^{-f} \tag{2.10}$$

  where

  $$f = \frac{B}{2}\left(\frac{R - r}{r \sin\varphi}\right) \tag{2.11}$$

  Similar to blade tip vortices, there are vortices shed from the hub region also. To correct for their effects on the induction field, Equation 2.11 is used. It should be noted that φ denotes the inflow angle and R_{hub} gives the hub radius.

$$f = \frac{B}{2}\left(\frac{r - R_{hub}}{R_{hub}\sin\varphi}\right) \tag{2.12}$$

- **Skewed wake corrections**: As mentioned earlier, momentum models are developed assuming an axial inflow. Therefore, whenever the rotor experiences a non-axial inflow, it is necessary to apply empirical corrections to the results.

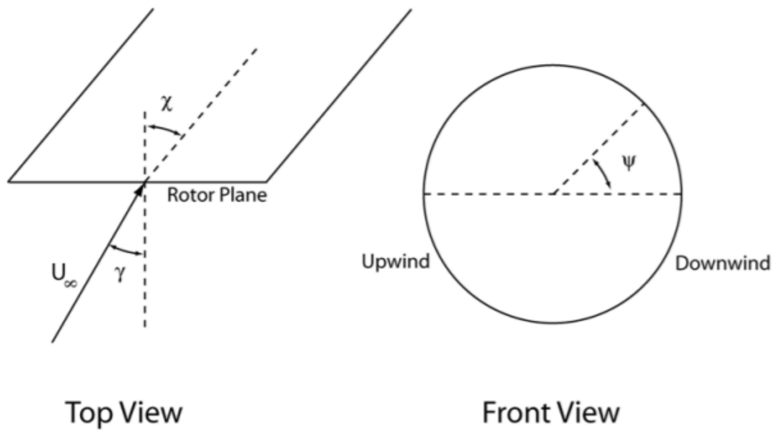

Figure 2.5: Illustration of the yaw (γ), wake skew(χ) and azimuthal angles(Ψ)[10]

The first model for skewed inflow was developed by Glauert[50], and is given by Equation 2.13. This model was developed assuming the rotors as auto-gyros. This means that the model is developed under the assumption that the rotors are lightly loaded. Therefore, this model cannot be expected to give accurate results under all circumstances.

$$a_{\text{skew}} = a\left[1 + K\frac{r}{R}\cos\psi\right] \tag{2.13}$$

where K is a constant depending on wake skew angle χ. Pitts and Peters [49], improved on the Glauert's model. The model equation given by Equation 2.14. However, this model also assumes a uniform inflow. This can again lead to less accurate results in the case of a pitching wind turbine. Therefore it is essential to check its validity in the case of a pitching FOWT.

$$a_{\text{skew}} = a\left[1 + \frac{15\pi}{32}\frac{r}{R}\tan\frac{\chi}{2}\cos\psi\right] \tag{2.14}$$

There are a few models developed more recently that consider effects of unsteady inflows also. Schepers and Snel [57] is such a model. It simplifies the unsteady effects by distinguishing them based on their scales. They are the unsteady profile effects that occur at the scale of the airfoil and dynamic inflow effects that occur at the rotor scale. Corrections for these airfoil scale effects will be common to all the unsteady flows irrespective of the rotor motion as they are dominated by airfoil scale aerodynamic and viscous effects. However, the dynamic inflow correction models need to be updated for every type of unsteadiness.

An example of such dynamic inflow effects is when the inflow velocity of a wind turbine rotor undergoes a sudden change in inflow velocity (for example during a wind gust). This can also arise due to airfoil scale changes such as a change in blade pitch angle or even in dynamic yawing [57]. It takes some time for the wake to adjust to this sudden change in inflow which is called 'wake inertia'[57]. The effects of dynamic inflow can be observed on all the inputs and responses of the rotor, which include the inflow's angle of attack, the induction field, and thus the thrust and torque outputs. **??** gives the dynamic response of an airfoil element that underwent a sudden change in inflow's angle of attack. An undershoot can be observed in the plot when the pitch angle is reduced to a lower value. Similarly, the change in blade pitch back to the original value gives rise to an overshoot. It can also be observed

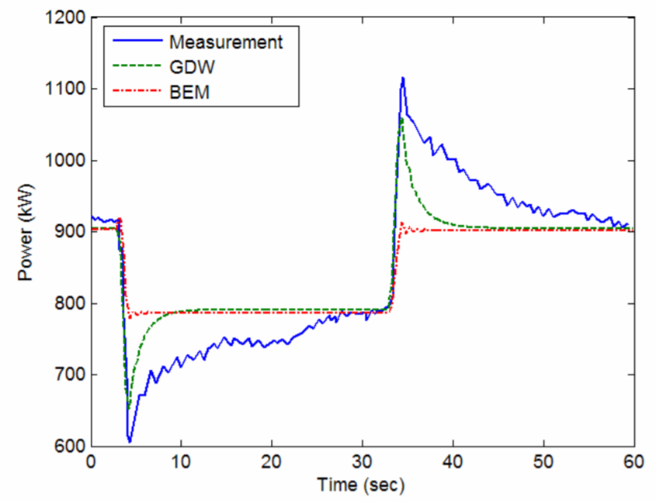

Figure 2.6: Plot of the dynamic response due to a step change in blade pitch[11]

that the BEM results do not inherently capture the effects of dynamic inflow signified by a flat profile for induction values.

There have been several dynamic inflow models developed in the past and a few examples of those are Oye's model [58][59], ECN's model [60], Pitt and Peter's model[49], and Suzuki[11].

2.2.2. Vorticity bases methodology

Unlike the momentum theory and NS equation-based solvers, vorticity-based models just calculate the flow physics only based on the values of circulation captured. Based on how the vorticities are modeled there are three different types of vortex models developed so far. They are the lifting line model, lifting surface model, and source-panel model. The difference between these three models arises in the step after discretising the blade into blade elements. As illustrated in Figure 2.7, the three different models mentioned above assign circulations to the blade elements in the following manner:

- Lifting line model: This model assumes the whole lifting element, in this case, the rotor blade to be a 1D line vortex. It then segments this line into elements and assigns different values of circulations to them. The solver then tries to solve for the values of these circulations the same way BEMT based models solve for induction values.
- Lifting surface model: This model adds complexity to the lifting line model and assumes the blade to be a lifting surface (a 2D surface). Each blade element is assigned a set of vorticities along the airfoil's camber line and the final goal of the solver will be to determine the vorticities corresponding to this lifting surface.
- Source-panel method: This method is similar to the lifting surface but comparatively has a greater resolution. Instead of assuming the blade as a two-dimensional surface, lumped vortices are assigned to the airfoil's camber line and solve for the circulation values by applying the Kutta Joukowski theorem.

Apart from this, vortex-based models differ in the way they model the vortices. The vortices can be modeled as a lumped vortex and can be assumed to be a vortex filament. The method of induction field calculation is also a criterion by which vortex-based methods differ. Since vorticity-based models are not the primary points of discussion of this thesis, they are left for the reader to explore and understand.

An essential advantage of these vorticity-based models is that they inherently account for wake inductions and do not rely on empirical models such as dynamic inflow models like BEM-based solvers do to model the wake effects. Wakes are essentially the vortices that are shed from the blade elements when there is a change in circulation, that is, aerodynamic forces on blades. Since vorticity-based models determine the circulation strengths of the bound vortices in edges, it is relatively much simpler to obtain the strength of vortices shed from edges. Therefore, depending on the computational resource

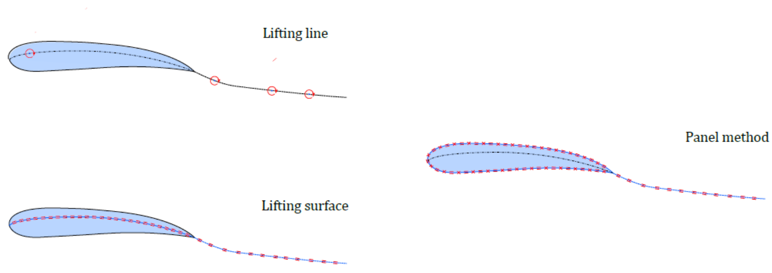

Figure 2.7: Different levels of blade resolutions in vorticity-based models [2]

available, it is just a matter of choice to include the effects of wake on rotor aerodynamics. Therefore, these models need no correction for finite blade effects or heavily loaded rotors as these effects are inherently considered in the model.

2.2.3. CFD based methodology

CFD models predict the flow behaviour by numerically solving for the flow variables such as velocity, pressure, etc. in the Navier-Stokes equations. These equations describe the conservation of mass and momentum in a fluid. These solvers use flow boundary conditions to predict the flow variables. Even though BEM-based models also make use of momentum equations to calculate aerodynamic forces, CFD-based solvers do not make or make very minuscule simplifying assumptions on the flow characteristics. The incompressible form of the Navier-Stokes momentum equation solved by CFD solvers takes the form given in Equation 2.15. Unlike BEM and Vorticity-based models, CFD solvers consider all the viscous effects.

$$\frac{\partial \mathbf{u}}{\partial t} + (\mathbf{u} \cdot \nabla)\mathbf{u} - \nu \nabla^2 \mathbf{u} = -\frac{1}{\rho}\nabla p + \frac{\mathbf{F}}{\rho} \tag{2.15}$$

As long as the wind turbines are under nominal operating conditions, the flow can be assumed to be incompressible as the flow's mach number does not significantly exceed $M = 0.3$. However, with an increase in the size of wind turbines blades recently, a few researchers suggested the usage of compressible NS equations for wind turbine research [61] [19] [16]. These researchers have concluded that compressibility effects are not negligible in the case of FOWT, especially when they are subjected to platform motions of high amplitudes[16].

Like most of the other numerical models, CFD models also discretize the fluid domain into smaller elements using the process called 'meshing'. The CFD solver takes the domain boundary conditions into account and calculates the flow variables by iteratively solving for them in every cell of the domain. In this class of solvers also, there are several categories based on different aspects such as the way rotors are modeled, discretization schemes, and the way turbulence scales are resolved. Starting with the categorization of CFD solvers based on rotor representation, there are three main categories. They are actuator disk (AD), actuator line (AL), and blade-resolved CFD models. Out of these, AD and AL models are particularly interesting for modeling wind turbine wakes as the boundary layer need not be resolved and simulations can be performed on much coarser meshes [62]. A brief description of these models is given below:

- **Actuator disk simulations**: These are the simplest models to study rotor aerodynamics as far as rotor modeling is concerned. While the models discussed so far (BEM and FVM) solve for aerodynamic forces by the rotor, in actuator disk models, aerodynamic forces produced by a rotor will be calculated beforehand and are prescribed to the disk. These prescribed forces are added as momentum sources and are substituted in the place of '**F**' of the governing equation Equation 2.15 in the respective cells of the computational domain. A clearer representation of actuator disk modeling is provided in Figure 2.8.

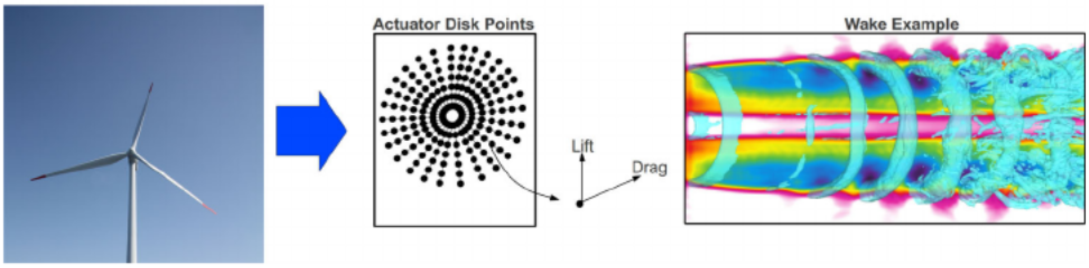

Figure 2.8: Depiction of a rotor modeled as an actuator disk and an example of the resulting wake field. [12]

AD models have been widely used across the industry[7][12] for rotor aerodynamic analyses mainly because they are cheaper and faster than blade-resolved models both from the pre-processing and solving point of view. However, it is also essential to have an understanding of the force field created by the rotor under the imposed flow conditions. As far as an axisymmetric flow is concerned, actuator disk simulations show good agreement with experimental results and can be useful in providing insightful information on dynamic inflow [63] and also on the wake states of rotor [64].

However, due to the simplifying assumptions the model takes while modeling the rotor, actuator disk models do not account for finite tip effects and need empirical correction to account for these effects as they are not inherently considered in these simulations. Another important drawback of actuator disk simulations is that the prescribed forces have to be axisymmetric. However in certain cases where the rotor is not experiencing an axial inflow, such as a yawed wind turbine or a FOWT in pitching motion, the force field across the rotor plane will not be axisymmetric. In such cases also, it is not advisable to use AD models directly [65] to simulate the flow field around the rotor as prescription of a non-axisymmetric load is impossible in an AD model. In fact, there have been a number of blade-resolved CFD analyses on FOWTs in the past, but usage of AD models for analyzing FOWT under non-axial flow-inducing platform motions has not been performed so far.

- **Actuator line models**: Sorensen and Shen [66] pioneered the usage of actuator line models for rotor analyses. This model assumes the blades in the rotor to be lines that impose thrust on the incoming flow. Similar to AD models, it is necessary have a precursive knowledge of rotor force fields to create an AL model with prescribed forces. But a conventional AL model (as introduced by Sorensen and Shen) can be used to calculate the force field on the rotor plane because they use airfoil polar data to calculate the forces. Figure 2.9 attached below provides a visual illustration of an actuator line model of a rotor.

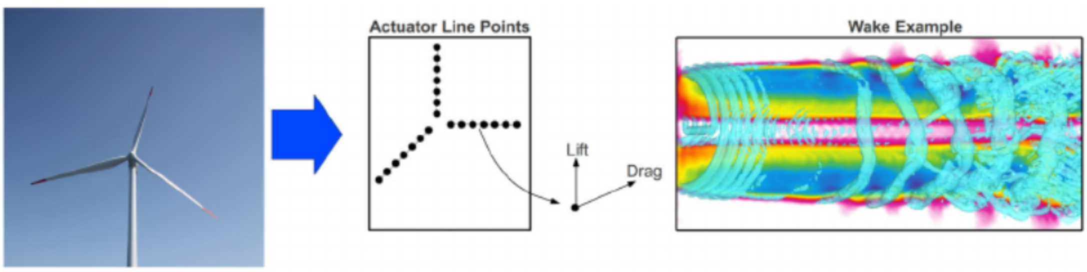

Figure 2.9: Illustration of an actuator line model [12]

AL models can be freely used to analyze the flow field around a rotor in skew. An example of such research is the one done by Mikkelsen [67] where he used AL models to study the effect of uniform skewed inflows on a HAWT rotor. Mikkelsen et al. also conducted research using AL models to study the aerodynamics of isolated rotor [68] and a row of rotors in each others wake [69]. AL models were also widely used to understand the stability and effects of finite tip and root vortices in the wake by researchers such as Ivanelle et al.[70].

- **Blade resolved CFD models**: Unlike AD and AL models which simplify the rotor geometry, in blade resolved models, the actual geometry of the blade and the hub will be considered in the domain. To model the rotation of blades, these models make use of overset grid method[71]. Blade resolved models are particularly advantageous to study the airfoil scale effects because they inherently account for viscous effects on the blade surface such as viscous interactions inside the boundary layer, flow separation, etc. [72].

  Owing to the complexity of blade-resolved models, they take significantly longer for pre-processing. They also have a high demand for computational resources due to their geometric complexity. Irrespective of the computational demand, they have been the most used CFD methods to analyze the aerodynamics of a pitching FOWT. Since analyses on FOWTs under platform pitching motion are still a relatively new field of research, researchers have been choosing blade-resolved models for their aerodynamic analyses to obtain a broad understanding of the induced effects.

Along with the choice of complexity in rotor modelling, the choices made in turbulence modelling also greatly affect the results chosen. Based on the extent to which turbulence is modeled, there are primarily three kinds of simulations. Each of these methods is briefly introduced below:

- **Direct Numerical Simulations**: In DNS simulations, the Navier-Stokes equations are numerically solved without making simplifying assumptions to resolve turbulence. Due to the expansive length scale range of turbulent eddies, the computational grid should comprise cell sizes as small as the smallest eddies are. This makes DNS significantly costlier than the other methods available to resolve turbulence. Since DNS can capture the flow details in all length scales, they are particularly suitable for fundamental studies at moderate Reynolds numbers.
- **Large Eddy Simulations**: LES simulations take a hybrid approach to resolve turbulence. The turbulence scales are low-pass filtered to separate out small-scale eddies from large scales. Small-scale turbulent eddies are modelled, usually using wall models, and large-scale eddies are resolved numerically as DNS does.
- **Reynolds Averaged Navier-Stokes simulations**: RANS simulations, as the name suggests, provide averaged results of flow variables so that the fluctuations are not even considered in the simulations[73]. They use different models, which differ in the nature their assumptions on turbulent scales, to calculate the Reynolds Shear Stress component. Since the small scale eddies are modeled, RANS does not need grids as fine as LES or DNS demands, which makes them a cheaper and more feasible option. Usage of RANS can be particularly challenging because there is no turbulence model that can be used universally for all applications. Since the results produced by RANS vary significantly based on the turbulence model used, a careful choice of turbulence model depending on the application [74].

With the evolution of technology, several new methods of CFD simulations were introduced. Owing to the high computational costs of DNS and LES, RANS is considered the ideal choice for CFD simulations as they provide detailed flow information with adequate accuracy even with a low-resolution mesh [75]. However, results from RANS simulations lack reliability as small scale turbulence near wall (in this case, the rotor) is not adequately accounted for or averaged out when the fluid is significantly unsteady [73]. Therefore, new hybrid methods such as Detached Eddy Simulations (DES) [76], Delayed Detached Eddy Simulations (DDES) [77] and Improved DDES [78] have been invented which serve as a compromise between RANS and LES in terms of computational costs and accuracy [79]. The preferred choice of simulations for this thesis is discussed in **??**.

2.3. Methodologies used in literature

In this chapter, an overview of past research on FOWT under the influence of effects from platform motions is provided. First, a discussion on the methodology used in the past is done, i.e. is the analysis experimental or uses numerical simulations? In the subsequent sections, the popularity of different types of simulations and simulation choices such as the choice of fidelity, turbulence model used, etc. is provided. For reference, Table 2.1 gives an overview of the methodologies used by past researchers. This chapter concludes by discussing the major inferences done by past research on pitching FOWT aerodynamics.

2.3.1. Methodology used for the analyses

As far as aerodynamic research on pitching FOWTs is concerned, the number of aerodynamic research using experimental simulations is comparatively lower than the number of numerical research done. However, there have been several instances in the past where experimental simulations were used to study the effects of pitch motion such as the research performed by Khosravi et al.[80], Rockel et al.[81] and Bayati et al.[82].

Khosravi et. al[80] conducted an aero-mechanic performance and wake study on a FOWT under prescribed pitching motion. Using Particle Image Velocimetry (PIV) to analyze the wake enables us to visualize and analyze the ensemble average of Reynolds stresses, and turbulent kinetic energy distributions in the wake and helps in visualizing the development of unsteady vortices arising due to pitching motion[80]. A study done by Rockel et al. [81] mainly dealt with the wake analysis and comparison of wakes from a fixed bottom turbine and a FOWT under pitch motion. A similar research conducted by Bayati et al.[82] compared results from FAST v7 [27] BEM solver with the wind tunnel measurements of a FOWT under prescribed pitch and surge. This study also observed discrepancies between BEM and experimental results; and concludes by stressing the need for further analysis with a focus on the unsteady phenomena.

Numerical researches are prominent in aerodynamic research on the effects of platform motions and the following sections in this chapter will provide the reader with a perspective on the popularity of numerical research in the field of FOWT aerodynamics (or wind turbine aerodynamics, in general). Table 1.1 gives us an idea of the sheer number of researchers in this field that used numerical simulations for their analyses. Experimental analyses can be highly beneficial for an aero-hydrodynamic analysis as it is easier to study the exact effects of hydrodynamic loads on the rotor instead of using external actuation to simulate the platform motions. But, to study the platform motions individually, we need an external actuation device which increases the complexity of the setup. Owing to their feasibility and capability to produce reliable results despite being simple to model, numerical simulations are the chosen type of simulations for this master's thesis.

2.3.2. Aerodynamic calculation methodologies

Depending on the research objective, all three levels of fidelity have been equally utilized by researchers in the past. This section discusses the past researchers' background motivation for the chosen level of fidelity and also the results obtained. A more in-depth study of the aerodynamic effects of pitch motion will be done later in Section 2.4.

BEM based simulations

BEM has been used in several instances in the past to analyze FOWT aerodynamics. The first-ever analysis on the effects of platform motions, done by Sebastian et al.[26], was done on FAST[86]. This study was performed on an NREL 5MW baseline wind turbine, placed on different floating structures, under different operating conditions defined by wind and wave data from BMT ARGOSS[86]. This research aims to get a primitive understanding of the unsteady effects that platform motions can induce on the rotor. The research predicted dominant platform motions for each floating structure and also a breakdown of momentum balance equations due to a highly unsteady flow field.

Most of the BEM-based simulations done so far have used FAST as their solver of choice mainly because of its capability of aero-servo-hydrodynamic coupling. Examples of such publications include [24], [87] and [88]. Karimirad[88], along with FAST, considered another popular aerohydrodynamic code called HAWC2[89] in his research. There have been several instances where results from FAST were used as a reference for the validation of a newly developed solver. Since the momentum-based methods were observed to fail due to a high degree of unsteadiness, they need to be first validated with the results from a higher-fidelity experiment. There have been instances such as [5] when in-house BEM codes are evaluated against FAST and RANS-based CFD results. Sivalingam et al. [18], on the

Table 2.1: List of select publications on pitching FOWTs in the past.

Publisher, year	Methodology	Turbulence model	Objective of the publication
Shi W. et al.[17], 2021	CFD	NA	To study the loading and wake characteristics of a pitching FOWT
Lu w. et al.[83], 2021	CFD		To assess the ability of CFD to predict the low-frequency hydrodynamic excitations.
Ortolani et al.[16], 2020	CFD	k-ω SST	To study of the performance of a FOWT pitching with high amplitudes and frequencies.
Ortolani et al.[19], 2020	BEMT, CFD	k-ω SST	To compare FAST and CFD results
Rodriguez and Jawors [35], 2020	FVM		To develop an aeroelastic framework
Kim and Shin[38], 2020	Experiment, BEMT		To test a wind turbine prototype
Ahn and Shin[39], 2020	Experiment, BEMT		To compare FAST and Experiment results
Fang et al.[40], 2020	CFD	NA	To study of the performance of a FOWT pitching with different amplitudes and frequencies.
Lienard at al.[29], 2020	CFD	NA	To study the effect of pitch and surge motions
Shen at al.[13], 2018	FVM		To analyze the unsteady aerodynamics of FOWT
Wen B. et al.[43], 2018	FVM		To study of power performance of a pitching FOWT.
Shen at al.[84], 2018	FVM		To study the loads and unsteadiness in wakes
Wen et al.[15], 2018	FVM		To study the wind shear induced by platoform pitch FOWTs
Leble et al.[14], 2017	CFD	NA	To study the effect of pitch and yaw motions
Wu C. et al.[1], 2017	CFD	k-ω SST	Develop a new CFD based numerical model
Khosravi et. al[80], 2016	Experiment,BEMT		To study the effect of pitching motion using experimental results
Bayati et. al[82], 2016	Experiment,BEMT		To compare FAST and Experiment results
Sivalingam et al.[18], 2015	BEMT, CFD	k-ω SST	To study dynamics of pitching FOWT using aerohydrodynamic simulations
Tran T. et al[85]. 2015	BEMT, CFD	k-ω SST	To study the effect of pitch amplitude and frequency on FOWT aerodynamics
Tran T. et al[5]. 2015	BEMT, CFD	k-ω SST	To study the effect of pitch and yaw motions on FOWTs
Tran T. et al.[4] 2014	CFD	k-ω SST	To study the effect of pitch on FOWTs
Jeon M. et al.[8], 2014	BEMT, FVM		To study unsteady aerodynamics using vortex lattice method

other hand just used the hydrodynamic module [90] of FAST to obtain the floating structure dynamics from prescribed wave inputs and used the floater dynamics to analyze the unsteady aerodynamics of a pitching rotor using CFD.

Vorticity based simulations
Researchers seem to use FVM solvers for the study of unsteady FOWT aerodynamics because of their optimal compromise between cost-effectiveness and physicality. Vorticity-based models are particularly useful in studies involving wakes and finite tip vortices because of their inherent ability to trace the vortex lumps in space and time. Figure 2.10 shows such an instance where a vortex model is used to calculate the effect of tip vortices in a rotor.

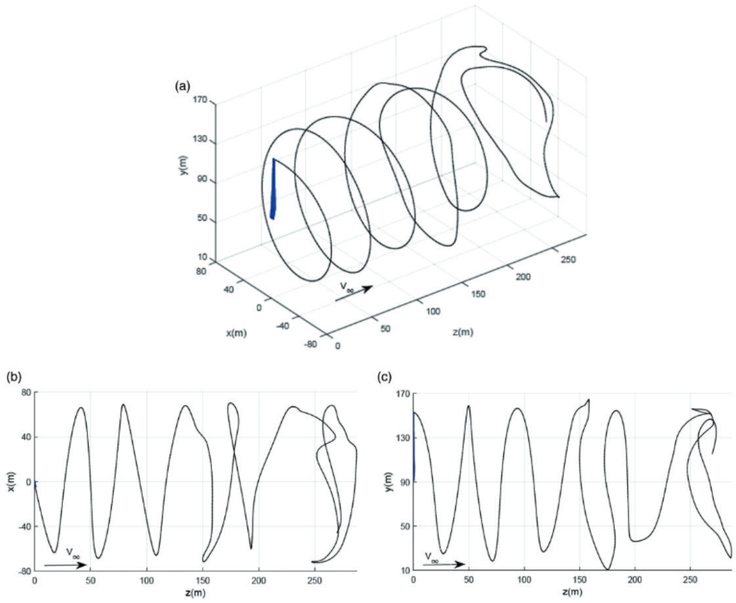

Figure 2.10: Study of tip vortex instability using a free vortex method, Shen et al. [13]

Shen X. et al.[13] used a lifting surface solver with a free wake model to study the blade-vortex interaction and occurrence of various flow states (TWS and VRS) in a FOWT under the influence of unsteady effects from prescribed platform motions. There have also been instances where a new vortex model is developed specifically for floating rotors. Sebastian et al. [91] and Rodriguez et al. [35] developed a new model that is based on vortex modelling to be applied specifically for FOWT application. Studies done on the effect of pitching amplitude on the power output of FOWT in the past[14][85] concluded that the average C_p increases with an increase in pitching frequency.

CFD simulations
CFD simulations are popular among researchers to study complex and fine aerodynamic details such as turbulence production with greater accuracy [18][4]. They are also a popular method used to benchmark the results from BEM or FVM codes. Publication by Tran T. et al. [4] is such an example where they used results from RANS CFD simulations of a pitching FOWT to estimate the accuracy of their in-house unsteady BEM code. This paper also reports that the discrepancies between CFD and UBEM results increased with the increasing pitching amplitude. This increase in errors was attributed to increased wake interaction at high amplitudes. A similar study on benchmarking BEM results was done by Sivalingam et al.[18] and the publication also contains recommendations for BEM corrections based on inferences drawn from CFD data. Tran T. et al. [85], in a later study, conducted a deeper wake-visualization analysis on the tip vortices using CFD to study the blade-wake interactions. Several other studies on rotor-wake interactions, wake strength and geometry have been performed by using CFD simulations [5].

Wu et al. [1] developed a coupled CFD method that couples the rigid body motion of the rotor with platform motions in multiple degrees of freedom (surge-pitch-heave motions in this case). Results from this model were validated with steady cases from past literature and then used to benchmark BEM-based FAST results. The occurrence of complex wake states such as TWS and VRS in an unsteady FOWT rotor was done by Leble et al. [14]. The simulations were conducted for a FOWT rotor under dynamic pitching and yawing with varying amplitudes. The ability of CFD models to account for compressibility and viscous effects has also been the unique selling point of CFD. Ortolani et al. [16] used compressible RANS simulations to assess the aerodynamics of FOWTs under severe pitching motion.

In this master's thesis, the primary aim is to obtain an in-depth understanding of a pitching FOWT's aerodynamics. To achieve that, it is essential to consider the viscous effects [4] such as viscous dissipation. Since the research field is still not mature, it is essential to first fully understand flow physics before diving into secondary effects. Therefore, this master's thesis will employ CFD simulations using OpenFOAM[92] for the aerodynamic analyses.

2.4. Inferences from literature study

This section discusses significant research findings, particularly concerning a pitching FOWT's aerodynamic effects from past studies mentioned in Table 2.1. This is done to provide an overview on what are inferences that is already present in the research community and what needs extra attention.

- Jeon et al.[8]: The study mainly aims to check the ability of VLM-based models to capture complex flow phenomena. It was found that VRS can occur when pitching FOWTs are operated at low inflow speeds. Due to a high windward velocity when the rotor is pitching forward, a recirculating flow was observed at the top of the rotor ($\Psi = 0^o$) as shown in Figure 2.3. An increase in inflow velocity during windward pitching tends to increase to TSR of blades and thus leads to the clustering of tip vortices near the rotor. Thus, this study predicts complex flow behaviour when the rotor is pitching toward the wind flow.
- Tran T. et al.[4]: This study focuses more on the rotor scale phenomena such as change in average power output. It was shown that pitching motion can lead to a substantial variation in power output and loading on the rotor. Loading on individual blades are highly varying due to pitching motion. Blade at ($\Psi = 0^o$), represented by black lines in Figure 2.12, was observed to have the highest load variations which are again attributed to higher platform-induced velocities at this blade due to higher distance from the platform.
- Tran T. et al[85]: This study concentrates more on the wake behaviour. The gap between consecutive helixes of tip vortices is not constant for a pitching FOWT. The gap increases when the FOWT pitches forward and decreases for a downstream pitch which signifies the presence of strong rotor-wake interactions. The study also concluded that the tip vortices shed during forward pitching motion are stronger than the ones shed during backward (along the inflow) pitch.
- Tran T. et al[5]: This study is an extension of the last inference. The change in strengths of tip vortices also tends to get influenced by the amplitude of pitching. Stronger tip vortices arise at higher amplitudes of pitching and the vortices are weaker for lower amplitudes of pitching.
- Leble et al.[14]: Variation of thrust and power increased with an increase in pitching amplitude. However, it was observed that the mean power output was observed to increase while the mean thrust decreased with an increase in pitching amplitude. Vortex Ring State was observed in a particular case (high pitching amplitude and low pitching) where pitching amplitude was $A_p = 5^o$ and a frequency of $f_p = 0.1Hz$.
- Wen et al.[15]: The effect of TSR on the power output of a pitching wind turbine is studied in this publication. Firstly, a comparison between the performance of a fixed foundation and FOWT is studied. It was observed that the mean power increases for a HAWT under the pitching condition. In previous research publications such as [14], it has been shown that the power output increased with an increase in pitching amplitude. However, in this research it has been shown that, with an increase in amplitude (denoted as reduced frequency in Figure 2.13 the mean power decreases at lower TSRs and increases at higher TSRs. This marks that there is no clear inference on the interaction between the rotor's TSR and the pitching dynamics.

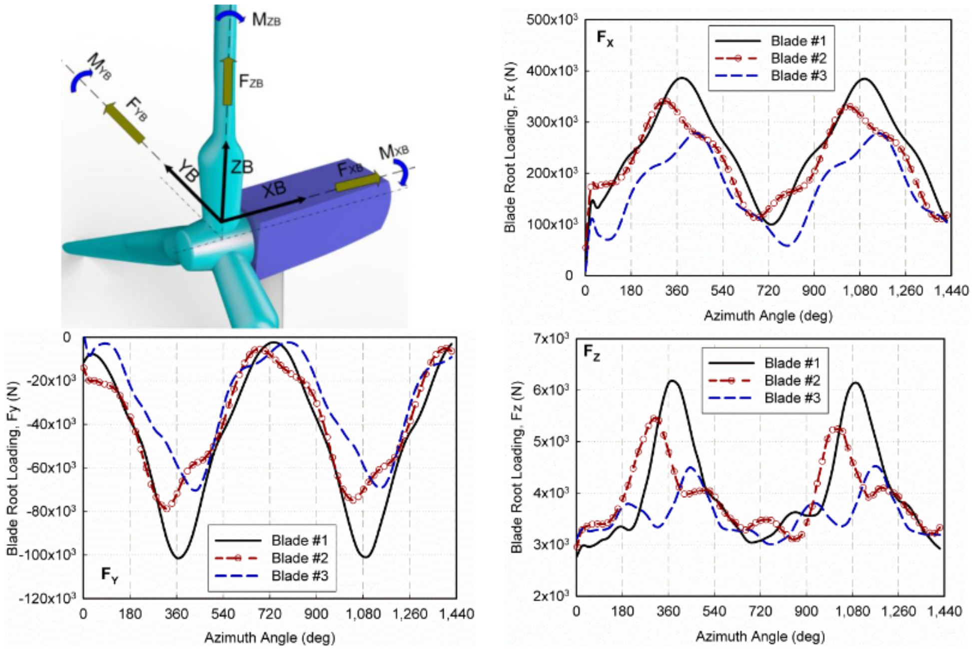

Figure 2.11: Individual blade loading (F_x, F_y, F_z) in a pitching FOWT, Tran et al. [4]

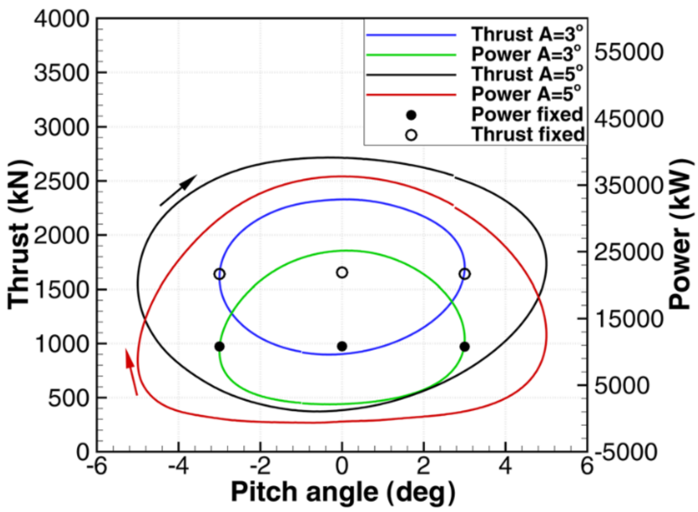

Figure 2.12: Thrust and power hysteresis loops for different pitching amplitudes[14]

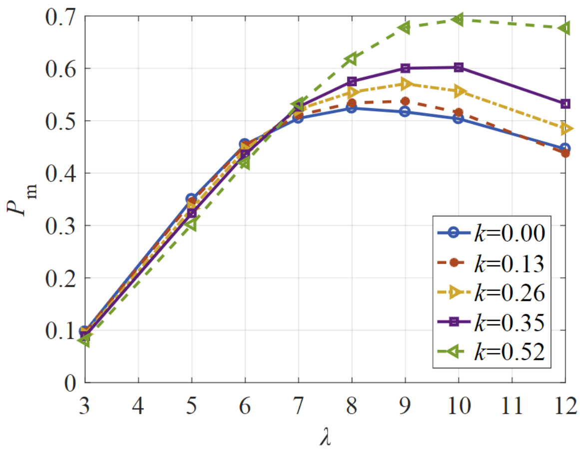

Figure 2.13: Power variation with TSR (λ) at different reduced frequencies[15]

- Lienard et al. [29]: Background reasoning behind the increase in mean power output of a pitching FOWT is analyzed in this research. It has been shown that the extra power is obtained from the forward pitching motion and reaches a maximum when the rotor reaches its mean position. Another important inference is that the dynamics in blade loading are dominated more by a change in the blade section's AoA (α) than the change in inflow velocity.
- Fang et al.[40]: The platform pitching motion induces dynamic stall on the airfoil and the airfoil will periodically experience stall leaving it in 'stall flutter'. This phenomenon particularly happens during the windward pitching motion. Even though intuitive, this study also observed that the amplitude of thrust and torque outputs of the rotor decreased with an increase in pitching periods.
- Rodriguez and Jawors[35]: They used their in-house FVM-based code for the analyses. On observing the blade response parameters like the individual blade deflections, rotor power, and thrust outputs, it was seen that at low inflow speeds (below rated wind speed) the wave-induced rotor motions have a lesser impact on blade dynamics. At rated and above-rated wind speeds of operation, the blades have a higher impact from platform-induced motions due to higher rotor-wake interactions. This is contrary to previous studies showing higher rotor wake interactions (which can be denoted by VRS/TWS wake states) occurs at low inflow speeds.
- Ortolani et al.[19]: This study exhibits the significance of compressibility effects (at moderate and high pitching amplitudes) in a pitching FOWT by comparing the results from a compressible RANS and an incompressible RANS CFD models. It was observed that the tip vortices shed into the wake are not continuous but rather intermittent (tip vortices have a periodically varying strength and sometimes are not even shed from blade tips), which is caused by periodic variations in blade angle of attack and entrainment velocity induced by tower's pitching motion. Affirming the conclusions of past research[8][4], this effect was most pronounced in the upper edge of the rotor (at $\Psi = 0^o$). An inversion in pressures at the suction and pressure side was observed at the blade tip in the region of $\Psi = 0^o$ during leeward pitching of FOWT due to high platform-induced velocities. This led to a momentary zero-lift state of the wing tip which is the reason behind the intermittency of tip vortices in the topmost region of the rotor.
- Ortolani et al.[16]: This paper studies the effect of severe platform pitching motions which are considered extreme operating conditions for a FOWT[16]. In the past, it has been shown that the mean power output of a pitching FOWT is higher than a fixed bottom wind turbine [15][29]. In a deeper study, conducted in this paper, it was found that the effective increase in the angle of attack during pitch motion leads to a higher difference in pressure coefficients (C_p) near the leading edge which in turn increases the net power output of the rotor. It was also shown that this effect is more pronounced near the blade root region because blade tips will stall during the forward pitching motion. From Figure 2.14, compressibility effects are observed and are more pronounced at the blade root region which is marked by the highest differences between compressible and incompressible RANS results.
- Shi W. et al.[17]: This research deals with the variation of loading along the contour of the airfoil

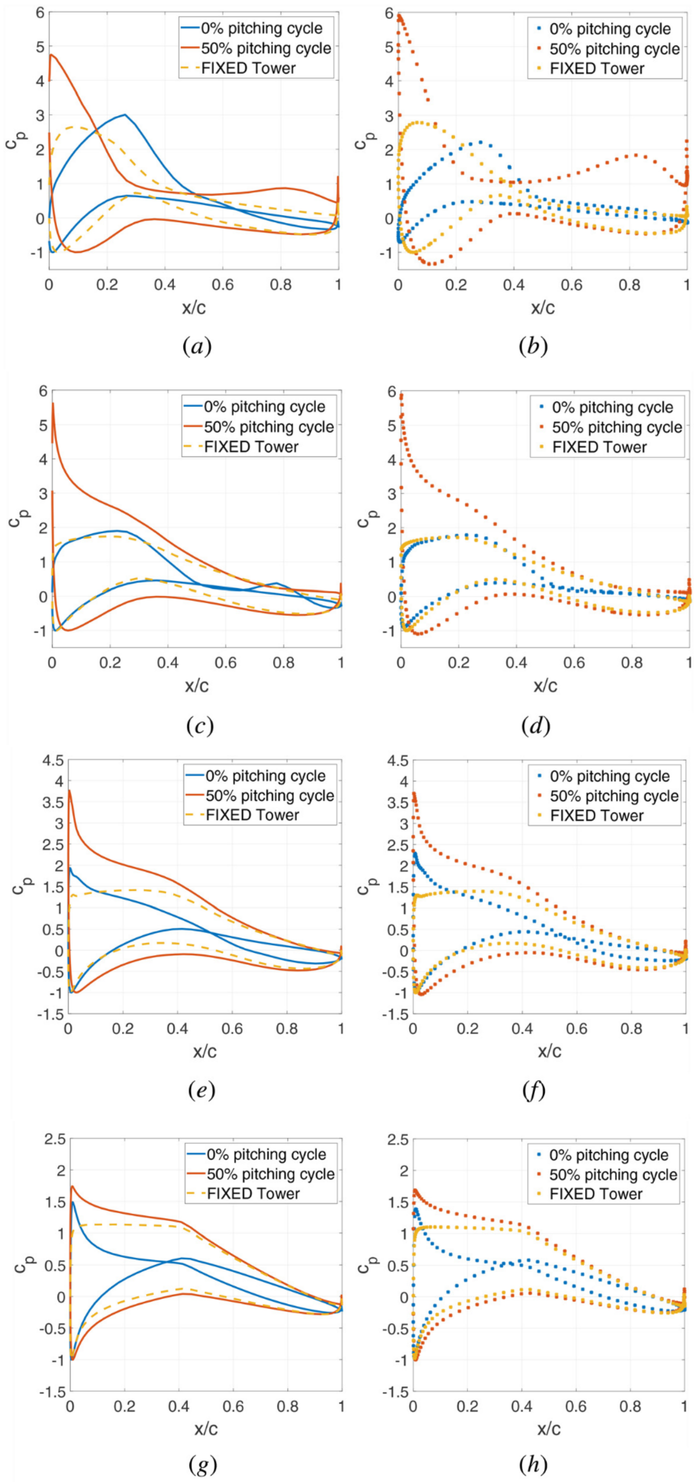

Figure 2.14: Plots of static pressure coefficient C_p at different blade sections - (a,b) - $\frac{r}{R} = 0.24$; (c,d) - $\frac{r}{R} = 0.42$; (e,f) - $\frac{r}{R} = 0.60$; (g,h) - $\frac{r}{R} = 0.96$. Left - compressible RANS; Right - incompressible RANS [16]

when the rotor is pitching. The value of C_p at the leading edge (which signifies the highest blade loading) reaches its maximum in the mean position during windward pitching of the FOWT and a minimum is observed again at the mean position but during leeward pitching motion of the FOWT which is the points of highest and lowest relative inflow velocities. On studying the pitch response concerning a fixed wave excitation and inflow speed at different TSRs, it was observed that the pitching amplitude is higher for a faster rotor than a slower one. This observation clearly shows the influence of TSRs on the response of pitching rotors.

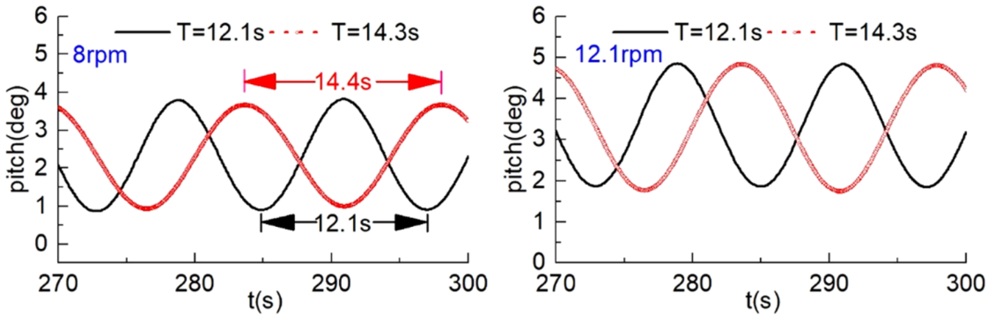

Figure 2.15: Difference in pitch response for two different rotational speeds of the rotor - $\Omega = 8$RPM (left) and $\Omega = 12.1$RPM (right)[17]

2.4.1. Recommendations for BEM

BEMT-based models are widely used by industries for their computational efficiency. Therefore, there is a need to improve the engineering models that are used as corrections for BEM results to account for complex aerodynamic effects that arise in pitching FOWTs. Therefore, this master's thesis will attempt to provide recommendations for the engineering models in BEMT with the help of results from high-fidelity CFD simulations. An attempt to test the validity of newer, improved model correction models for pitching FOWTs will also be considered in this master's thesis.

As discussed in Section 2.2.1, BEM models are not readily suitable for use in analyses of FOWTs because they are inherently incapable of accounting for complex flow phenomena that arise when they undergo platform-induced motions. Additionally, they are not advised for unstable flows in particular since the adjustments for a dynamic stall and a dynamic wake are implemented individually and are not connected[10]. However, a number of correction models have been developed in the past to take into account tip vortex effects, unstable effects brought on by dynamic intake, and to adjust for skewed wakes, which are fundamental components of the aerodynamics of a pitching FOWT. Similar research on providing recommendations for BEM using CFD results have been done in the past[85][5][18][19]. Certain researches such as [82][38][39]. There have also been cases where incremental modifications have been suggested based on comparisons between the BEM and experimental data. The comparisons of the results and the suggestions made by these researchers are covered in the next subsection.

Comparing BEM and high fidelity results

Most of the research done to check the validity of BEM solvers in predicting the aerodynamic effects of a pitching FOWT used FAST[27] as their choice of BEM solver. FAST, which uses $Aerodyn$ module [93] for aerodynamic simulations, pre-includes certain empirical correction models to account for unsteady, skewed inflows.

One of the first researches to check the validity of BEM results for pitching FOWTs was done by Tran T. et al.[85]. This study considered both implementations $Aerodyn$ solver, with BEM (denoted as FAST-BEM) and GDW (denoted as FAST-GDW) for the comparative analyses. The study reported that, for small pitching amplitudes ($A_p \leq 1^o$) where the platform-induced velocity is low, results from FAST-BEM are closer to CFD results, while FAST-GDW results showed an over-prediction in the power outputs. On conducting a deeper study in [5], it was observed that the discrepancies between UBEM and CFD results are most pronounced in the leeward pitching motion. This is due to the incapability of BEM solvers to account for synthetic rotor-wake interactions and also their inability to capture the viscous effects such as dynamic stall. It was further recommended to improve the dynamic stall and wake models in the $Aerodyn$ module. Irrespective of the particular recommendations provided by re-

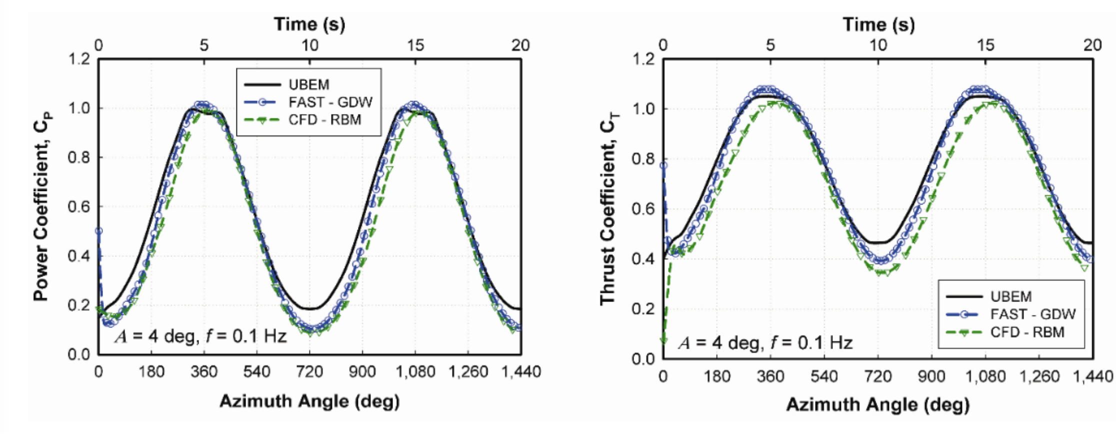

Figure 2.16: Rotor power outputs calculated using in-house BEM (UBEM), FAST-GDW and CFD codes at $A_p = 4^o$ [5]

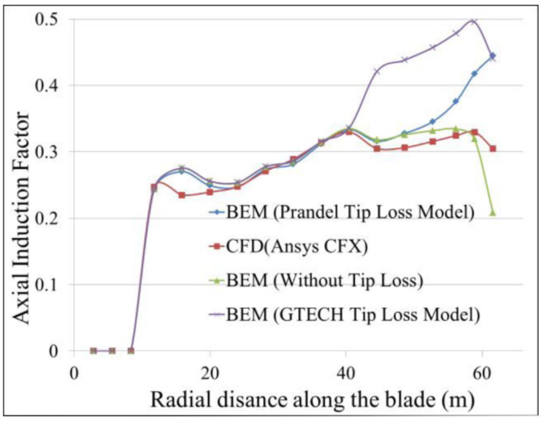

Figure 2.17: Discrepencies between CFD and BEM results near blade tip region, Sivalingam et al. [18]

searchers, a significant blade-vortex interaction was reported in most of the studies. These are marked by the phase difference between thrust and power outputs of UBEM and CFD simulations in Figure 2.16. This phase lag effect in oscillating rotors was also highlighted by Apsley et al.[94]. Therefore this effect needs particular attention throughout the pitching cycle and specifically during the leeward pitching of the FOWT. Induction effects imposed by the dynamic wake on rotors are mainly corrected by dynamic inflow models in BEM-based simulations. Since the unsteadiness in wakes changes with the type of rotor motion, a special dynamic inflow model needs to be developed particularly for pitching rotor applications. To the best of the author's knowledge, there does not exist a dynamic inflow model specific to pitching motion as other platform motions such as surge motion[3] do. Therefore, the models in Section 3.2.2 are tested for applicability to pitching wind turbine cases with an emphasis on the phase difference caused due to the dynamic inflow effect.

Adding to this, yaw correction models also need special attention as a pitching FOWT rotor undergoes a super-imposition of dynamic surge and yaw motions. To the knowledge of the author, these models have not been largely tested for accuracy in the case of rotors in dynamic yaw motion. Therefore a few of the yaw correction models such as Pitt's and Peter's model[49], Glauert's model[50], and ECN's model[53].

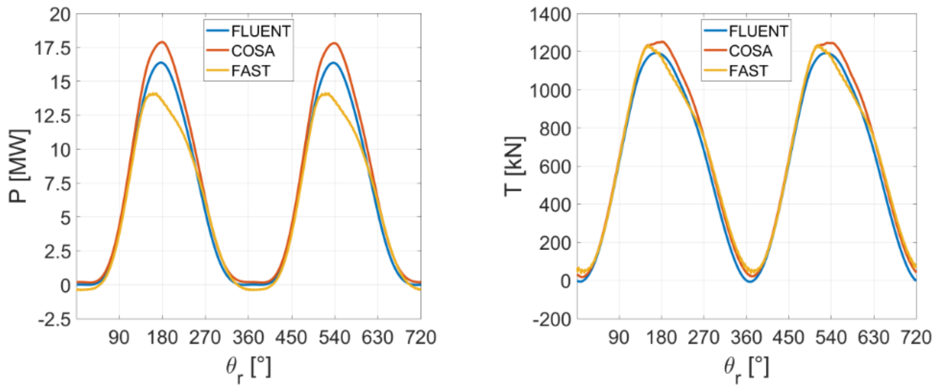

Figure 2.18: Discrepencies between CFD and BEM results due to compressibility effects, Ortolani et al. [19]

2.5. Test cases in the literature

Figures attached below depict the values of different test case parameters studied in the past, by using three different plots, namely ΔC_T vs. C_T, ΔC_T vs. V_{max} and A vs. k. All these parameters have been non-dimensionalized for proper correlation between different wind turbine models and inflow conditions across the publications. Figure 2.20 helps us visualize the relation between maximum change in thrust outputs concerning the maximum velocity attained during pitching. Figure 2.21 gives the relation between maximum change in thrust with respect to the mean thrust outputs while **??** gives the combinations of pitching amplitudes and thrusts used in the past. The parameters such as rotor's thrust T, pitching velocity V_p, and pitching frequency ω_p are non-dimensionalized according to the equations given by Equation 2.16 Equation 2.17 and Equation 2.18. The parameters C_T, V_{max}, and k represent the power output, the maximum velocity attained by the FOWT rotor during its motion, and the frequency of pitching motion respectively. Non-dimensionalizing these parameters helps us compare results and operating conditions from research easily.

$$C_T = \frac{T}{\frac{1}{2}\rho A V_\infty^2} \tag{2.16}$$

$$V_{max} = \frac{A_p \omega_p H_{hub}}{V_\infty} \tag{2.17}$$

$$k = \frac{\omega_p D}{V_\infty} \tag{2.18}$$

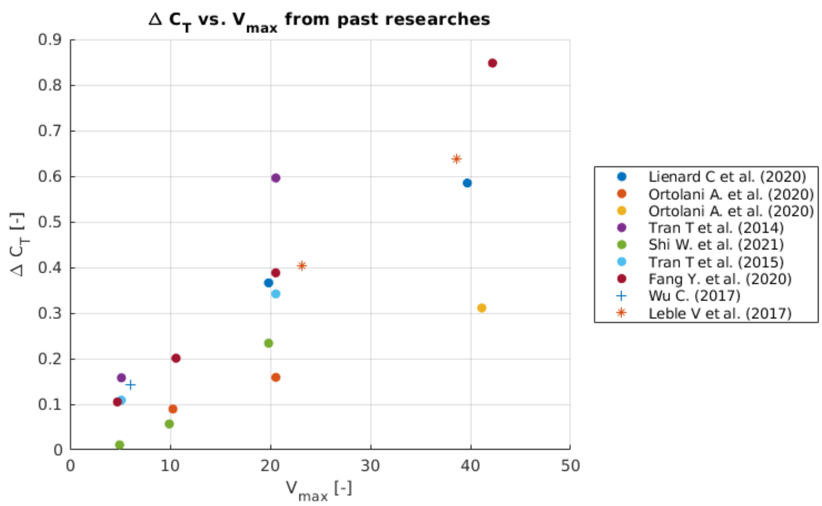

Figure 2.19: Plot between ΔC_T and V_{max} used in past research test cases

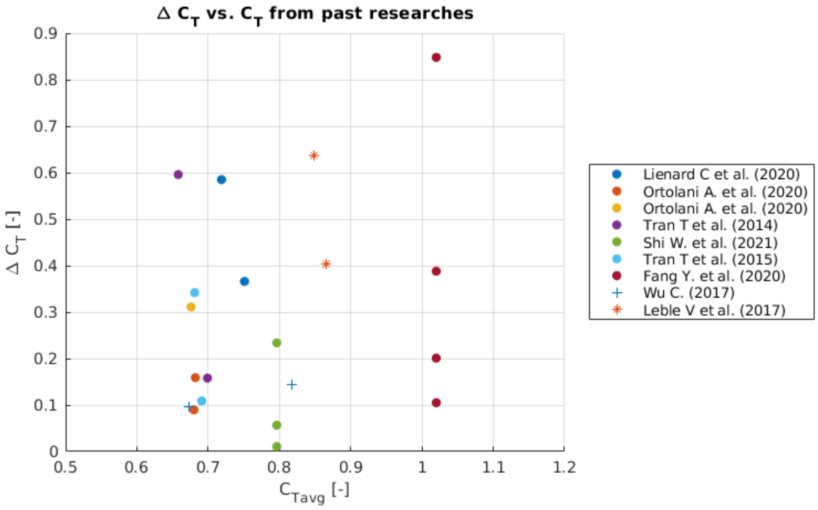

Figure 2.20: Plot between ΔC_T and C_T used in past research test cases

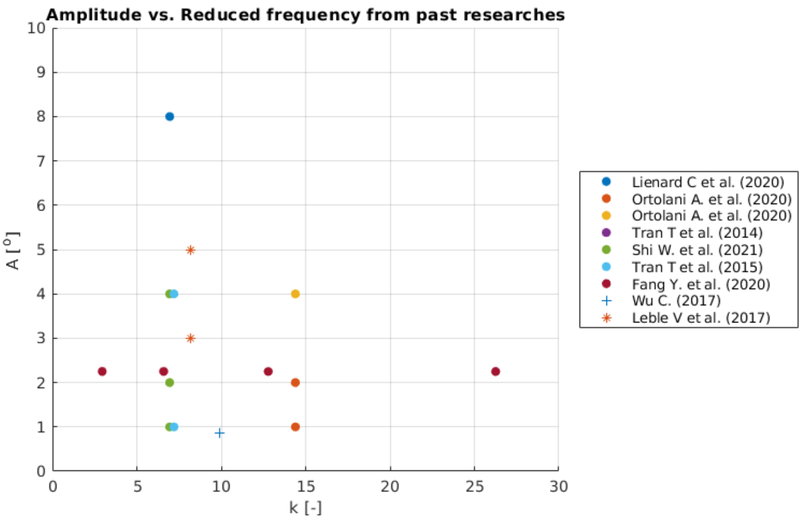

Figure 2.21: Plot between A and k used in past research test cases

3
Methodology

This chapter explains in detail the methodology used in this project for modelling a FOWT under platform-induced pitching motion. Section 3.1 contains the model setup of the corresponding actuator disk simulations. The chapter concludes by describing the BEM correction models tested in this project and the associated modifications, if any. Figure 3.1 gives an understanding of the parameters of pitching motion such as pitching amplitude θ_p and the velocity of pitching Ω_p. The line $a0c$ represents the actuator disk.

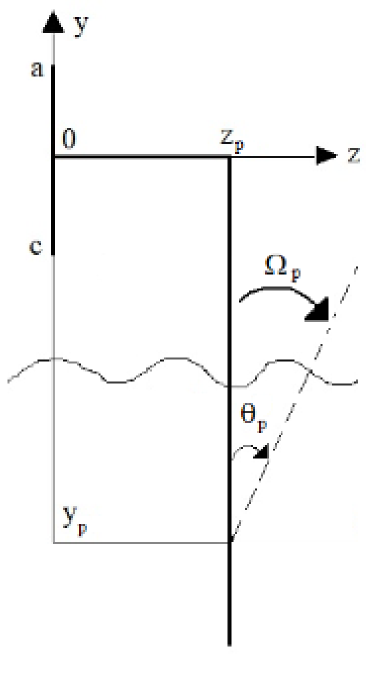

Figure 3.1: Illustration of the pitching amplitude and velocity [16]

CFD simulations in this project were developed and solved using an open-source CFD package, OpenFOAM. Therefore, the following sections will discuss the modifications made to pre-coded C++ libraries for actuator disk and actuator line CFD simulations. The following sections will discuss the process of computational model development and its validation. Following that, a detailed discussion of the modifications made to the pre-coded OpenFOAM libraries will be discussed.

3.1. Actuator Disk Model

An actuator disk simulation, as described in Section 3.1, attempts to model the wind turbine rotor by selecting a set of cells (a cylinder with infinitely small thickness) and applying momentum sources to them. Therefore, instead of adding a physical boundary to the computational domain, a set of cells is selected and momentum source is added to them. Thus, when the Navier-Stokes equations are solved inside these cells, only extra variables corresponding to the external force field are added. This requires much lesser pre-processing time and solving time when compared to a blade-resolved model or any model that involves the actual geometry of the wind turbine. The following sections explain the different steps involved in setting up an actuator disk model of a pitching FOWT wind turbine rotor.

3.1.1. Computational domain and model setup

As with any CFD simulation, the simulation process starts with setting up the computational domain and determining the grid resolution for optimal solutions. The process of determining grid resolution and domain size will be discussed in the following section. The current section contains the choices made in setting the simulation up.

Owing to the computational resource availability and requirements on the accuracy and physicality of results, the current set of simulations uses a RANS model to model turbulence. Owing to its accuracy in modelling external incompressible turbulent flows, the two-equation k-ϵ model was chosen for the CFD simulations conducted in this project. This turbulence model, along with the initial conditions for pressure and velocity, takes in k, ϵ, and ν_t also as initial conditions for turbulence modelling at the inlet. The formulae used for the calculation of these inlet conditions are provided in Equation 3.1, Equation 3.2, and Equation 3.3. The turbulence length scale (L) was chosen to be $0.07 * L_{ref}$ where L_{ref} is the reference length scale of the flow. This flow reference length scale was chosen to be 0.7 times the diameter of the rotor following the recommendation by Hamlaoui for HAWT simulations using actuator disk [95]. A separate turbulence intensity independence test was conducted, discussed in Section 3.1.4, as a part of the model validation process to study the influence of TI values on the induction field. However, all the other simulations use initial conditions that correspond to an ambient turbulence intensity of around 0.08% following the recommendations provided by Spalart and Rumsey [96] for accurate external aerodynamic analyses using the standard k-ϵ model.

$$k = \frac{3}{2}(I|U_{ref}|)2 \tag{3.1}$$

$$\epsilon = \frac{C_\mu^{0.75} k^{1.5}}{L} \tag{3.2}$$

$$\nu_t = C_\mu \frac{k^2}{\epsilon} \tag{3.3}$$

Figure 3.2 illustrates the computational domain used for Actuator disk model used in this project. Since a pitching rotor will possess symmetry along its center line(along Y-axis in this case), a half-rotor model of the computational domain is created. The side denoted by 'side1' in the figure is assigned with a **symmetryPlane** boundary condition so that the simulation takes into account a full actuator disk. The background mesh was created using GMSH [97], a third-party open-source three-dimensional meshing software package. This software produces a mesh file of **'.msh'** format. This is converted into an OpenFOAM mesh file using **gmshToFoam**. However, on using this mesh for CFD simulations, it was identified that the mesh resolution (at least at the actuator disk) is lower than necessary. Therefore a single refinement region was added near the actuator disk region using **topoSet** and **refineMesh** utilities in OpenFOAM. The utility **topoSet** was used to select a cylindrical region that extends up to 0.4D upstream and downstream of the actuator disk and has a radius of 0.75D. Upon using **refineMesh** to refine the selected region, all the cells are divided in half in all three directions (X, Y, and Z axes), thus resulting in 8 times the number of cells previously present in the refinement region. The boundary conditions imposed in the computational domain's boundaries are:

- Inlet: Uniform velocity - 11 m/s
- Exit: Zero gradient - 0 gauge pressure

- Side - 1: Symmetry boundary condition
- Side - 2: Wall - no-slip boundary condition
- Top: Wall - no-slip boundary condition
- Bottom: Wall - no-slip boundary condition

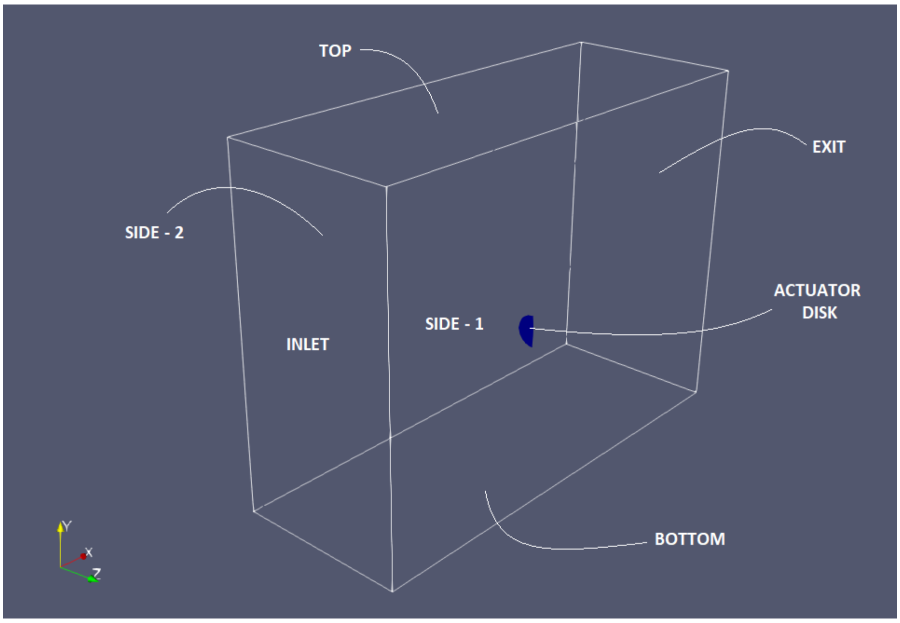

Figure 3.2: Illustration of the computational domain used for simulations

Once the refinement region is introduced, the next step in the process is to define a set of cells as the actuator disk to mimic the FOWT rotor. To accomplish this, again the **topoSet** utility of OpenFOAM is used. This utility defines a cylindrical cell set of very small thickness (about 1 cell width) at the origin. Once the cell set is selected and defined, the OpenFOAM class **actuationDiskSource** was used to define the selected cell region as a momentum source. It should be noted that this class was slightly modified to dynamically vary the magnitude and direction of thrust. The modified code is presented in Appendix E in the appendix. This class takes in data on thrust, power, and geometric specifications of the actuator disk and introduces momentum sources to the selected cell region. This particular mesh setup was used for convergence and validation studies, which involve stationary actuator disk simulations. But the mesh file as it is cannot be used for modeling the pitching motion of a FOWT because the actuator disk library used and the utility used to select the actuator disk region do not change with time and are capable of modeling only stationary actuator disks. Therefore, the dynamic mesh utility inside OpenFOAM is used to introduce movement to the actuator disk. The dictionary **dynamicMeshDict** contains the specifications about the motion of the cell zone in which the selected cell zone will be made to move as per the specified motion. The process of implementing dynamic meshes is not fully straightforward. So, it is broken down into simpler steps and is presented here.

3.1.2. Dynamic mesh and motion specification

Firstly, the topology of the computational domain needs an explanation as it is mainly developed particularly for the pitching motion or any rotatory mesh motions in general. It can be observed from Figure 3.3 that it contains a cylindrical region with the center slightly off from the location y=0. This is done to place the actuator disk exactly in between the top and bottom boundaries, i.e. at the origin of the domain (as it is present in the domain size independency cases). Since this CFD model tries to model an NREL 5MW wind turbine, the center of this cylindrical region is anchored at the location *(0, -0.714, 0)*. It could be confusing to understand why the location of the center of rotation is kept at $y = -0.714$. Since the model is parameterized with respect to the diameter of the 5MW NREL reference wind turbine, the ratio between the hub height and the diameter of the wind turbine is 0.714. That is, H_{hub} = $0.714 * D$. Therefore, by placing the center of rotation at (0, -0.714, 0), a wind turbine rotor that pitches about its platform is simulated.

The cuboidal region present in the middle makes the selection of actuator disk uniform thickness easier. A thin outer cylindrical region is added to facilitate a more efficient cell deformation and transfer of flow data from the dynamic region (master) to the stationary region (slave).

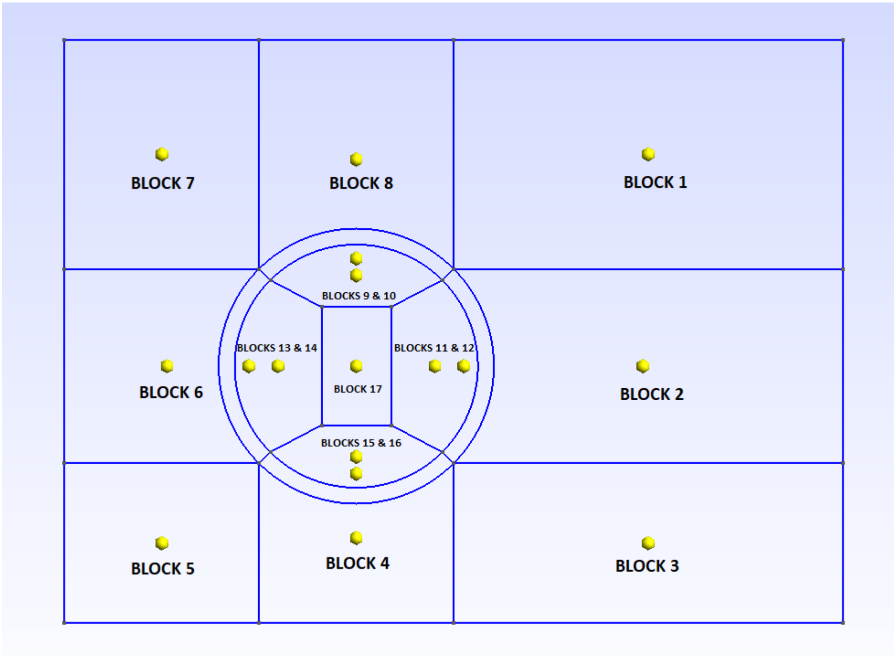

Figure 3.3: Illustration of the computational domain's topology

It should also be noted that the interface between the master and slave regions of the mesh needs to be assigned as a separate set of patches to implement the dynamic motion. This interface patch will later be duplicated to create two different baffles namely 'masterAMI' and 'slaveAMI'. This is achieved by using the utility **createBaffles** [98] in OpenFOAM.

Dynamic mesh implementation
As discussed earlier, the inner cylindrical region will be the dynamic part of the mesh, while the rest of the mesh will be stationary. To achieve this, the 3D computational mesh domain was created from the mesh topology illustrated in Figure 3.3. Along with the cell zone definition for actuator disk using **topoSet**, the cell zone which will act as the dynamic part of the mesh will also be defined. Therefore, two cell zone assignments are done in this part:

- The first cell zone, which consists of a thin cylindrical region with normal in X direction that will act as the actuator disk.
- The second cell zone, which consists of a cylindrical region with normal in Z direction that will be the dynamic part of the mesh.

Further, using the dictionary **dynamicMeshDict**, the master cell zone is imposed with an oscillatory-rotatory motion. From the list of readily available solid body motion functions within dynamicMesh library, the utility **oscillatingRotatingMotion** is used for imposing this motion. Using this utility, a sinusoidal pitching motion on the rotor can be readily imposed by defining the center of rotation (which is *(0, -0.714, 0)* in this case), amplitude, and frequency of pitching.

3.1.3. Modifications to other libraries
Another OpenFOAM's in-built library was modified for usage in this project. The changes made to **actuationDiskSource** along with the respective reasons are enlisted below:

- **Velocity monitoring:** For the calculation of thrust from C_t values, the **actuationDiskSource** class originally takes in the velocity at the monitor cells defined in **fvOptions**. But, for accurate calculation of thrust from C_t, it is essential to choose a cell where the velocity is undisturbed by the actuator disk. To eliminate this risk, the velocity magnitude at the inlet is directly used for calculating the thrust (instead of the velocity at the monitor cells).
- **Thrust calculation:** The original variable scaling method calculates thrust using the formula:

$$F_T = \frac{1}{2}\rho A_d \left| u_d \cdot n \right|^2 C_T^* \tag{3.4}$$

where

$$C_T^* = C_T(\frac{|u_m|}{|u_m|})^2 \tag{3.5}$$

where, A_d is the area of disk, u_d is the average velocity at the actuator disk and u_m is the averaged velocity in the monitor region.
However, since in this particular set of simulations, u_d and u_m are essentially the same, the values of C_T and C_T^* are going to be same. Therefore, the concept of C_T^* is eliminated and the thrust force is directly calculated using the formula:

$$F_T = \frac{1}{2}\rho A_d U_\infty^2 C_T \tag{3.6}$$

- **Dynamic thrust coefficient:** For the unsteady cases, the thrust coefficient of the rotor is also varied dynamically. This change in C_T is made to follow the oscillatory motion of the actuator disk. Thus the value of C_T is made to vary according to the equation:

$$C_T(t) = C_{T_0} - \Delta C_T cos(2\pi f t + \phi) \tag{3.7}$$

where $C_T(t)$ is the mean thrust coefficient of the actuator, C_{T_0} is the baseline thrust coefficient, ΔC_T is the change in thrust coefficient introduced, f is the frequency of pitching motion and ϕ is the phase difference between pitching motion and the change in thrust coefficient. Value of ϕ is maintained at $\phi = 0^o$ unless specifically mentioned.

3.1.4. Grid independence and Model validation

Since studying the induction field in a pitching rotor is one of the primary goals of this project, the model has been validated by comparing the rotor-averaged axial induction obtained from CFD results with the analytical results obtained using empirical relations based on momentum theory. In the current model validation study, the independence studies mentioned below were performed:

1. Domain size independence
2. Grid size independence (Mesh refinement)
3. Ambient turbulence intensity independence
4. Reynold's number independence

Induction Calculation

From the plot of U_x vs. distance from rotor (Figure 3.4) obtained from CFD results, a discontinuity is observed in the velocity field when it crosses the actuator disk. This does not represent any physical phenomenon and is purely a numerical phenomenon that occurs due to the presence of cells that impart momentum to the flow. Thus, this discontinuity has to be removed from the velocity data before calculating the velocity at the rotor. Therefore, the velocity U_x at the rotor disk was calculated by linear interpolation (as the velocity profile looks close to linear near the rotor disk). This interpolated value of U_x was later used to calculate the induction at the rotor.

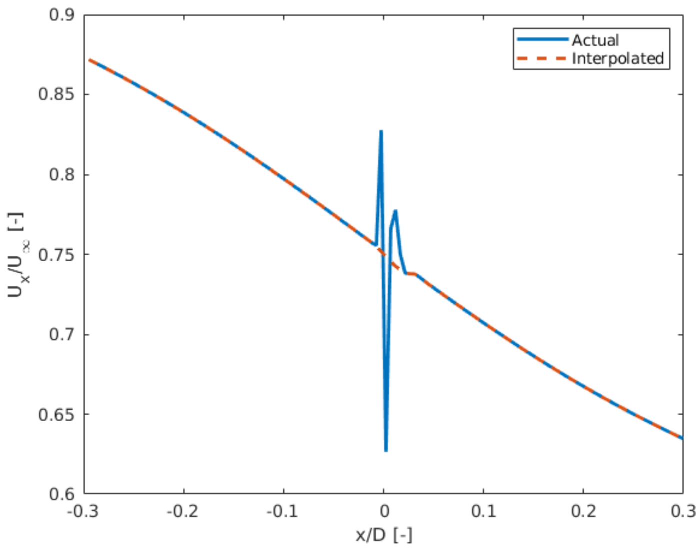

Figure 3.4: Method of interpolation used to calculate the velocity at the actuator disk

The velocity field is captured along a line corresponding to the rotor azimuth of $\phi = 0^o$ from $r/R = -1$ to $r/R = 1$. It is essential to keep this in mind while trying to understand the results presented in Section 4.2.4. The induction field captured at $\phi = 0^o$ is assumed to be the induction field corresponding to the other azimuthal angles too That is, the azimuthal variation of the induction field due to rotor tilt is disregarded in this method of calculation (i.e. $a_{\phi=0^o} = a_{\phi\neq0^o}$). Since the platform pitching motion is angular, the effects that arise purely due to the pitching motion of the actuator might be slightly exaggerated.

The rotor averaged induction was calculated using Equation 3.8

$$a_{avg} = \frac{\sum_{i=1}^{N} a(\phi = 0^o)_i \cdot \pi(r_i^2 - r_{i-1}^2)}{\pi R^2} \tag{3.8}$$

where a_i is the axial induction corresponding to i^{th} rotor annulus and r_i is the radial position of the i^{th} annulus. This rotor averaged induction from CFD results was compared with the analytical results for axial induction obtained using Equation 3.9[99].

$$C_T = \begin{cases} 4a_{avg}(1 - a_{avg}) & a_{avg} \leq \frac{1}{3} \\ 4a_{avg}\left(1 - \frac{1}{4}(5 - 3a_{avg})a_{avg}\right) & a_{avg} > \frac{1}{3} \end{cases} \tag{3.9}$$

In the following sub-sections, a detailed description of the test cases used to validate the computational domain is provided.

Domain size and grid size independence

To perform this study, a sample domain was created with dimensions: X_{up} = $6D$, X_{down} = $10D$, Y_{in} = $12D$ and Z_{in} = $6D$. With these dimensions, a background mesh was created as illustrated in Figure 3.5. It should be noted that the grid size independency studies have been performed on a different mesh which has a different topology from the current mesh. Details on that mesh and the reason it was not used in this project is presented in the appendix. That particular mesh was not used further in any of the dynamic tests because of the discontinuity issue observed in the actuator disk region. More details on this problem are provided in the appendix section.

As mentioned earlier, an additional refinement zone was added near the region of the actuator disk. This region is depicted in Figure 3.6. For the grid size independency tests, the number of cells in the Z direction is changed. Thus, the cell thicknesses and lengths (in Y direction) are not changed but the cell width (in the Z direction) is the only parameter that changes from one mesh to another.

It is noteworthy that the cell lengths in the Z direction have a small progression (of value 1.02) to it, such that every next cell in the Z direction will have a width 1.02 times that of the previous cell $(W_{i+1} = 1.02 * W_i)$. This progression is introduced to reduce the total number of cells in the mesh grid and also have a finely refined mesh near the actuator disk. In the coarsest mesh, the number of cells in the Z direction is 70. It is slowly increased to a value of 170 in the finest mesh grid. Table 3.2 gives the accuracy in results obtained from grids with the number of cell divisions in the Z direction. In the table, the column 'smallest cell width' gives the width of the smallest cell in the actuator disk (the last cell Z direction). Accuracy of the mesh grid is provided by presenting the error observed in disc-averaged inductions corresponding to $C_T = 0.8$. The theoretical value of axial induction corresponding to $C_T = 0.8$, calculated using Equation 3.9, is $a = 0.2764$.

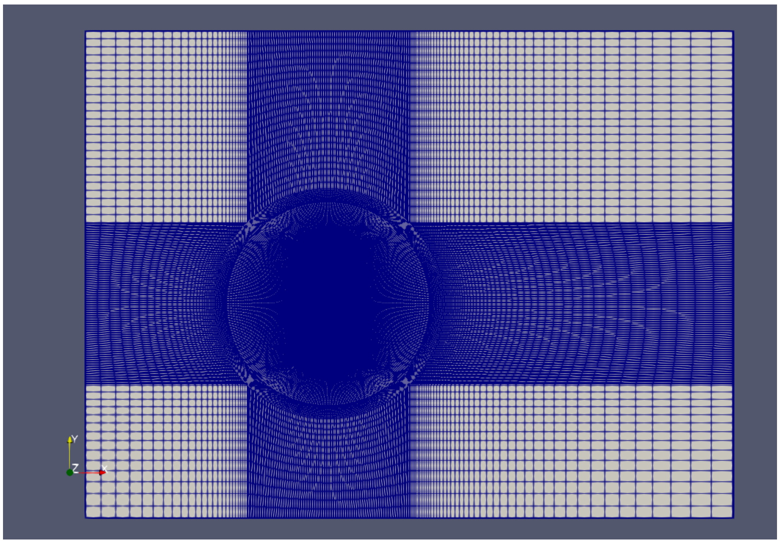

Figure 3.5: Background mesh grid created using GMSH meshing package

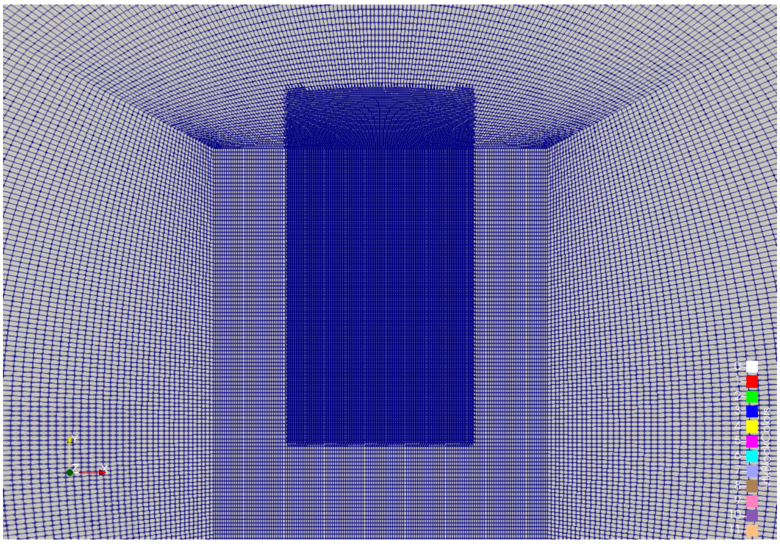

Figure 3.6: Zoomed-in view of the refinement region added in the vicinity of the actuator disk.

Table 3.1: Domain size independence study: Domain sizes and corresponding errors

Case #	X_u	X_d	Y_u	Y_d	Z	a_{avg}[]	Absolute error (%)
AD_1	3	10	6	6	6	0.2574	6.8552
AD_2	9	10	6	6	6	0.2718	1.6599
AD_3	12	10	6	6	6	0.2742	0.7769
AD_4	6	7	6	6	6	0.2692	2.6002
AD_5	6	13	6	6	6	0.2741	0.8230
AD_6	6	16	6	6	6	0.2739	0.9140
AD_7	6	10	3	3	6	0.2696	2.4629
AD_8	6	10	9	9	6	0.2729	1.2485
AD_9	6	10	12	12	6	0.2731	1.1745
AD_10	6	10	6	6	3	0.2696	2.4711
AD_11	6	10	6	6	9	0.2704	2.1510
AD_12	6	10	6	6	12	0.2731	1.1779
AD_13	6	10	6	6	6	0.2708	1.4126

As observed from Table 3.1, it can be noted that the distance of grid boundaries from the actuator disk has a significant influence on the induction field and also the averaged induction values on the actuator disk. Out of all the parameters changed, the least significant parameter seems to be the distance downstream in X direction (X_d). X_u has the most significant influence on rotor averaged induction as it plays a crucial role in flow development and numerical stability which in turn is crucial for stable and accurate CFD results. Thus, more accurate results are obtained as the domain boundaries move away from the actuator disk. The same trend is observed in the distances of boundaries in Y and Z directions also. As the domain sizes in these directions are increased, better results are observed. Therefore, taking both the accuracy of results and availability of resources into account, the reference domain itself was used for all the further CFD analyses.

Table 3.2: Grid refinement levels and corresponding errors

Number of cells	Min cell length in z-direction (z/D)	a_{avg}[-]	Absolute error [%]
6.1M	0.02	0.2865	3.654
9M	0.0098	0.2772	0.289
11M	0.0063	0.2755	0.326
13.2M	0.004	0.2770	0.217
16.6M	0.0025	0.2767	0.108

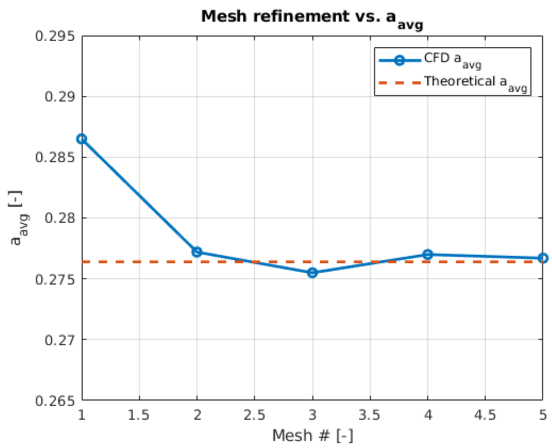

Figure 3.7: Influence of mesh refinement on calculated average induction

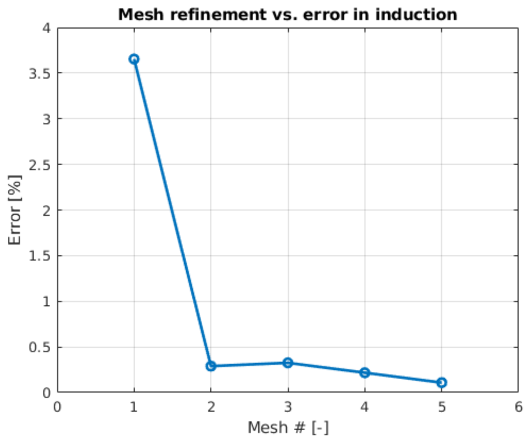

Figure 3.8: Influence of mesh refinement on calculated average induction's errors

As indicated by Table 3.2, the error progressively reduces with an increase in the number of cells in the Z direction. An oscillatory behaviour is observed in the trend of averaged induction and errors. There can be two reasons for this behaviour. One is that the solution itself is oscillating with respect to mesh refinement, while the other can be the method used to calculate induction. Regardless of the number of cells in the actuator disk, velocities from only a few particular locations on the actuator disk are used to calculate the induction field. Since the resolution of data extraction does not increase with the mesh resolution, an error might be introduced in the calculation and thus result in a slightly different value than expected. The mesh number 3 is used for further analyses because it is capable of delivering accurate enough results with an error percentage of around 0.3% and is also computationally much cheaper than meshes 5 and 6.

Reynolds number and Turbulence intensity dependency

As the optimal grid refinement levels and domain sizes are calculated, the next step in the process is to study the dependency of results on Reynolds number Re and turbulence intensity I. Even though the effect of these two parameters is expected to be marginal, it is still necessary to test and choose the optimal inflow parameters for accurate aerodynamic studies[96]. Therefore, on the final domain obtained from previous studies, analyses with different Re and I are conducted to study their effects and choose the optimal inflow conditions.

Table 3.3: Reynolds number independence study results and corresponding errors

Re [-]	a_{avg}[-]	Absolute error [%]
1.00E+05	0.2752	0.4341
1.00E+06	0.2754	0.3618
1.00E+07	0.2755	0.3256
1.00E+08	0.2755	0.3256

From Table 3.3, it can be observed that the flow Reynolds number does not have a significant influence on the induction values of the actuator disk. Only a slight increase in rotor-averaged induction is observed with a change of less than 1%. Therefore, it can be safely assumed that the flow Reynolds number, at least within incompressible turbulent range, does not have a significant averaged influence on the induction field of the rotor. Therefore, a Reynolds number of $Re = 5E^6$ was used for all the further analyses in this project. A very similar observation was made for turbulence intensity tests too. As observed in Table 3.4, the value of a_avg barely changes with turbulence intensity levels. For the sake of reliability, a turbulence value of 0.08% is used for all the analyses, as recommended by Spalart et al. [96] for accurate aerodynamic calculations using k-ϵ RANS turbulence model.

Table 3.4: Turbulence intensity independence study results and corresponding errors

TI [%]	a_{avg}[-]	Absolute error [%]
0.01	0.2756	0.2894
0.1	0.2755	0.3256
0.5	0.27545	0.3437
1	0.2754	0.3618
2	0.2754	0.3618

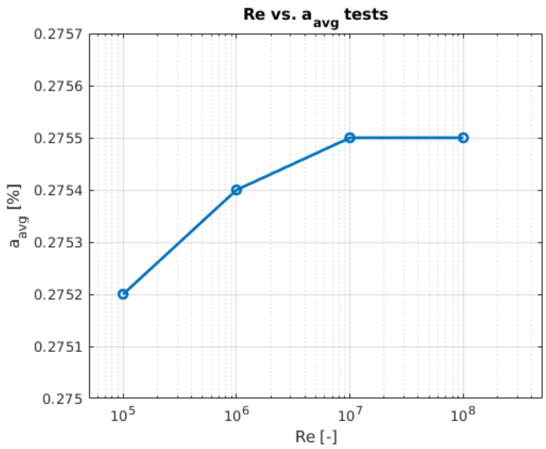

Figure 3.9: Influence of flow Reynolds number on calculated average induction

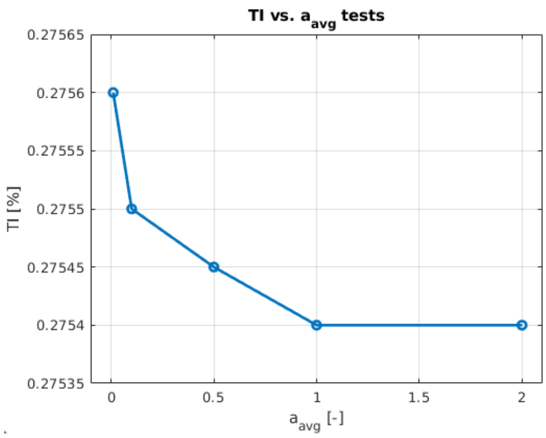

Figure 3.10: Influence of turbulence intensity on calculated average induction

Model validation against momentum theory for normal cases

In this section, the model's results for other values of C_T are checked for accuracy against results from momentum theory. The theoretical induction values are obtained from Equation 3.9 which also takes into account Glauert's correction for heavily loaded rotors. From Figure 3.11, it can be observed that the results obtained from CFD match perfectly for lower values of thrusts, that is $C_T < 1$. A slight difference between calculated CFD results and results from momentum theory is observed at high load cases. It should also be noted that the location at which axial velocity is sampled/calculated influences the value of induction calculated and this influence is much higher in high C_T cases. However, the difference in results observed can also be attributed to the fact that Glauert's correction is only one of the possible fits to sparse experimental data [100].

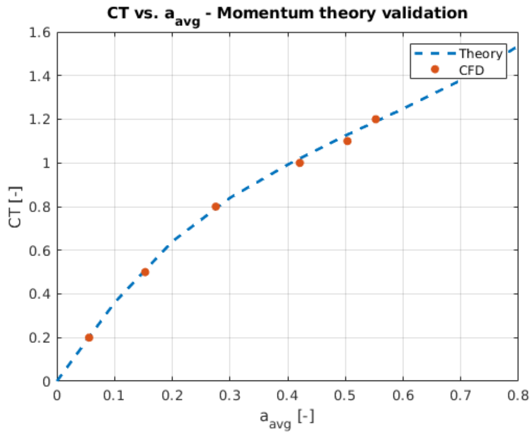

Figure 3.11: Validation against momentum theory for different C_T of disks

Model validation against momentum theory for yawed cases

This section presents the results obtained for the purpose of model validation against momentum theory and Glauert's theory for yawed actuator disk. These cases also were tested with a specification of C_T = 0.8. However, as expected the observed C_T will be lower than the prescribed value the actuator disk is not normal to the flow. In **??**, the rotor averaged induction calculated from CFD results is compared with rotor averaged induction calculated from momentum theory. As can be observed from the error percentages, the CFD results agree greatly with the average induction calculated using the momentum theory given in Equation 3.10.

$$C_{T_{yaw}} = 4 * a_{axial} * (cos(\theta_{yaw}) - a_{axial}) \tag{3.10}$$

$$a_{yaw}(r) = a_{axial} * (1 + tan(\chi/2) * ((\frac{r}{R}) * sin(\psi))) \tag{3.11}$$

In the equations given above, a_axial is the rotor averaged axial induction, θ_{yaw} is the yaw angle, χ is the wake angle and ψ is the azimuthal angle. It should be noted that the wake angle is calculated using a different formula as opposed to Glauert's proposal. Jimenez [101] proposed a novel method to calculate the wake angle by considering the momentum change in lateral direction also. This gives rise to Equation 3.12.

$$\chi{=}(cos^2\theta_{yaw} sin\theta_{yaw} C_T)/2 + \theta_{yaw} \tag{3.12}$$

?? provides the comparison between the results calculated using glauert's theory and CFD simulations. The table compares the value of C_T calculated for yaw angles $\theta_{yaw} = -10^o$ and $\theta_{yaw} = 10^o$. The CFD model slightly under-predicts the values of C_T when compared to the momentum theory results. This behaviour is expected given the tendency of engineering models to over-predict the results due to their inability to account for complex effects such as viscous effects. Since the model will be used for testing the accuracy of yaw engineering models also, it is essential to check the radial distribution of the induction field. For this purpose, a reference case from [102] at high yaw angle is modelled and tested for accuracy. The comparison between the CFD-predicted results and vortex model predicted results is provided in Figure 3.12. This case corresponds to a wind turbine with $C_T = 0.64$ and at an yaw angle of $\theta_{yaw} = -30^o$. The CFD predicted result for axial induction shows decent accuracy when compared to the reference results.

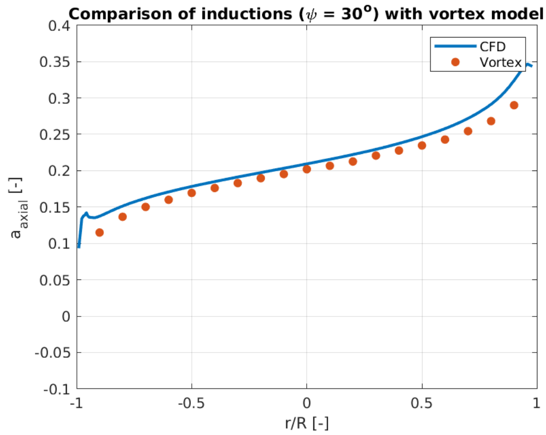

Figure 3.12: Validation against Glauert theory for θ_{yaw} = -30^o

3.2. BEM correction Models

This section provides the description (along with modifications made, if applicable) of the BEM-based models that have been tested for accuracy in this thesis project. As discussed in Section 1.3.1, yaw correction models and a dynamic inflow model will be tested by comparing their results with the results obtained from actuator disk CFD simulations.

3.2.1. Yaw correction models

A lot of yaw correction models have been developed recently, some being totally novel and some being a derivative of an old model. As far as this thesis is concerned, the models which do not include tip correction are discussed because using an actuator disk model, the tip losses are anyway not perfectly captured. Therefore, this thesis only deals with the models that are derived from Glauert's yaw correction model[54]. Since the basis of these models are the same and the method by which these models are derived is not the focus of this thesis, only the equations corresponding to the yaw correction are presented here. Glauert's correction model is presented in **??** and the models presented below are derivatives of Glauert's model. The yaw models tested in this thesis are:

- **Pitts Peter's yaw (original) correction model:**

$$a_{yaw} = a_{avg}(1 + \frac{15\pi}{32} tan(\chi/2)\frac{r}{R} sin(\psi)) \tag{3.13}$$

- **Pitts Peter's yaw (updated) correction model:**

$$a_{yaw} = a_{avg}(1 + \frac{15\pi}{64} tan(\chi/2)\frac{r}{R} sin(\psi)) \tag{3.14}$$

- **White and Blake's yaw correction model:**

$$a_{yaw} = a_{avg}(1 + \sqrt{2} sin(\chi)\frac{r}{R} sin(\psi)) \tag{3.15}$$

- **Oye's yaw correction model:**

$$a_{yaw} = a_{avg}(1 + \mathbf{F} tan(\chi/2)\frac{r}{R} sin(\psi)) \tag{3.16}$$

  where $\mathbf{F} = (\frac{r}{R})^2 + 0.4(\frac{r}{R})^4 + 0.4(\frac{r}{R})^6$

3.2.2. Dynamic inflow model

This dynamic inflow model was developed by Carlos S. Ferreira [3], particularly for surging FOWTs. This model takes into account the dynamic response of the rotor due to platform motions. Studies discussed in Section 2.4.1 suggest that the dynamic response of an unsteady rotor or a rotor under unsteady wind conditions produces a dynamic response that undergoes an exponential decay with time.

Following the same suggestion, this model also assumes the dynamic response of a surging actuator disk to be a function of exponentially decaying components. This section just briefly explains the model, but a more complete explanation of the working of this model is provided in [3].

Since BEM theory is applicable only in an inertial frame where the rotor and the stream tube are static, the model uses different reference velocities for its induced velocity calculations. They are u_{str} (induction velocity inside the stream tube) and u_{act} (induction velocity at the actuator disk). Accompanying these two velocities, the model also uses two different sets of time scales corresponding to the actuator disk scale induction effects (τ_{act_1} and τ_{act_2}) and the stream tube scale (τ_{str}) effects. These time scales are calculated using the case's operating conditions using Equation 3.17, Equation 3.18, and Equation 3.19.

$$\tau_{str} = \frac{L_{str}}{U_{\infty_{\text{ref}}} - \frac{u_{str}}{2}} \tag{3.17}$$

$$\tau_{act_1} = \frac{L_{act}}{U_{\infty} - \frac{u_{act}}{2} - v_{act}} \tag{3.18}$$

$$\tau_{act_2} = \frac{L_{act}}{U_{\infty_{ref}} - \frac{u_{act}}{2}} \tag{3.19}$$

In the above equations, L_{str} and L_act represent the length scales of the stream tube and actuator disk respectively. v_{act} represents the pitching velocity of the actuator disk. $U_{\infty_{ref}}$ and U_{∞} are the free stream velocity in the inertial frame and global free stream velocities. For an actuator disk under oscillating surge or pitch motion, reference velocity is equal to that of the global frame, i.e. $U_{\infty_{ref}}$ = U_{∞}. The stream tube induction velocity and actuator disk induction velocities are found using the low pass filter functions that are represented by Equation 3.22 and Equation 3.21 respectively. The variable u_{qs} denotes the quasi-steady solution for induction velocity which is calculated from U_{str} and C_T using the formula presented in Equation 3.20. It should be noted that U_{str} is the global stream tube velocity while u_{str} denotes the induction velocity of the stream tube.

$$u_{qs} = \frac{C_T U_{\infty}^2}{4} \frac{1}{U_{str}} \tag{3.20}$$

$$u_{act_{(t+\Delta t)}} = u_{act_{(t)}} e^{-\frac{\Delta t}{\tau_{act_1}}} + u_{qs} \left(1 - e^{-\frac{\Delta t}{\tau_{act_2}}}\right) \tag{3.21}$$

$$u_{str_{(t+\Delta t)}} = u_{str_{(t)}} e^{-\frac{\Delta t}{\tau_{str}}} + u_{qs} \left(1 - e^{-\frac{\Delta t}{\tau_{str}}}\right) \tag{3.22}$$

The equations Equation 3.21, Equation 3.22 provide the final calculated velocities at the actuator disk and velocity of the stream tube respectively for each time step t. By calculating the values of u_{act} and u_{str} for multiple time steps (ranging from $t/T = 0$ to $t/T = 1$), the trend of dynamic response on the induction field is captured through a surge cycle. Using the calculation of u_{act}, the disk trend of disk-averaged induction is obtained for a surging actuator disk. It is again emphasized that this particular dynamic inflow model is calibrated for surging actuator disks. Since the wake characteristics of a pitching rotor will be different from that of a surging actuator disk, the dynamic effect due to the vortices downstream is also expected to be different. However, it is also expected to provide results with reasonable accuracy because the effect of the rotor's yaw while pitching at small angles might not be significant enough to create a big difference in the induction field of the rotor. Therefore, it is still worthwhile to test the applicability of the current dynamic inflow model for pitching motions also.

4 Results

This chapter contains the results obtained from actuator disk simulations carried out through the course of this project. This chapter starts with a preliminary discussion of the steady actuator disk results in Section 4.1 where both the thrust prescription and motion prescription are constant. Following that, a detailed discussion on unsteady results will be discussed in Section 4.2.

In this section, discussion on the three kinds of actuator disk simulations will be discussed. Firstly, the cases with a still actuator disk and varying thrust prescription will be discussed. This is followed by a discussion of cases with a pitching actuator disk with constant thrust prescription. Finally, the cases with a pitching actuator disk and dynamic thrust prescription will be discussed. Within each section, firstly a preliminary discussion of the aerodynamics of that particular type of simulation is done. Following that, the same case with a higher frequency of pitching is compared and contrasted to analyse the effects of higher frequency. Following that, a case (of the same kind) with a lower specified thrust is presented and discussed to analyse the effects of thrust specification on the aerodynamics of the actuator.

4.1. Steady actuator disk results

In this section, steady case results will be discussed. Since the results of a steady actuator disk are mostly known to the research community and have already been discussed to an extent in the model validation section (Section 3.1.4), the current section will not dive deep into the discussion of the results. However, it is necessary to check if the model is capable of predicting Turbulent Wake States (TWS) and Vortex Ring States (VRS). Since these two operating states of a wind turbine are expected to occur in a floating offshore wind turbine undergoing platform motions, checking the computational model's capability to predict these two states is essential. This will help later in understanding the wake states that occur in dynamic cases better.

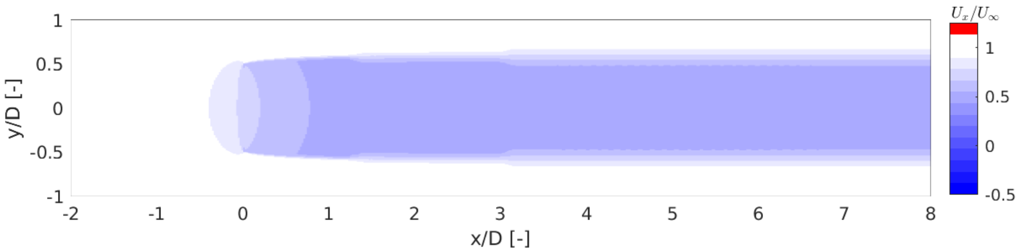

Figure 4.1: Contour of U_x/U_∞ showing TWS downstream of the actuator disk with $C_T = 0.8$

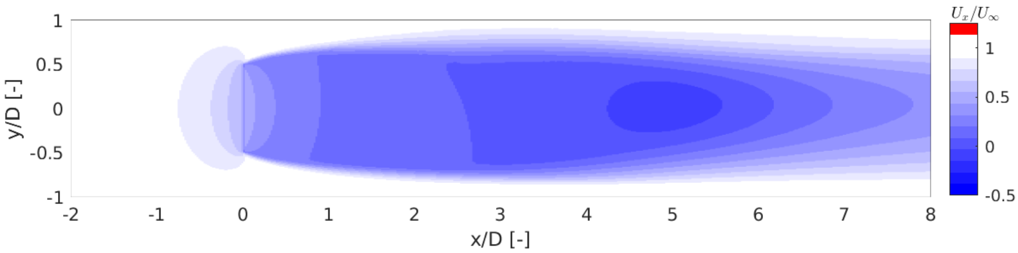

Figure 4.2: Contour of U_x/U_∞ showing TWS downstream of the actuator disk with $C_T = 1.1$

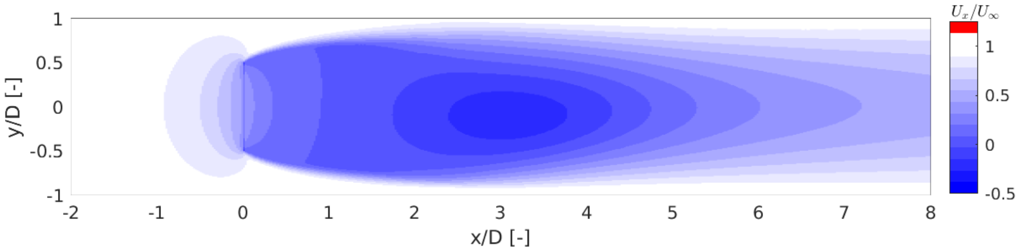

Figure 4.3: Contour of U_x/U_∞ showing TWS downstream of the actuator disk with $C_T = 1.2$

A visible region of recirculation, marked by negative values of U_x/U_∞, is observed in the wake region of Figure 4.2 and Figure 4.3. However, the contour plot presented in Figure 4.1, corresponding to $C_T = 0.8$, does not show any sign of recirculation in the wake. This verifies the fact that TWS states occur at high C_T values ($C_T > 1$) and not at lower values of C_T, that is at $C_T < 0.8$. More than verifying the fact that the TWS occurs at high C_T, these contour plots show the capability of the actuator disk CFD model to predict the occurrence of complex flow states such as TWS.

4.1.1. Yaw correction models comparison

In this section, a comparative analysis of the induction field predicted by the actuator disk CFD model and the BEM-based yaw correction models is done. This is done by plotting the radial distribution of axial inductions along the vertical of the actuator (corresponding to $\psi = 0^o$). It should be noted that the tip effects are not accounted for in any of the models discussed in this section (except for White and Blake's model). Also, to provide an objective view, the values of a_{avg} fed into the yaw correction models corresponds to the a_{avg} calculated using momentum methods. Before discussing the yawed cases, it is essential to compare the induction results predicted by the yawed case with the CFD induction field. Figure 4.4 provides the comparison of the same. It should be noted that the results predicted by yaw correction models are not individually visible because they overlap each other. Since the wake angle is zero, the value of Coleman's constant ($K(\chi) = 0$) drops to zero and there will be no difference between the predictions of yaw models. However, this provides an understanding of the disparity between results from momentum theory and CFD simulations.

$$a_{avg} = \sum_{i=1}^{N} a(\phi = 0^o)_i / N \tag{4.1}$$

$$\Delta a_{avg}[\%] = \frac{\sum_{i=1}^{N} (a_{i_{CFD}} - a_{i_{eng}})}{a_{avg}} * 100 \tag{4.2}$$

Table 4.1: Cumulative error (%) of induction field produced by the Yaw correction models

Yaw angle	Coleman	Oye	Pitts Peters	Pitts Peters (updated)	White and Blake
5	-0.8321	-0.7858	-0.9221	-0.6708	-0.2114
-5	-0.7912	-0.7113	-0.8914	-0.6117	-0.1006
10	-2.7984	-2.663	-3.1255	-2.2122	-0.5811
-10	-2.583	-2.4168	-2.9215	-1.9762	-0.2878
15	-4.143	-3.889	-4.7923	-2.9805	0.1315
-15	-4.1277	-3.8568	-4.7794	-2.9596	0.1655

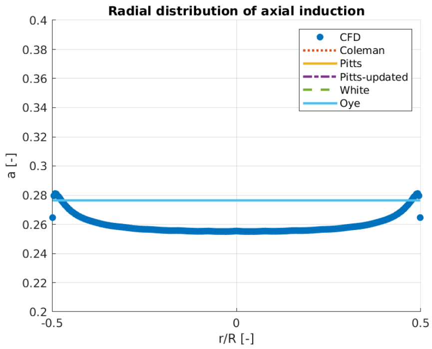

Figure 4.4: Comparison of induction field obtained from CFD results with yaw correction model results for $\theta_{yaw} = 0^o$

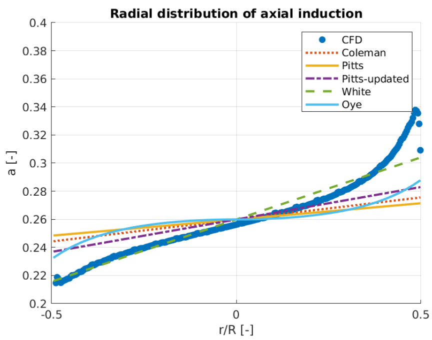

(a) $\theta_{yaw} = 5^o$

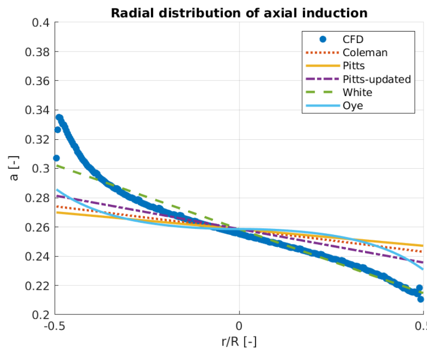

(b) $\theta_{yaw} = -5^o$

Figure 4.5: Comparison of induction field obtained from CFD results with yaw correction model results for $\theta_{yaw} = 5^o$ and $\theta_{yaw} = -5^o$

$$\Delta a_{avg}[\%] = \frac{\sum_{i=1}^{N}(a_{i_{CFD}} - a_{i_{eng}})}{a_{avg}} * 100 \tag{4.3}$$

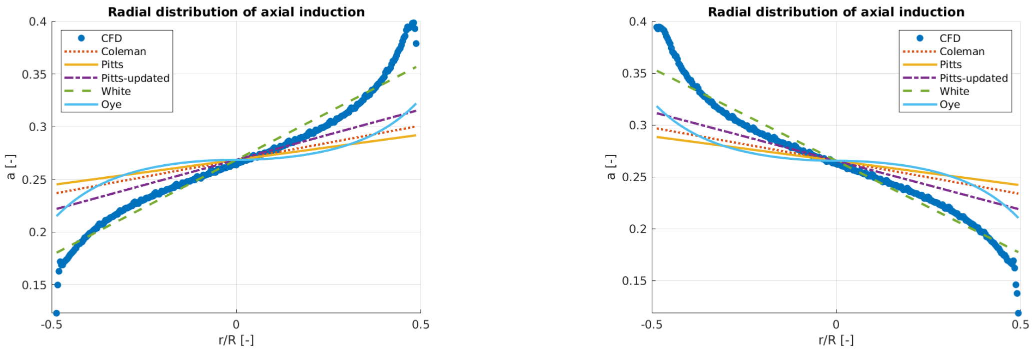

(a) $\theta_{yaw} = 10^o$ **(b)** $\theta_{yaw} = -10^o$

Figure 4.6: Comparison of induction field obtained from CFD results with yaw correction model results for $\theta_{yaw} = 10^o$ and $\theta_{yaw} = -10^o$

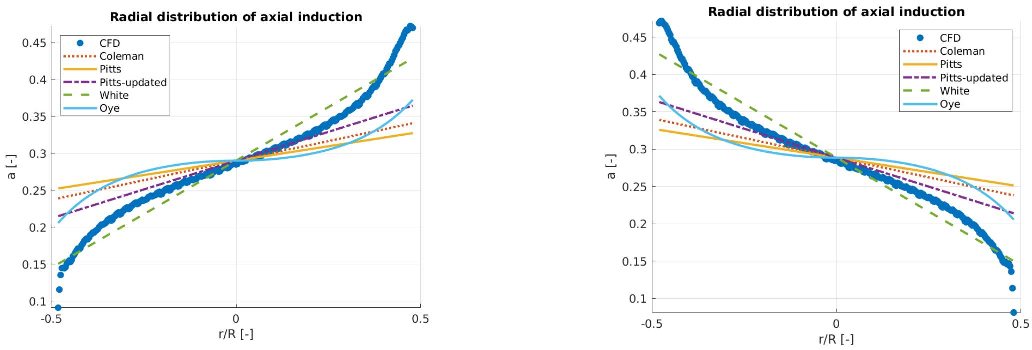

(a) $\theta_{yaw} = 15^o$ **(b)** $\theta_{yaw} = -15^o$

Figure 4.7: Comparison of induction field obtained from CFD results with yaw correction model results for $\theta_{yaw} = 15^o$ and $\theta_{yaw} = -15^o$

The primary observation made from these plots comparing the induction fields of CFD with yaw models is that the values of axial induction calculated by CFD are lesser than the inductions predicted by momentum methods. This is because of the general tendency of BEM models to overpredict the inductions compared to CFD results. The value of a_{axial} provided to the yaw models is calculated by calculating the mean of a_{axial} at all the annular elements along $\psi = 0^o$ (formula given in Equation 4.1. Another important observation made from these plots is that the induction fields predicted by the engineering models do not account for the vortices that arise from the (top and bottom) edges of the actuator disk. Therefore, the induction fields predicted by the momentum-based yaw correction models are linear and do not show non-linear behaviour near the tip and root. Therefore, it is important to judge the efficiency of these yaw correction models by mainly observing the slope of inductions predicted by them. The tip and hub loss corrections are anyway going to get added on top of the induction fields predicted by yaw correction models. Therefore, they must capture the slope of the induction field properly.

Upon observing Figure 4.5 visually, which correspond to $\theta_{yaw} = \pm 5^o$ it can be seen that the updated Pitts and Peter's model and White and Blake's model come closest to the results predicted by the CFD model with respect to the slope of the induction field. Between these two models, White and Blake's model comes closest to CFD results with the predicted slope nearly equal to that of the average slope of the CFD-predicted induction field. Coleman's model and original Pitts and Peter's model give the worst predictions of induction fields. The predictions of White and Blake's model are closer to CFD results on the far side of the actuator. That is, region $r/R = 0$ to $r/R = 0.5$ in Figure 4.5a and region $r/R = 0$ to $r/R = -0.5$ in Figure 4.5b. Even though Oye's model is capable of capturing the tip and hub effects, it does not do a good job of predicting the slope of the induction field well. Therefore, qualitatively, Oye's model with appropriate corrections for wake angle calculation should give the best results. In general, except for White and Blake's model, all the other yaw models tend to under-predict the magnitude of the induction field slopes.

With increasing yaw angle, the slopes of induction fields predicted by the engineering models get further away from the slope of the induction field predicted by CFD. This observation is also backed by increasing error values with an increase in yaw angles in Table 4.1. The model that does not show this behaviour of increasing error with increasing yaw angles is White and Blake's model. The cumulative error is not greatly influenced by the yaw angle as much as it does for the other models. This is because this model uses a different formula to calculate the Coleman's constant which decides the slope of the induction field. Therefore, it can be concluded that the wake angle may be calculated using White and Blake's method for more accurate predictions of induction fields.

An objective comparison of the accuracy of yaw models is provided in Table 4.1 by presenting the cumulative error in predicted values of induction. The cumulative error is calculated by adding up the error in induction values corresponding to each element. The formula presented in Equation 4.3. It should be noted that the error values take into account the errors due to lack of tip corrections too. By looking at the values of error also, White and Blake's model performs the best, showing a constant trend in the error values. Therefore, it can be concluded that the method used for the calculation of wake angle by White and Blake is the best of the lot. The only downside is that it does not consider the effects of tip vortices while predicting the induction field. Therefore, it can be concluded that White and Blake's model with appropriate corrections for the effects of tip vortices, is the best option of the models discussed in this thesis. Based on the suggestions provided above, Oye's model's method of calculating the wake angle is replaced with the method of calculation used by White and Blake. This was done because White and Blake's model was found to predict the wake angle much more accurately than the other models and Oye's model was the only model that could take tip effects into consideration. The results presented below correspond to the model given in Equation 4.4. The induction field predictions look much better after this modification is made. As it can be readily observed, the overall slope of the induction field is properly captured now. The tip effects, even though are not properly captured, are considered in this model, unlike the original White and Blake model.

$$a_{yaw} = a_{avg}(1 + \mathbf{F}\sqrt{2}sin(\chi)sin(\psi)) \tag{4.4}$$

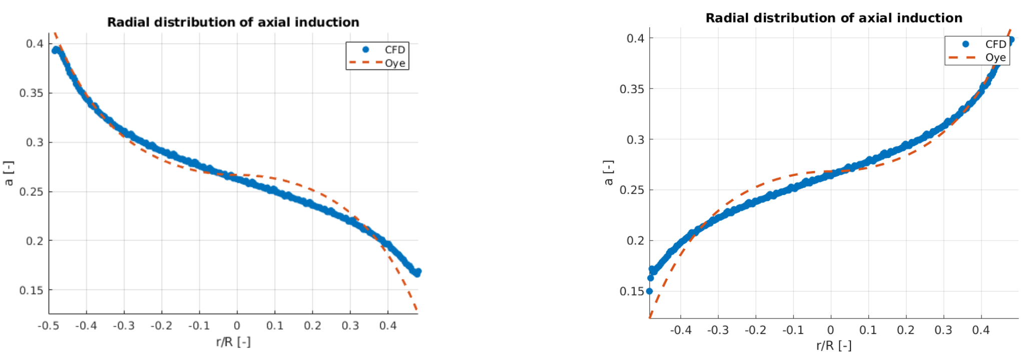

(a) $\theta_{yaw} = 10^o$ **(b)** $\theta_{yaw} = -10^o$

Figure 4.8: Comparison of induction field obtained from CFD results with the modified Oye's yaw correction model results for $\theta_{yaw} = 10^o$ and $\theta_{yaw} = -10^o$

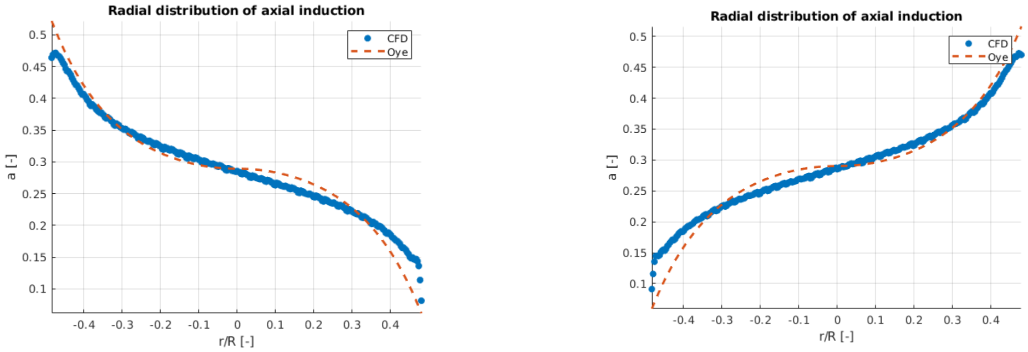

(a) $\theta_{yaw} = 15^o$ **(b)** $\theta_{yaw} = -15^o$

Figure 4.9: Comparison of induction field obtained from CFD results with the modified Oye's yaw correction model results for $\theta_{yaw} = 15^o$ and $\theta_{yaw} = -15^o$

4.2. Unsteady actuator disk results

In this section, the results of the unsteady actuator simulations are discussed. The section starts with presenting the aerodynamic effects that arise due to the rotor's pitching. This will be discussed using relevant contour plots of velocity, pressure, and vorticity. Following this discussion, a brief discussion on the differences between the aerodynamics of pitching and surging actuator disks is done by comparing the current results with results from [2]. In the subsequent section, the induction field corresponding to the pitching actuator disk is presented and is also compared with the surging CFD results and the dynamic inflow model result. The pitching induction results will be discussed by plotting the disk-averaged induction and induction at the center of the disk (at r/R = 0). In a later section, a deeper analysis of the effects of tilting is done by plotting the induction fields at the disk's periphery also (at $r/R = 0.9$ and $r/R = -0.9$).

Table 4.2 presents the unsteady actuator disk simulation matrix. It can be observed that the simulation matrix produced in Table 4.2 tries to replicate the test matrix used by Arianna [2] in their thesis publication on the study of the induction field of an actuator disk under surge motion. By replicating the cases analyzed by Arianna [2], it was attempted to recreate the same cases and provide a comparative study between surging and pitching actuator disks. The only parameter that is different from the cases simulated by Arianna is the amplitude of pitching. It could be noted that the amplitude of pitching is θ_p = 8.05^o. This amplitude was chosen to maintain the same magnitude of displacement handled in the analysis done on the surging actuator disk by Arianna. As mentioned earlier, the NREL 5MW reference wind turbine (only for the dimensions of the rotor diameter and hub height) is chosen for this purpose. Therefore, when an NREL 5MW wind turbine pitches at an amplitude of θ_p = 8.05^o, it also translates to a distance of $x/D = 0.1$ which is the amplitude of surging for the cases analyzed in [2]. Even though it was planned to perform a different set of simulations on the pitching actuator disk, it was later understood that a comparative analysis between these two (surge and pitch) platform motions adds more value to the research as it helps the community better compare and contrast the effects that these two similar platform motions have on the performance of the rotor. Also, this simulation matrix helps us understand and compare the accuracy of the surging rotor's dynamic inflow model [3] when applied to the pitching motion of the rotor and to the surging motion.

In Table 4.2, cases 1 to 6 represent the cases where the actuator disk is moving in a sinusoidal pitching motion while exerting a constant thrust on the flow. Cases 7 to 12 represent the cases where the actuator disk is physically fixed while the thrust exerted by the actuator disk varies in magnitude and direction with time mimicking the trend of thrust exerted by a pitching rotor. The cases further down, cases 13 through 24, represent a pitching actuator disk with dynamic thrust prescription. Cases 18 through 24 represent special and extreme cases to test the applicability of the dynamic inflow model [3] for pitching motion. Even though the chances of occurrence of such cases are close to zero or even zero in real life, they are included in this CFD analysis campaign to validate the dynamic inflow model

Table 4.2: Simulation matrix containing all the Actuator disk simulations done

Case #	Ct	delCt	A [deg]	f_p [Hz]	K [-]	V_max [-]
1	0.8	0	8.05	1.7506	0.999	0.1
2	0.8	0	8.05	8.7535	4.999	0.5
3	0.8	0	8.05	17.506	9.999	0.99
4	0.5	0	8.05	1.7506	0.999	0.1
5	0.5	0	8.05	8.7535	4.999	0.5
6	0.5	0	8.05	17.506	9.999	0.99
7	0.8	0.5	0	1.7506	0.999	0
8	0.8	0.5	0	8.7535	4.999	0
9	0.8	0.5	0	17.506	9.999	0
10	0.5	0.3	0	1.7506	0.999	0
11	0.5	0.3	0	8.7535	4.999	0
12	0.5	0.3	0	17.506	9.999	0
13	0.5	0.3	8.05	1.7506	0.999	0.1
14	0.5	0.3	8.05	8.7535	4.999	0.5
15	0.5	0.3	8.05	17.506	9.999	0.99
16	0.8	0.5	8.05	1.7506	0.999	0.1
17	0.8	0.5	8.05	8.7535	4.999	0.5
18	0.8	0.5	8.05	17.506	9.999	0.99
19	0.8	-0.5	8.05	1.7506	0.999	0.1
20	0.8	-0.5	8.05	8.7535	4.999	0.5
21	0.8	-0.5	8.05	17.506	9.999	0.99
22	0.5	1	8.05	1.7506	0.999	0.1
23	0.5	1	8.05	8.7535	4.999	0.5
24	0.5	1	8.05	17.506	9.999	0.99

for extreme and unphysical situations.

4.2.1. Results of cases with a pitching actuator disk with constant thrust

This section discusses the results of cases with a pitching actuator disk with constant prescribed thrust. As an attempt to do a comparative study between the aerodynamics of a surging actuator disk and a pitching actuator disk, the contour plots of velocity, pressure, and vorticity obtained from the pitching actuator CFD results are compared and contrasted with the contour plots obtained from a surging actuator CFD analyses done by Arianna[2]. Contour plots corresponding to different extremities of the pitching cycle are presented to provide a deeper understanding of the flow physics at different time steps.

Initial observations

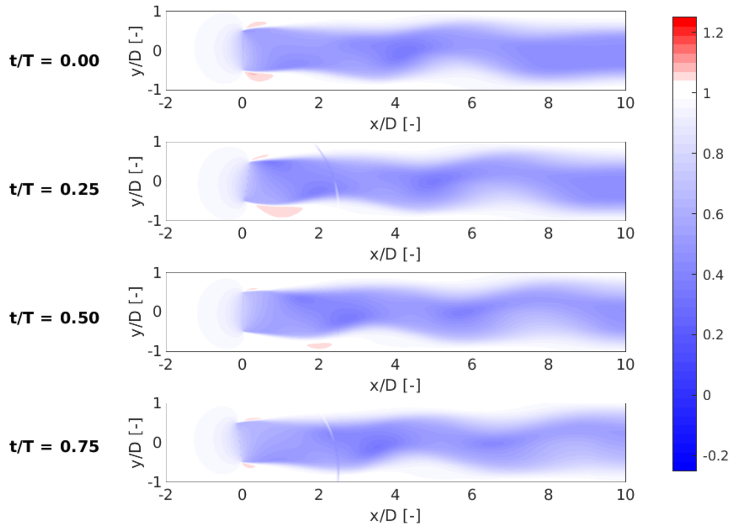

Figure 4.10: Contour of normalized X velocity (U_x/U_∞) for Case1 - $C_T = 0.8$; $\Delta C_T = 0$; $\theta_p = 8^o$; $\omega_{red} = 1$

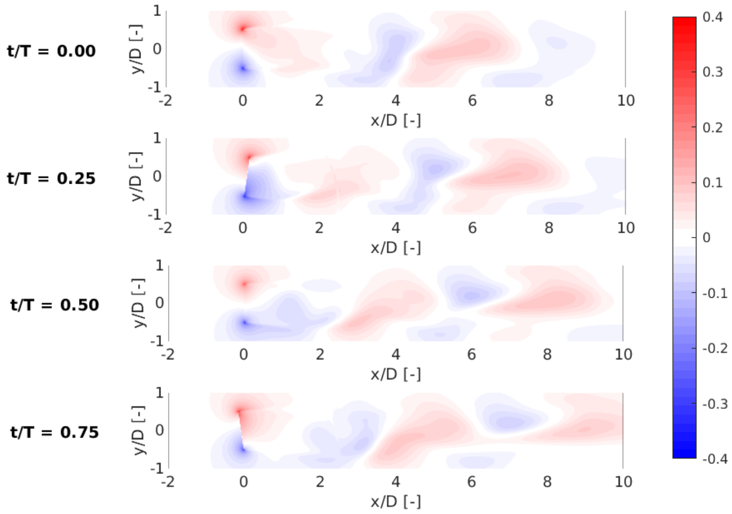

Figure 4.11: Contour of normalized Y velocity (U_y/U_∞) for Case1 - $C_T = 0.8$; $\Delta C_T = 0$; $\theta_p = 8^o$; $\omega_{red} = 1$

The most significant observation from the velocity contours in Figure 4.10 and Figure 4.11 is the slow-down of the flow field downstream of the rotor. A strange arc (around 2D downstream) in the wake is observed in the contours. This is purely an effect of deformed cells and therefore is not a physical phenomenon. Please refer to Appendix D in the appendix for better clarity on this. As with any actuator disk which imposes thrust against the free stream, the flow field slows down in the wake of the actuator disk and speeds up near the actuator disk's outer edges to conserve mass continuity. From both Figure 4.10 and Figure 4.11, it is prominent that there is a wake meandering because of the influence of the actuator disk's pitching motion. The flow speed-up near the actuator disk's edges can be better observed in Figure 4.11 where the curvature of flow around the actuator disk is clearly marked by red and blue coloured regions on the top and bottom of the actuator disk. As intuitive as it is, it can be observed that the flow outside of the stream tube tries to merge the wake due to the negative pressure difference between the freestream and the wake. One other important observation from Figure 4.11 is that the wake produced by the actuator disk is not symmetric. It could be observed that there is a significant downwash at $t/T = 0.25$ and a significant upwash at $t/T = 0.75$. In fact, on a deeper analysis, it was identified that the downwash is present during the whole time period from $t/T = 0$ to $t/T = 0.5$ and the upwash is present in the latter half of the cycle. That is, regardless of the position of the disk, whenever the actuator disk is pitching leeward ($\theta_p > 0$), there is a downwash of the flow just downstream of the actuator and when the disk is pitching forward ($\theta_p < 0$), the flow tends to move upwards. As the actuator pitches leeward, the flow is pushed down creating a region of downwash and as it pitches forward, it creates a region of low pressure on the upper half region which causes the flow to move up and create an upwash. In Figure 4.28 which shows the U_y contour of a still actuator disk, this effect is not observed. Therefore, it can be concluded that the downwash and upwash are purely due to the motion of the actuator disk because when the pitching motion is absent, the exact opposite trend is observed. Therefore, the pitching motion of the actuator can be concluded as the primary reason for the wake meandering observed here.

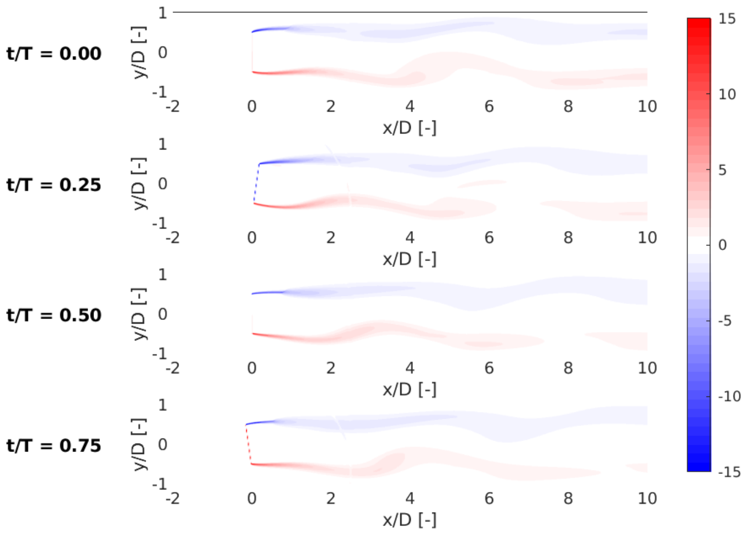

Figure 4.12: Contour of normalized Z vorticity ($\omega_z D/U_\infty$) for Case1 - $C_T = 0.8$; $\Delta C_T = 0$; $\theta_p = 8^o$; $\omega_{red} = 1$

From Figure 4.12, the tip vortices arising from the upper and lower edges of the actuator disk are apparent. It can be noted that the vortex shed from the top edge of the actuator disk has a negative magnitude (in -Z direction) and the vortex shed from the bottom edge has a positive magnitude. This observation is intuitive in the case of an actuator disk going by the definition of vorticity ($\omega = \nabla \times F$). In an actuator disk with constant loading and normal to the flow, there is no significant change in the force field along the actuator disk except for the tip of the actuator disk. Therefore, the formula for the strength of tip vortices becomes:

$$\omega = \nabla \times F_{ext} = -\frac{\partial f_x}{\partial y} \tag{4.5}$$

This leads to a negative vorticity on the top edge where $\partial y > 0$ and a positive vorticity on the bottom edge where $\partial y < 0$. It should be noted that ∂f_x is always positive at the disk's edges because the external force field (force exerted by the actuator in -X direction) is absent in the free stream and that makes the value of $\partial f_x > 0$. Since the change in force field at the actuator disk is less significant in the case of an actuator disk normal to the flow, at $t/T = 0$ and at $t/T = 0.5$, there is no vorticity field present on the actuator disk region during these two-time steps. At the extremities of the pitching cycle $t/T = 0.25$ and $t/T = 0.75$, where the force field on the actuator disk is non-uniform due to the yaw of the disk, a vorticity field can be observed. As expected, a negative vorticity field is observed at the actuator disk which signifies a decrease in the magnitude of f_x from the bottom edge to the top edge. Similarly, a positive vorticity field is observed at the actuator disk during the time step $t/T = 0.75$. This can be better understood by observing Figure 4.13 in which the induction field (depicted by black lines in front of the actuator disk region) in front of a tilted actuator disk is (roughly) presented. When the actuator is tilted backward, one can observe an induction field that decreases in magnitude from bottom to top as shown in Figure 4.13a and the exact opposite can be observed when the actuator is tilted forward as seen in Figure 4.13c. Contrary to both, when the actuator disk has no tilt, there is no significant difference in the induction field. Thus, the vortex shed from the actuator disk's region is also not as strong as the tip vortices.

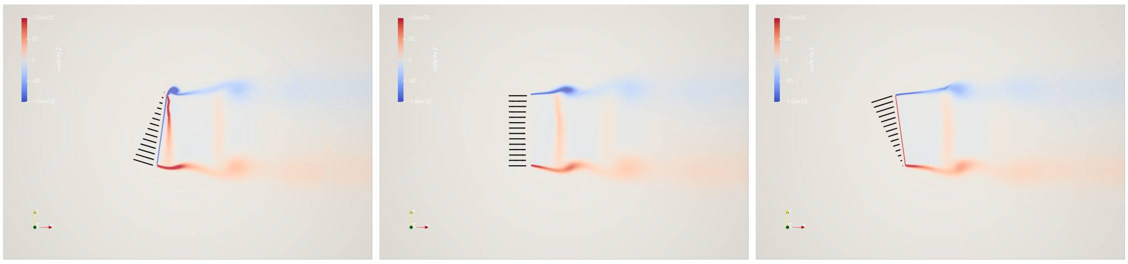

(a) $\theta_p = 8^o$ **(b)** $\theta_p = 0^o$ **(c)** $\theta_p = -8^o$

Figure 4.13: Illustration of the change in induction field and loading due to the actuator disk's tilt

Apart from the trend of vorticity field in and around the actuator disk region, the tip vortices show a distinctive behavior in the wake region too. Along with the wake, the vortices shed from the actuator's tips also undergo meandering. The observed wake meandering can also be influenced by the shedding of lumped tip vortices when the actuator disk is at the leeward extreme position (just after $t/T = 0.25$). It is visible that the location (x/D) of the top tip and the bottom tip of the actuator disks, when the vortex lumps are shed, are different due to the tilt of the actuator. This can also have an influence on the wake and lead to meandering. But the primary observation is that the vortices get lumped up as they pitch leeward and shed completely at the leeward extreme position.

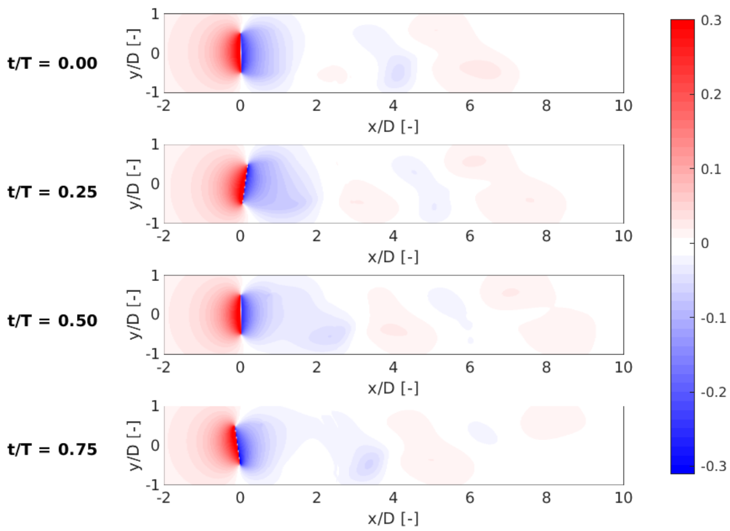

Figure 4.14: Contour of normalized pressure (C_P) for Case1 - $C_T = 0.8$; $\Delta C_T = 0$; $\theta_p = 8^o$; $\omega_{red} = 1$

From Figure 4.14, it can be observed that the force exerted by the actuator disk creates a region of high pressure in front of it and a region of low pressure downstream of it. It could also be observed that when the actuator disk is pitching leeward, it creates a region of low pressure (in the downstream region) that is biased toward the upper edge of the actuator disk and a region of high pressure (in the upstream region) which is biased towards the lower edge. The effect of this bias can be seen in the wake region also in the form of asymmetry in the wake.

This bias should be attributed to the upwash and downwash of the flow observed in the U_y contour. As the disk pitches leeward, the flow just downstream of the actuator also starts moving downwards, signified by the blue region at $t/T = 0.25$ in Figure 4.11. This creates a low-pressure region near the upper edge of the actuator disk. Similarly, when the actuator is pitching forward, flow tries coming back up signified by the red region at $t/T = 0.75$ in Figure 4.11.

High frequency case

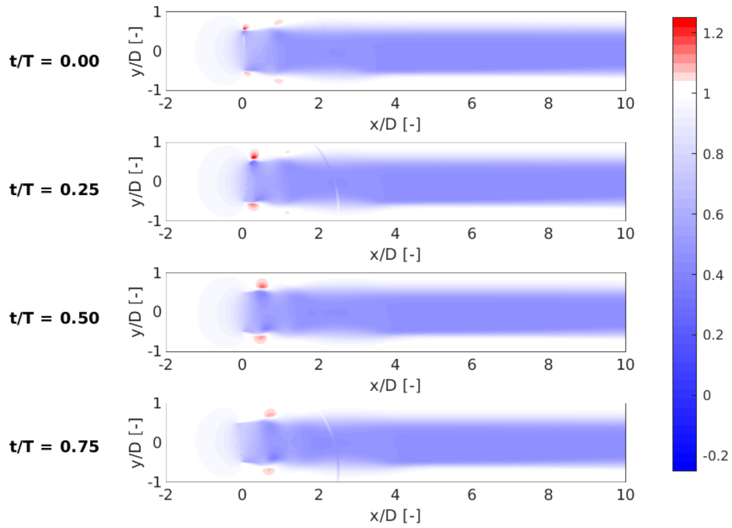

Figure 4.15: Contour of normalized X velocity (U_x/U_∞) for Case2 - $C_T = 0.8$; $\Delta C_T = 0$; $\theta_p = 8^o$; $\omega_{red} = 5$

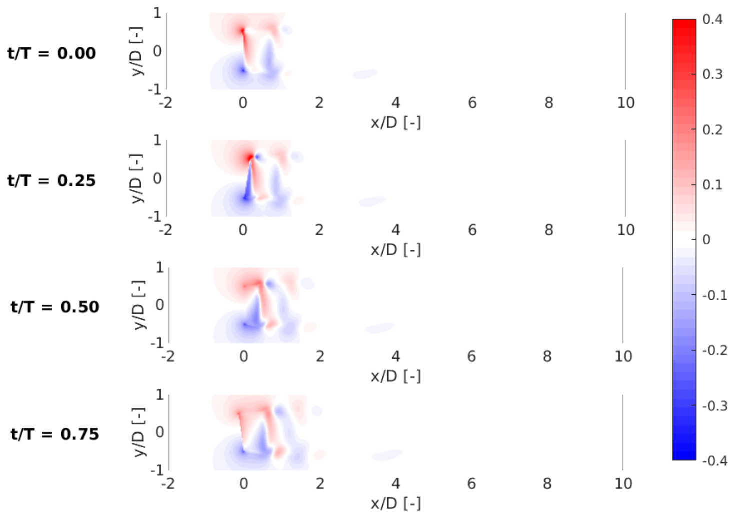

Figure 4.16: Contour of normalized Y velocity (U_y/U_∞) for Case2 - $C_T = 0.8$; $\Delta C_T = 0$; $\theta_p = 8^o$; $\omega_{red} = 5$

From the velocity contours presented by Figure 4.15 and Figure 4.16, the primary observations that can be made are the effects increase in the pitching frequency of the actuator. This is highlighted by smaller but stronger flow shear in Figure 4.16(compared to Figure 4.10 and Figure 4.11) near the edges of the actuator disk. As a result, the wake meanders at a higher frequency proportional to the pitching frequency of the actuator. The same observation of upwash and downwash downstream due to flow shear around the actuator disk is observed in this case too. However, these flow shears are concentrated closer to the actuator disk and have a steeper gradient. This is because the flow further downstream does not have enough time to adapt to the effects induced by the pitching disk. However, a significant difference in the wakes of case 1 with $\omega_{red} = 1$ and case 2 with $\omega_{red} = 5$ is also observed. The oscillations of flow in the Y direction get nullified much earlier than the case with low frequency. This signifies a higher level of turbulent mixing in the wake for higher frequencies of pitching.

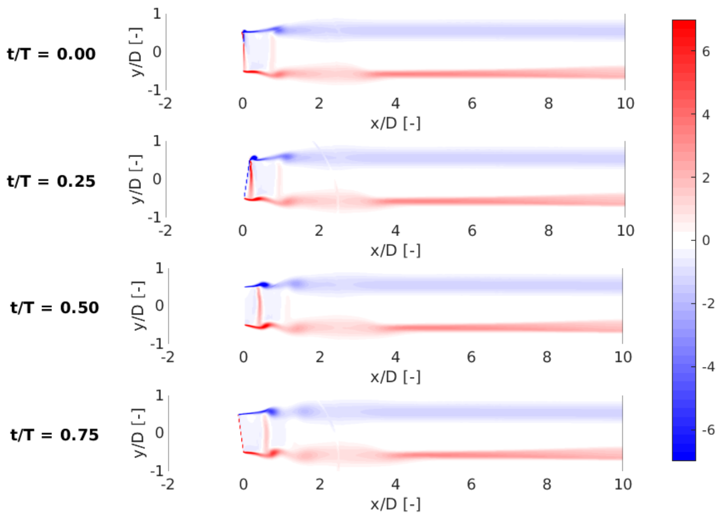

Figure 4.17: Contour of normalized vorticity ($\omega_z D/U_\infty$) for Case2 - $C_T = 0.8$; $\Delta C_T = 0$; $\theta_p = 8^o$; $\omega_{red} = 5$

The primary observations made from Figure 4.12 apply for Figure 4.17 also. However, as observed with the other contour plots corresponding to case 2, the same phenomena are observed but more prominently and with a higher intensity. The vortex lumping at the edges during leeward pitching and its shedding at the leeward extremity is clearly visible at higher frequencies of pitching.

An interesting observation from Figure 4.17 is the positive and negative vortex sheets shed from the actuator, parallel to the Y axis. However, these vortex sheets have a gradient to them. The strength of the positive vortex increases from bottom to top while the negative vortex is stronger at the bottom than at the top. It is important to note that these vortices are nearly as strong as the tip vortices. Since these vortices are more clearly observed at higher frequencies, the production of this vortex is mostly an effect of the actuator's pitching motion. It can also be seen that the vortex sheet convects downstream without changing its orientation signifying that this vortex is largely unaffected by the tip vortices and other flow instabilities. Upon observing other time steps, it was found that the source of this vortex is the change in the force field on the actuator disk during its pitching motion. The mechanism by which these two vortices arise and shed can be summarised in five steps:

- The positive vortex starts developing on the actuator from $t/T = 0.5$, when the actuator disk is tilted forward. This forward tilt results in a negative $\partial f_x/\partial y$ on the actuator disk and thus in a positive vorticity field to be developed on the same.
- As the actuator pitches forward, the vorticity gains in strength as the tilt angle gets higher and reaches a maximum at forward extreme position $t/T = 0.75$.
- When the actuator starts pitching leeward, the vorticity on the actuator slowly loses strength due to decreasing tilt of the rotor.

- This positive vorticity on the actuator disk sheds throughout the leeward pitching cycle from $t/T = 0.75$ to $t/T = 0$. At $t/T = 0$, a 'line' vortex that is normal to the free stream, that has a positive gradient ($\partial \omega_z / \partial y$) is fully shed.
- Even though this vorticity seems to be shed just from the top edge of the actuator, it is in fact shed from the whole actuator disk region. The vorticity just has a steep gradient such that the strength of the vorticity shed near the top edge is significantly higher than the vorticity shed from the bottom part of the actuator.

In a similar mechanism, the negative vortex also starts developing on the actuator disk from $t/T = 0$, when the actuator is pitching leeward from the mean position. This vorticity gains maximum strength at $t/T = 0.25$ when the actuator disk is fully tilted backward. As the actuator disk starts pitching forward, the negative vortex that was embedded with the actuator disk convects downstream and is visible in the wake. This negative vortex is shed throughout the forward pitching motion until the actuator disk reaches the forward extreme position. Thus, in the wake region, one can observe the positive vortex to be shed throughout the leeward pitching cycle and the negative vortex to be shed during the forward cycle.

Due to their close proximity to the actuator disk, these vortices can have a high influence on the induction field. However, the positive vortex is expected to have a slightly higher influence on the induction field than the negative vortex because of their difference in strengths. It should also be noted that the actuator disk tends to cross the positive vortex when it is pitching leeward. Therefore, the influence of this vortex is expected to be the highest when the actuator is pitching leeward. The influence of this vortex on the actuator's induction field is visualized in Section 4.2.4

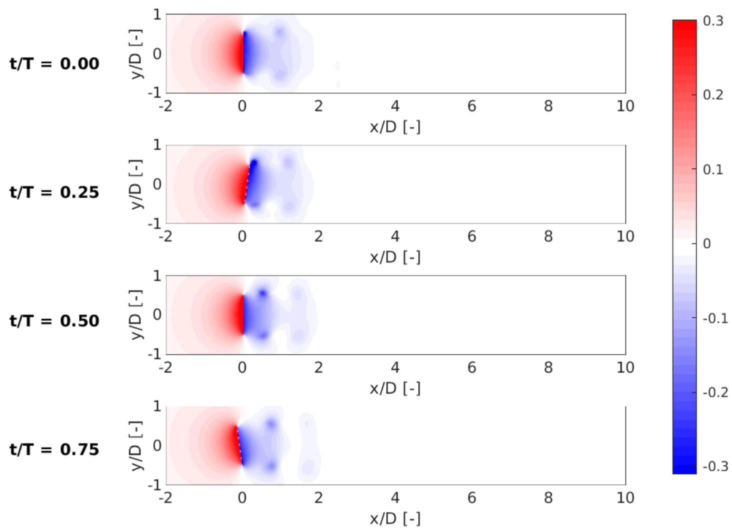

Figure 4.18: Contour of normalized pressure (C_P) for Case2 - $C_T = 0.8$; $\Delta C_T = 0$; $\theta_p = 8^o$; $\omega_{red} = 5$

The pressure contour of the case with $\omega_{red} = 5$, presented in Figure 4.18 is not very different from the behaviour observed in Figure 4.14. However, since the pitching velocity is high, the lumping of the low-pressure region on the top and bottom edges of the actuator disk is more visible due to the higher velocity of pitching. It can also be observed that these two regions of low pressure, even though they occur at different phases of the pitching cycle, traverse along the wake nearly at the same rate which is dictated by the wake.

Low thrust case

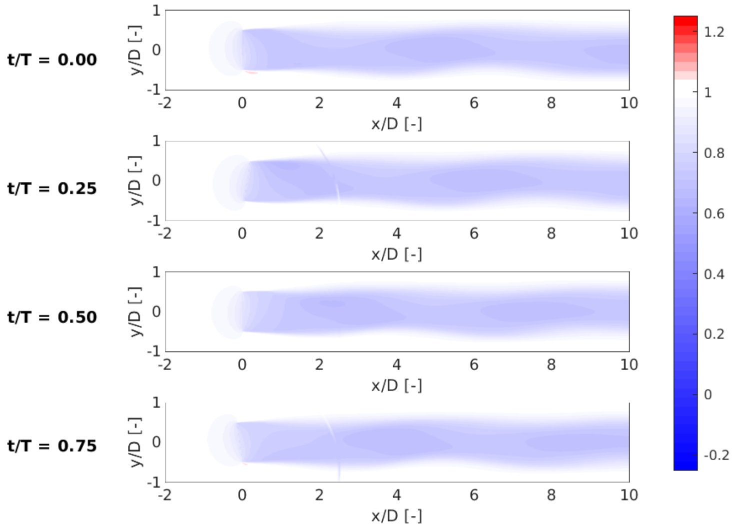

Figure 4.19: Contour of normalized X velocity (U_x/U_∞) for Case4 - $C_T = 0.5$; $\Delta C_T = 0$; $\theta_p = 8^o$; $\omega_{red} = 1$

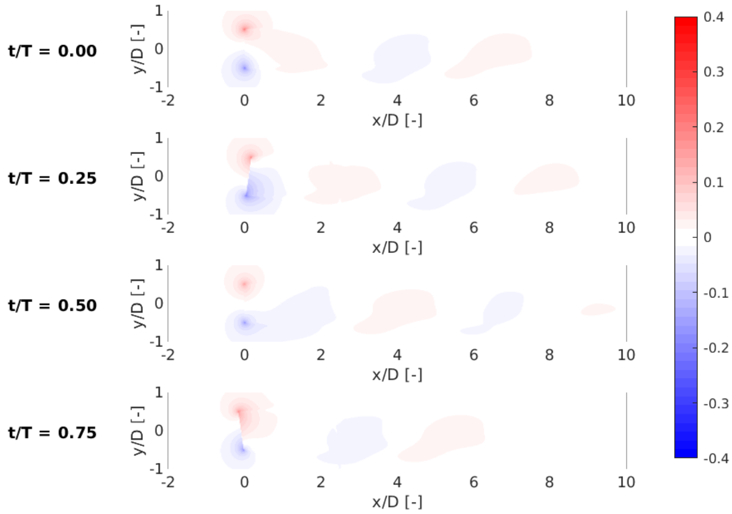

Figure 4.20: Contour of normalized Y velocity (U_y/U_∞) for Case4 - $C_T = 0.5$; $\Delta C_T = 0$; $\theta_p = 8^o$; $\omega_{red} = 1$

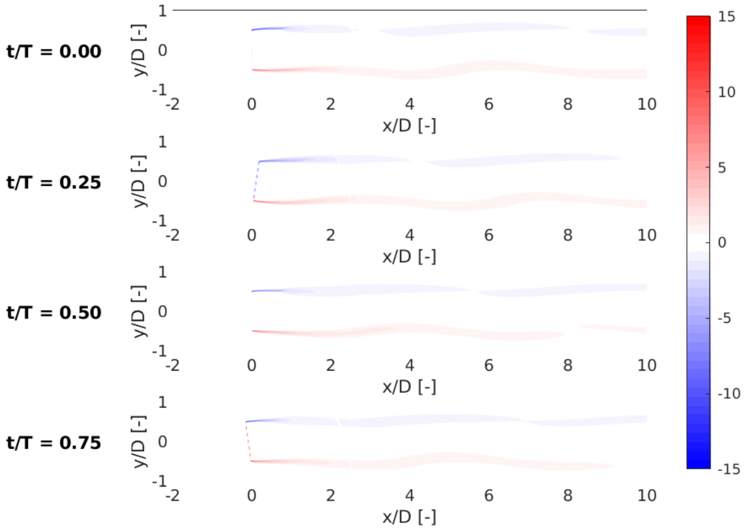

Figure 4.21: Contour of normalized Z vorticity ($\omega_z D/U_\infty$) for Case4 - $C_T = 0.5$; $\Delta C_T = 0$; $\theta_p = 8^o$; $\omega_{red} = 1$

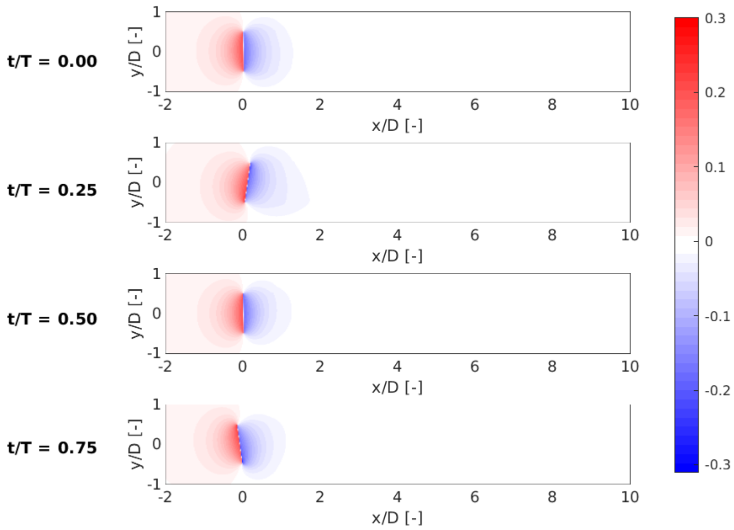

Figure 4.22: Contour of normalized pressure (C_P) for Case4 - $C_T = 0.5$; $\Delta C_T = 0$; $\theta_p = 8^o$; $\omega_{red} = 1$

Upon comparing the contour plots of normalized X and Y velocities, Z vorticity and pressure of case 4 (prescribed $C_T = 0.5$) with that of case 1's (prescribed $C_T = 0.8$) there is not a big difference observed in the trend of the flow physics. The noteworthy observation is that the wake meandering in the case with a lower thrust specification is slightly lesser than the meandering seen in the case with an actuator pitching at the same frequency but with a higher specified thrust. The same effect of lower thrust can be seen in pressure contour (Figure 4.22) too where the magnitude of the pressure difference between either side of the actuator disk is lesser than that observed with high thrust case (refer Figure 4.14).

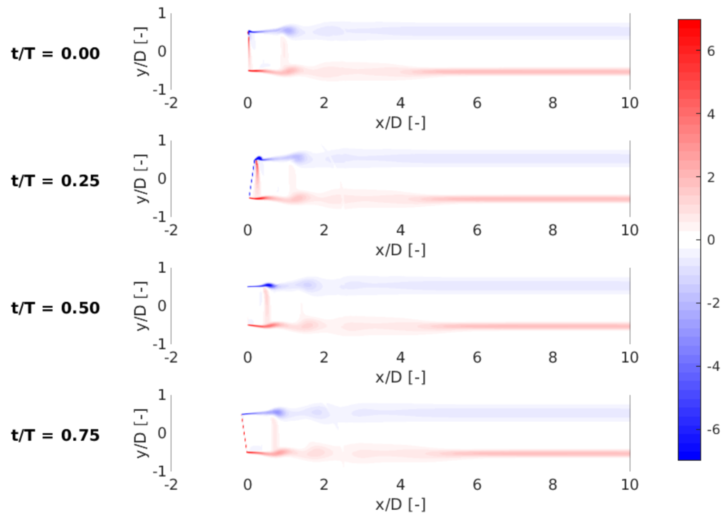

Figure 4.23: Contour of normalized Z vorticity ($\omega_z D/U_\infty$) for Case5 - $C_T = 0.5$; $\Delta C_T = 0$; $\theta_p = 8^o$; $\omega_{red} = 5$

An interesting observation that can be made from the normalized vorticity plot of low thrust pitching actuator disk is that the strength of the vortices shed parallel to the actuator disk (during the middle of the cycle) is of lower strength compared to the vorticity shed in the case of pitching actuator disk with higher specified thrust (case 2 - Figure 4.17). This observation reiterates that the strength of these vortices depends on the pitching velocity and the thrust exerted by the actuator, making it a non-linear effect.

Comparison of Pitching rotor aerodynamics with Surging cases

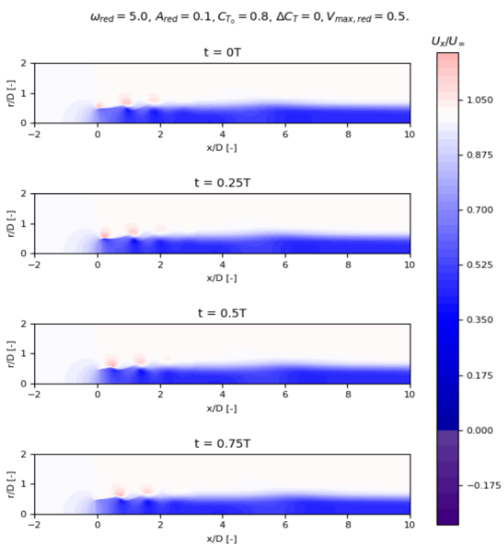

Figure 4.24: Comparison of U_x field of surging CFD case for $C_T = 0.8$; $\Delta C_T = 0$; $\theta_p = 8^o$; $\omega_{red} = 5$

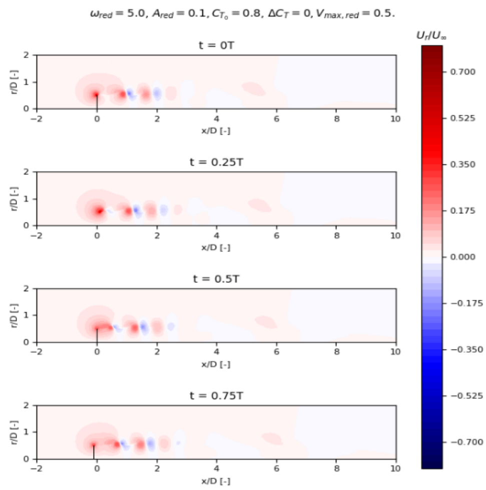

Figure 4.25: Contour of normalized R velocity (U_r/U_∞) for $C_T = 0.8$; $\Delta C_T = 0$; $\theta_p = 8^o$; $\omega_{red} = 5$ [2]

The pitching case corresponding to the contours presented in Figure 4.24 and Figure 4.25 is case 2 (refer to Figure 4.15 for normalised U_x contour and Figure 4.16 for normalised U_r contour). On observing the contour for U_x, it is clear that the wake of a surging actuator disk has no meandering as opposed to the pitching case. This is also confirmed by the contour plot of U_y also where the region close to $r = 0$ has a zero value for U_y. This observation, even though is intuitive, has been confirmed by the results obtained from the CFD analysis.

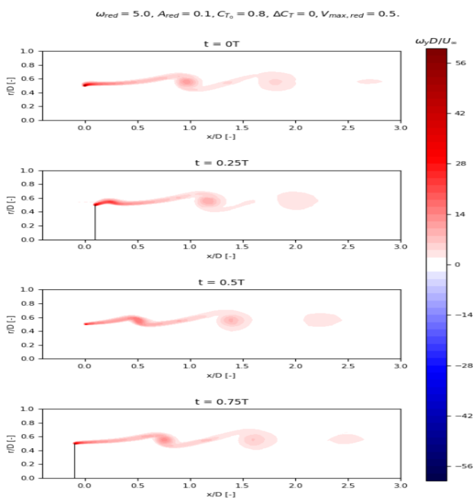

Figure 4.26: Contour of normalized Y vorticity ($\omega_z D/U_\infty$) for $C_T = 0.8$; $\Delta C_T = 0$; $\theta_p = 8^o$; $\omega_{red} = 5$ [2]

It should be noted that the reference results (from [2]) correspond to Y vorticity while the plots presented in this report correspond to Z vorticity. This can be disregarded as the reference results were taken from the XZ plane while the results presented in the current report correspond to the XY plane. Therefore, both these contours capture the tip vortices shed from the actuator disk and can be compared and contrasted.

The stark difference between Figure 4.26 and Figure 4.17 is the absence of the vortices that are shed along the actuator disk in the surging case. This is because there is no tilt to the actuator when it is surging, and this results in no significant gradient of force field on the actuator disc. Therefore, the only set of vortices that can have a significant effect on the induction field is the tip vortices.

4.2.2. Results of cases with still actuator disk with dynamic thrust

Before discussing the results, it must be noted that along with the magnitude of C_T imposed by the actuator, the direction also varies sinusoidally mimicking the change in direction of thrust when the actuator is subjected to pitching motion.

Initial observations

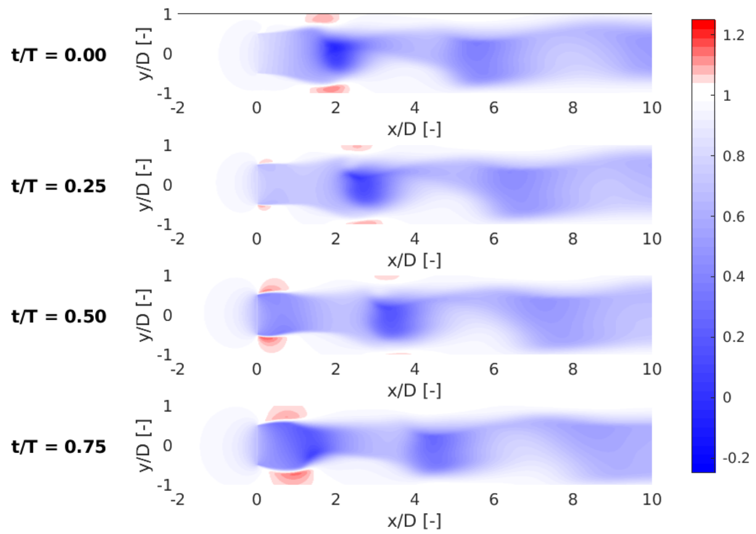

Figure 4.27: Contour of normalized X velocity (U_x/U_∞) for Case7 - $C_T = 0.8$; $\Delta C_T = 0.5$; $\theta_p = 0^o$; $\omega_{red} = 1$

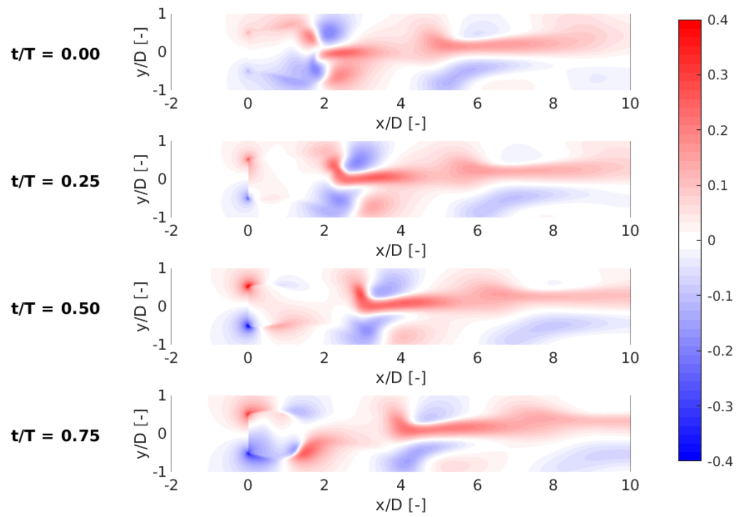

Figure 4.28: Contour of normalized Y velocity (U_y/U_∞) for Case7 - $C_T = 0.8$; $\Delta C_T = 0.5$; $\theta_p = 0^o$; $\omega_{red} = 1$

Figure 4.27 and Figure 4.28 present the normalized U_x and U_y contours of a still actuator disk with dynamic thrust prescription. In Figure 4.27, the meandering of wake can be clearly observed. However, the wake meandering seems to have a 180^o phase shift with the wake that was observed in Figure 4.10. This is because the prescribed thrust also changes direction in an effort to mimic a pitching actuator disk. It is a known fact that an actuator that imposes thrust with a positive Y component will introduce a positive Y component to the wake. The same effect is observed in Figure 4.28. At $t/T = 0.25$, the thrust imposed by actuator has a positive Y component (similar to an actuator that is tilted backward). Thus, a positive U_y is observed at $t/T = 0.25$ and a negative U_y is observed at $t/T = 0.75$. Therefore, it can be concluded that the meandering of the wake introduced by the pitching motion and thrust are in opposite phases.

The occurrence of a turbulent wake state (TWS) is also observed in the wake of the actuator disk, marked by areas of recirculation (negative U_x) at around 2D downstream at $t/T = 0$. It can be seen that the TWS is a result of a high thrust value ($C_T \geq 1$). Therefore, the researchers should take the occurrence of TWS into consideration while developing an engineering model for pitching FOWTs at high thrusts. The phase shift of wake meandering between the cases with still actuator and moving actuator (with constant thrust) is more clearly visible in Figure 4.28. In Figure 4.28, in contrast to Figure 4.11, the downwash and upwash occur at exactly opposite phases of the pitching cycle. In Figure 4.28, an upwash is observed at $t/T = 0.25$ while Figure 4.11 presented a downwash. The upwash observed in Figure 4.28 makes clear sense because the direction of the specified thrust is inclined positively (such that the actuator disk is tilted and facing upwards). This exerts a thrust with an upward component on the flow and thus makes the wake tilt upwards which results in an upwash. For similar reasons, a significant downwash is observed at $t/T = 0.75$.

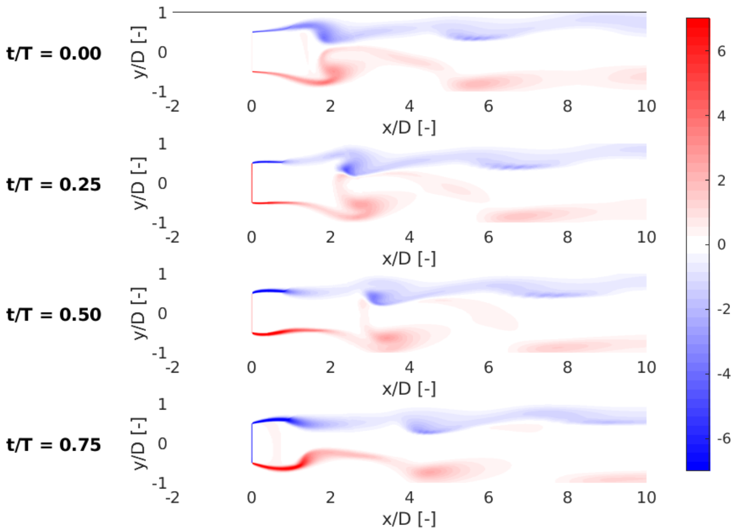

Figure 4.29: Contour of normalized vorticity ($\omega_z D/U_\infty$) for Case7 - $C_T = 0.8$; $\Delta C_T = 0.5$; $\theta_p = 0^o$; $\omega_{red} = 1$

Figure 4.29 presents the vorticity field that arises due to a still actuator disk with oscillating prescribed thrust. It can be observed that the tip vortices shed from the actuator disk have a symmetric behaviour in the wake. The slight asymmetry between the top and bottom tip vortices can be attributed to numerical diffusion due to cells of bad quality and also not oriented with the flow. Thus, the vortex at the top edge diffuses faster than the vortex shed from the bottom edge. In an ideal mesh, this effect is not expected and the vortices from the top and bottom edges should be symmetric. This symmetric behaviour contrasts with the observation made in Figure 4.12 in which the vortices get asymmetric as they convect downstream. Since the vortices are shed at the exact location in the case of a still actuator disk, they convect symmetrically downstream.

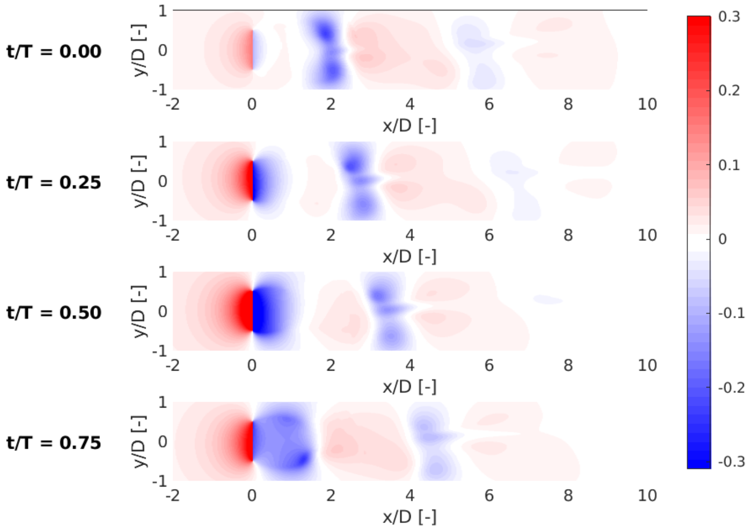

Figure 4.30: Contour of normalized pressure (C_P) for Case7 - $C_T = 0.8$; $\Delta C_T = 0.5$; $\theta_p = 0^o$; $\omega_{red} = 1$

Figure 4.30 presents the pressure field corresponding to case 7. A clear observation from the plot is the alternating high-pressure and low-pressure regions in the wake. It is clear that these alternating regions of low pressure and high pressure are clearly a result of the change in magnitude of specified thrust. At $t/T = 0$, where the region just downstream of the actuator reaches the highest pressure, and at $t/T = 0.5$ that region reaches the lowest pressure. These two time steps correspond to the lowest and highest thrusts exerted by the actuator disk. Thus, they result in alternating pressure regions in the wake.

Even though such behaviour was observed in Figure 4.14, it was much less pronounced due to the higher levels of turbulent mixing in the wake. Since the actuator disk is maintained still in the case of Figure 4.30, turbulent mixing observed is much lesser than in cases 1 and 2 where the actuator disk is physically pitching. Therefore, it can be concluded that the turbulent levels in the wake of a pitching rotor can be attributed more to the platform motions than the change in thrust exerted by the rotor on the flow.

High frequency case

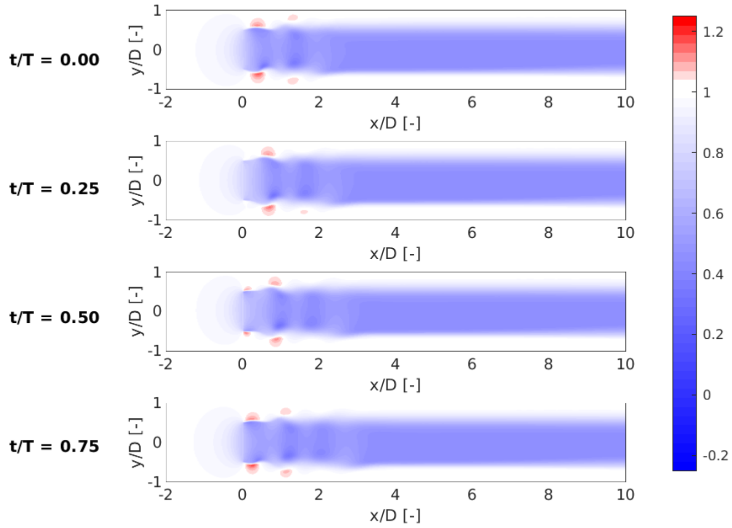

Figure 4.31: Contour of normalized X velocity (U_x/U_∞) for Case8 - $C_T = 0.8$; $\Delta C_T = 0.5$; $\theta_p = 0^o$; $\omega_{red} = 5$

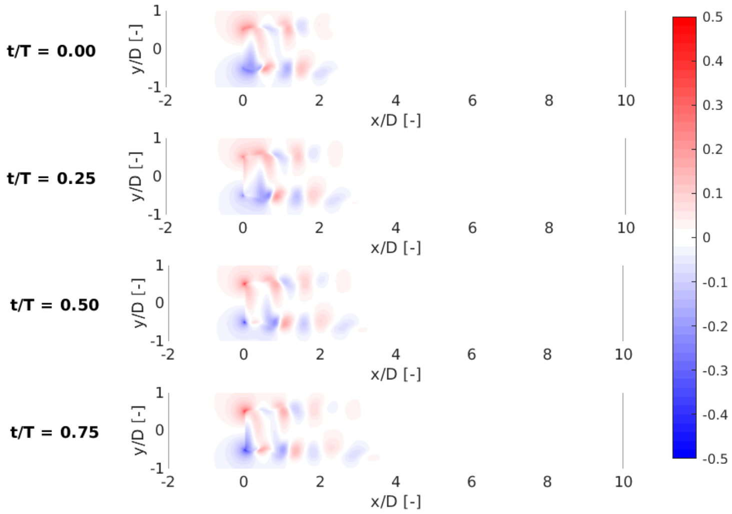

Figure 4.32: Contour of normalized Y velocity (U_y/U_∞) for Case8 - $C_T = 0.8$; $\Delta C_T = 0.5$; $\theta_p = 0^o$; $\omega_{red} = 5$

The X velocity contour of case 8, presented in Figure 4.31, is similar to that of case 7 with regard to the trend. A very similar trend is observed with respect to the Y velocity contour, represented by Figure 4.32 too. The flow physics is very similar to that of case 7's but occurs at a higher frequency. In Figure 4.32, the meandering of the wake is more clearly observed marked by alternating regions with positive and negative Y velocities.

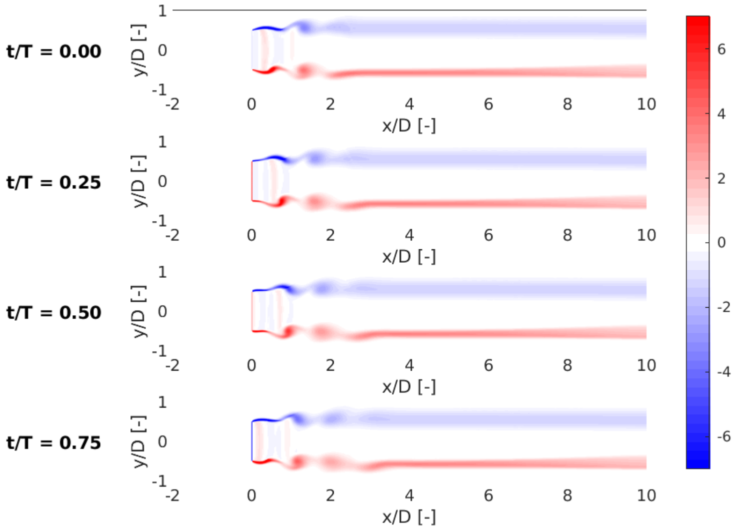

Figure 4.33: Contour of normalized vorticity ($\omega_y D/U_\infty$) for Case8 - $C_T = 0.8$; $\Delta C_T = 0.5$; $\theta_p = 0^o$; $\omega_{red} = 5$

Figure 4.33 presents the normalized vorticity contour corresponding to case 8. A vortex, normal to the flow, similar to the one observed in case 2 (Figure 4.17) is also observed in this case. Even though the actuator disk is not physically tilted to introduce a force gradient on the actuator disk, the directional nature of the thrust specification induces a gradient in the induction response of the actuator(just as depicted in Figure 4.13). This leads to a gradient in the force field on the actuator and thus leads to vortices getting shed normal to the flow. Upon close observation, it can also be noted that the vorticity at the actuator disk region assumes a positive magnitude at $t/T = 0.25$. This behaviour is exactly opposite to the negative vorticity produced at $t/T = 0.25$ in Figure 4.12 (pitching actuator disk with constant thrust). Thus the vortices that are shed due to the gradient in the force field also have a 180^o phase shift with the cases that simulate pitching actuator with constant thrust.

However, the strength of this vortex is lesser than the vortex shed in the case of a physically pitching actuator. It is also noteworthy that there is no lumping of vortices due to pitching motion as observed in case 2. In the case of a still actuator disc, these normal vortices do not have as big an influence on the induction field of the actuator disk because of two reasons. The first is that it is weaker than the vortices observed in the pitching case. The second and more important reason is that, since the actuator disk is still, it does not come under the direct influence of this vortex as opposed to the case of a moving actuator where the actuator falls into this vortex while it pitches leeward.

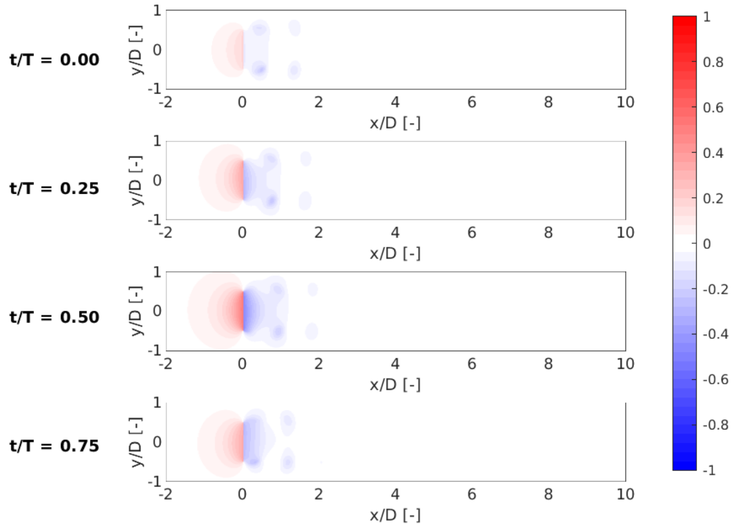

Figure 4.34: Contour of normalized pressure (C_P) for Case8 - $C_T = 0.8$; $\Delta C_T = 0.5$; $\theta_p = 0^o$; $\omega_{red} = 5$

With regards to the pressure plot, there is not much of a difference with respect to the case with a lower frequency of thrust modulation (case 7). The regions of high pressure and low pressure are just much closer together because of the higher frequency of thrust modulation.

Low thrust case

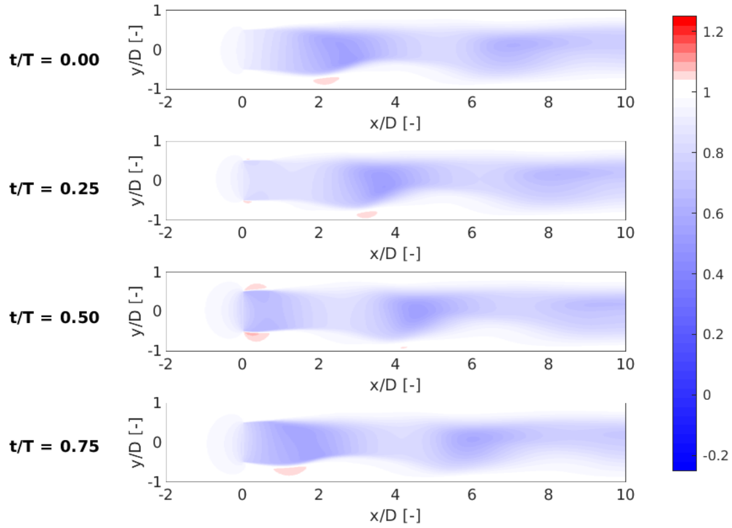

Figure 4.35: Contour of normalized X velocity (U_x/U_∞) for Case10 - $C_T = 0.5$; $\Delta C_T = 0.3$; $\theta_p = 0^o$; $\omega_{red} = 5$

Comparing the U_x contour of case 10 with the U_x contour observed with case 7 (refer to Figure 4.27) is that TWS is not observed in this case. This again hints that the occurrence of TWS is determined by the magnitude of thrust imposed by the rotor on the flow. As expected, the extent to which the wake meanders is also lesser than that observed in Figure 4.27. Similarly, the strength of tip vortices is also lesser compared to the vortices observed in the high-thrust case (Figure 4.29). Due to a lesser turbulent wake, these tip vortices tend to travel longer without dissipating much leading to a more stable wake which takes longer to recover.

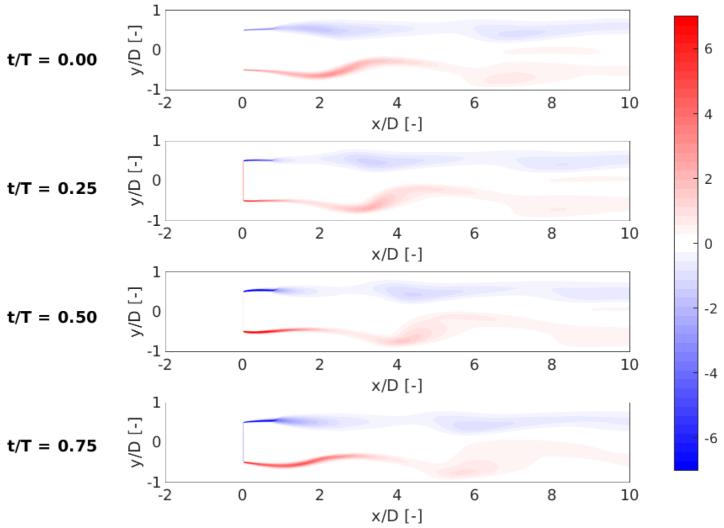

Figure 4.36: Contour of normalized Z vorticity ($\omega_z D/U_\infty$) for Case10 - $C_T = 0.5$; $\Delta C_T = 0.3$; $\theta_p = 0^o$; $\omega_{red} = 5$

Comparison of Pitching rotor aerodynamics with Surging cases

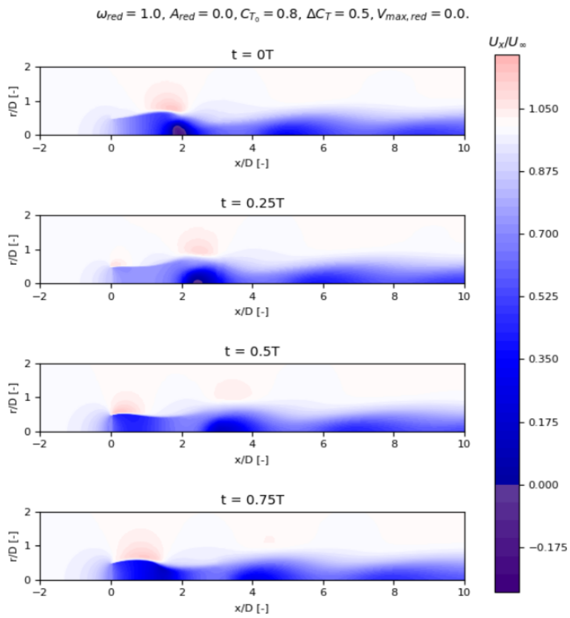

Figure 4.37: Contour of normalized X velocity (U_x/U_∞) for $C_T = 0.8$; $\Delta C_T = 0.5$; $\theta_p = 0^o$; $\omega_{red} = 1$

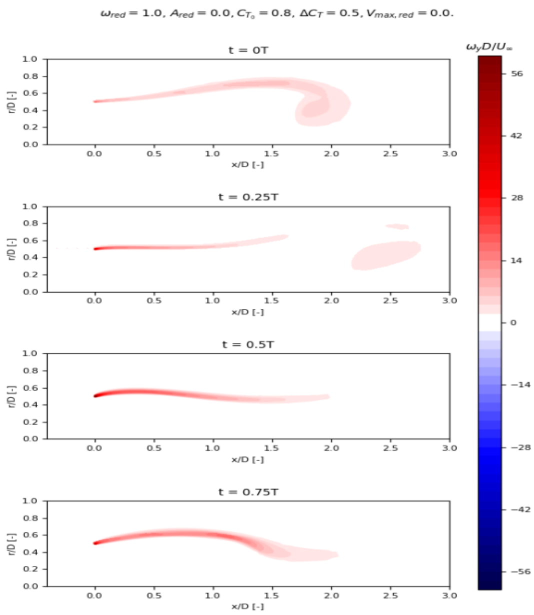

Figure 4.38: Contour of normalized Y vorticity ($\omega_y D/U_\infty$) for - $C_T = 0.8$; $\Delta C_T = 0.5$; $\theta_p = 0^o$; $\omega_{red} = 1$

Figure 4.37 and Figure 4.38 present normalised U_x and ω_y contours corresponding to case 7 in Table 4.2. Comparing Figure 4.27 with the U_x contour corresponding to the pitching case, TWS occurs in both these cases at around 2D downstream. With regards to the vorticity plot, the same trend as observed in Section 4.2.1 is observed. Since the loading on the actuator disk is more uniform when compared to an actuator disk with tilt, there is no vorticity observed on the actuator at the extreme positions. This reiterates the fact that the only vortices to be considered for devising the dynamic inflow model for surging applications are the tip vortices. But to devise a dynamic inflow model for pitching actuators, the vortices shed parallel to the actuator disk also needs to be considered.

4.2.3. Results of cases with a pitching actuator disk with dynamic thrust

Initial observations

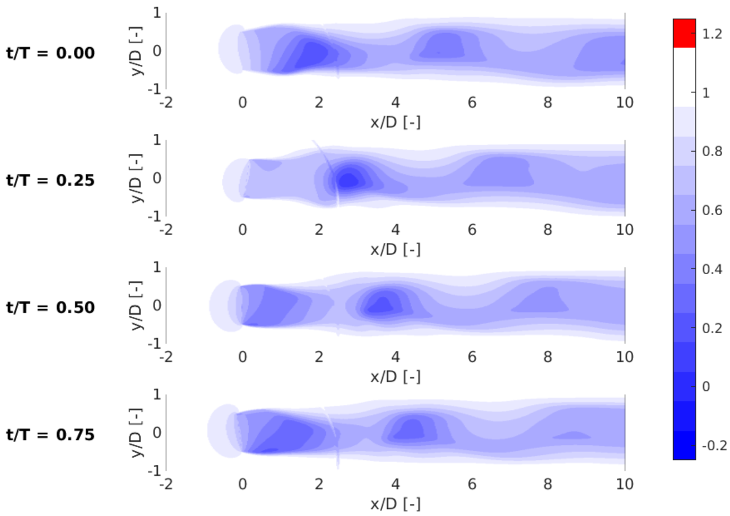

Figure 4.39: Contour of normalized X velocity (U_x/U_∞) for Case 16 - $C_T = 0.8$; $\Delta C_T = 0.5$; $\theta_p = 8^o$; $\omega_{red} = 1$

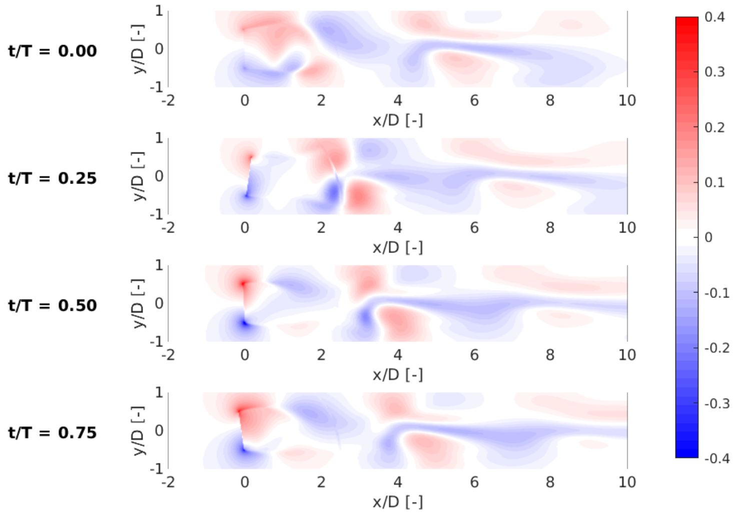

Figure 4.40: Contour of normalized Y velocity (U_y/U_∞) for Case 16 - $C_T = 0.8$; $\Delta C_T = 0.5$; $\theta_p = 8^o$; $\omega_{red} = 1$

The starkest observation made from the normalized U_x contour, presented in Figure 4.39, is the presence of recirculation regions in the wake. This results in an occurrence of the turbulent wake state (TWS). This is attributed to the high values of thrust during the cycle. From the contour plot, it is visible that the forward pitching of the actuator disk is when the flow recirculation arises. It is noteworthy that TWS did not occur in the previous two sets of cases. The red regions just outside of the wake signify a higher rate of shearing of the flow around the actuator disk when it is pitching with a dynamic thrust. The contour of U_y also shows a more turbulent wake region with stronger recirculation, which again signifies the occurrence of TWS.

It can also be observed that the normalized U_y contour of case 16 looks more similar to that of case 1 than the U_y contour of case 7 where only the thrust prescription changes. This implies that the flow physics of the wake is influenced more by the pitching motion of the actuator than the change in prescribed thrust. From the results observed from Figure 4.11, Figure 4.28, and Figure 4.40, it can be concluded that the influence of pitching motion has a higher influence on determining the wake dynamics than the change in rotor's thrust.

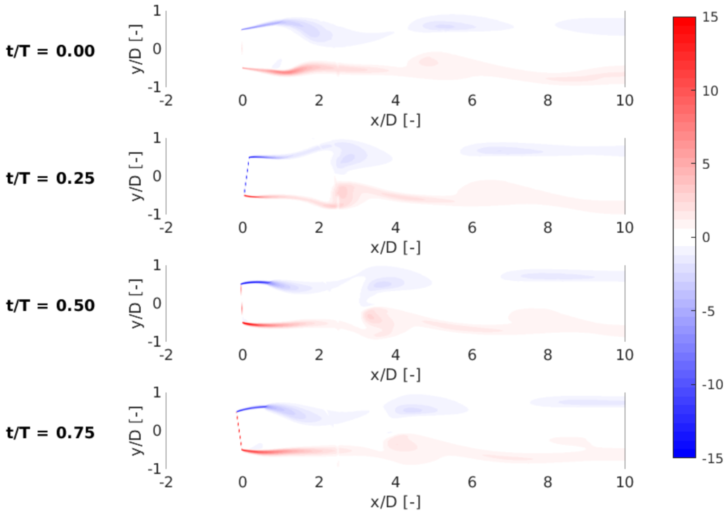

Figure 4.41: Contour of normalized Z vorticity ($\omega_z D/U_\infty$) for Case 16 - $C_T = 0.8$; $\Delta C_T = 0.5$; $\theta_p = 8o$; $\omega_{red} = 1$

The contour of the normalized vorticity field, presented by Figure 4.41, displays both behaviours of the vorticity field produced by the moving actuator with constant thrust (in Figure 4.12 - case 1) and the still actuator disk with dynamic thrust (in Figure 4.29 - case 7). The vortices shed from the tips tend to recirculate downstream at the regions where TWS occurs. However, the strength of these tip vortices does not seem to significantly vary from the previous cases.

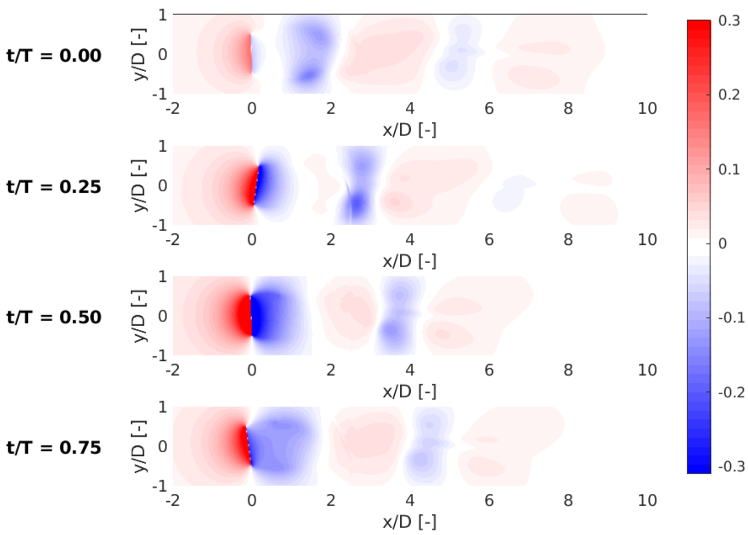

Figure 4.42: Contour of normalized pressure (C_P) for Case 16 - $C_T = 0.8$; $\Delta C_T = 0.5$; $\theta_p = 8^o$; $\omega_{red} = 1$

As with the vorticity contours, pressure contour also shows the compounding effect of imposing a dynamic motion and dynamic thrust to the actuator. The pressure contour presented in Figure 4.42, like Figure 4.14 - case 1, shows the same bias of negative pressure towards the top edge and bottom edge of the actuator disk at $t/T = 0.25$ and at $t/T = 0.75$ respectively. Figure 4.42 also shows the highest difference (between upstream and downstream of the rotor) in pressure fields at $t/T = 0.5$ and the lowest change in pressure field during $t/T = 0$ as observed in Figure 4.30.

High frequency case

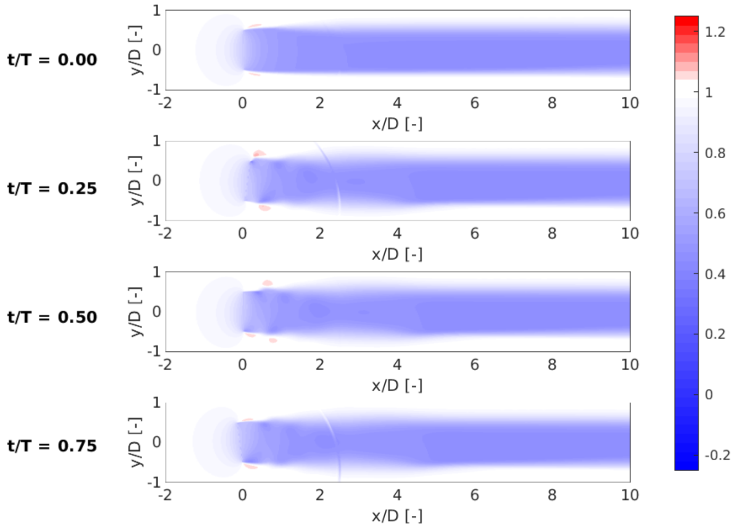

Figure 4.43: Contour of normalized X velocity (U_x/U_∞) for Case 17 - $C_T = 0.8$; $\Delta C_T = 0.5$; $\theta_p = 8^o$; $\omega_{red} = 5$

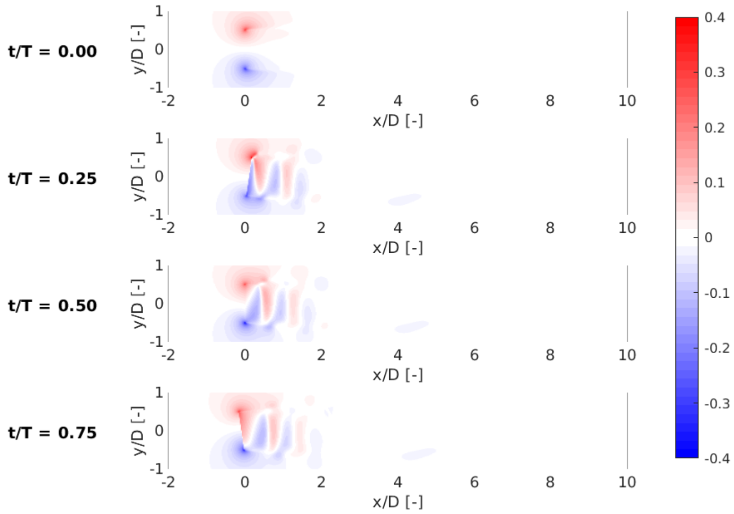

Figure 4.44: Contour of normalized Y velocity (U_y/U_∞) for Case 17 - $C_T = 0.8$; $\Delta C_T = 0.5$; $\theta_p = 8^o$; $\omega_{red} = 5$

From the contour of U_x presented in Figure 4.43, it is clear that the TWS state does not occur when the actuator pitches at high frequencies. This is because the flow does not have enough time to get influenced by the induction field of the rotor. Therefore, it can be concluded that TWS state is a threat only when the actuator pitches at low frequencies with high thrusts. The flow gets influenced by the dynamics of pitching motion more than the induction field at higher frequencies. This is confirmed by Figure 4.44 also where the oscillatory behaviour of flow in the wake dies out rather quicker than it did in the case with lower frequency.

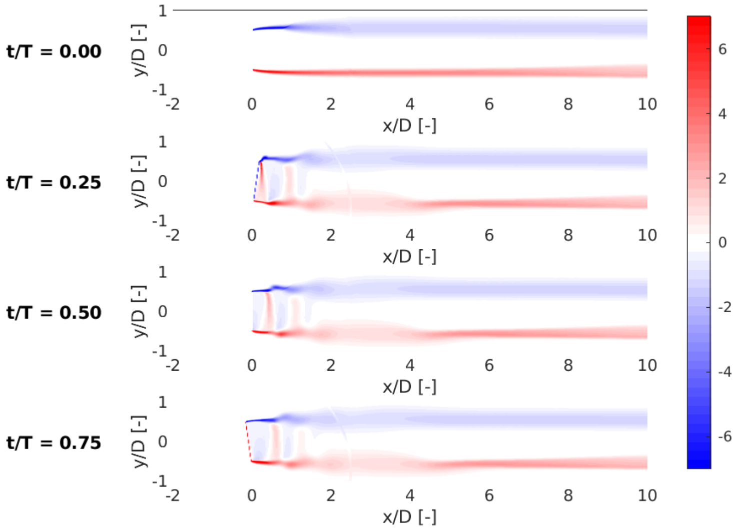

Figure 4.45: Contour of normalized Z vorticity ($\omega_z D/U_\infty$) for Case 17 - $C_T = 0.8$; $\Delta C_T = 0.5$; $\theta_p = 8^o$; $\omega_{red} = 5$

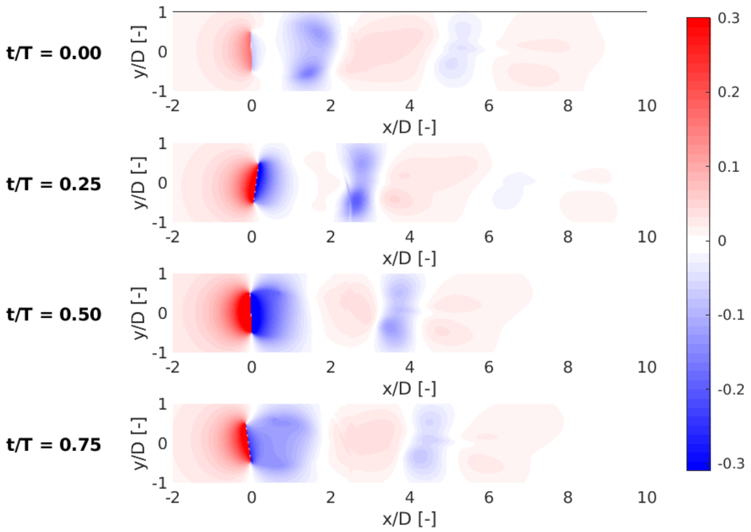

Figure 4.46: Contour of normalized pressure (C_P) for Case 17 - $C_T = 0.8$; $\Delta C_T = 0.5$; $\theta_p = 8^o$; $\omega_{red} = 5$

In Figure 4.45, the negative vortex (parallel to the actuator) shed from the bottom seems to have a slightly higher strength than it did in case 2 (refer to Figure 4.17). However, it can be clearly seen that the strength of this negative vorticity is comparatively higher than the negative vorticity observed in case 2 (notice the shorter range of colour map in Figure 4.17). This hints that the strength of the vortices that are shed parallel to the actuator disk is dependent on both the pitching velocity and the thrust output by the actuator disk. This also makes the strength of this tip vortex, which has a significant influence on the induction field, a non-linear effect of the pitching motion.

The pressure contour of case 17, presented by Figure 4.45, exhibits the same difference that other cases exhibited by other case sets. An increase in pitching frequency led to a faster decay of flow instabilities in the wake. Even though the magnitude of pressure difference between either sides of the actuator disks does not seem much different from the case with lower frequency, the size of the region of low pressure (downstream) is smaller than the case with lower frequency. This marks higher flow recovery in the case with higher frequency of pitching.

Low thrust case

There was not much of a difference observed in the low thrust low-frequency case (case 13). Therefore, only the case with low thrust and high frequency (case 14) is discussed in this section.

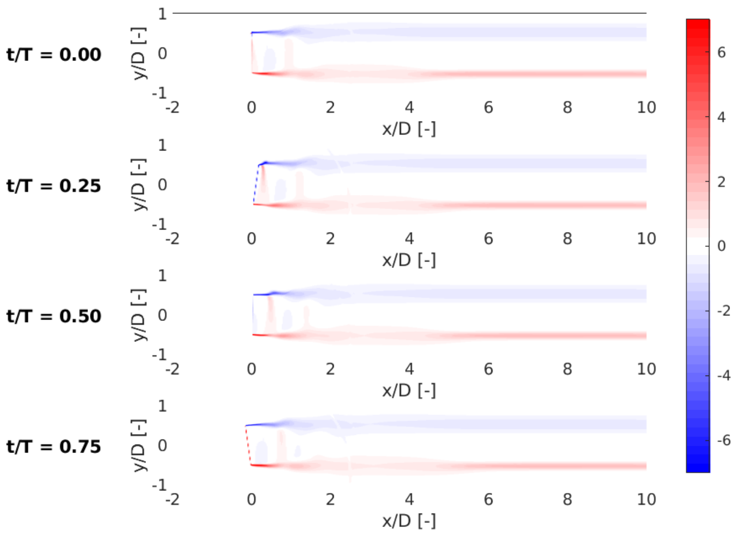

Figure 4.47: Contour of normalized Z vorticity ($\omega_z D/U_\infty$) for Case 14 - $C_T = 0.5$; $\Delta C_T = 0.3$; $\theta_p = 8^o$; $\omega_{red} = 5$

From Figure 4.47, it can be observed that the vortices that are shed parallel to the actuator disk is present in this case also. As observed in the previous cases such as case 17, case 2, and case 5, the strength of the positive vortex is higher than the negative vortex that is shed parallel to the actuator disk. Thus, their effect can still be expected in the induction field, but not to an extent as observed in cases 2 and 5.

Extreme load cases

In this section, contour plots corresponding to cases 19 to 24 are discussed. Cases 19 to 21 simulate a pitching actuator disk with $\Delta C_T = -0.5$. While cases 22 to 24 simulate a rotor with a magnitude of thrust variation higher than the baseline thrust.

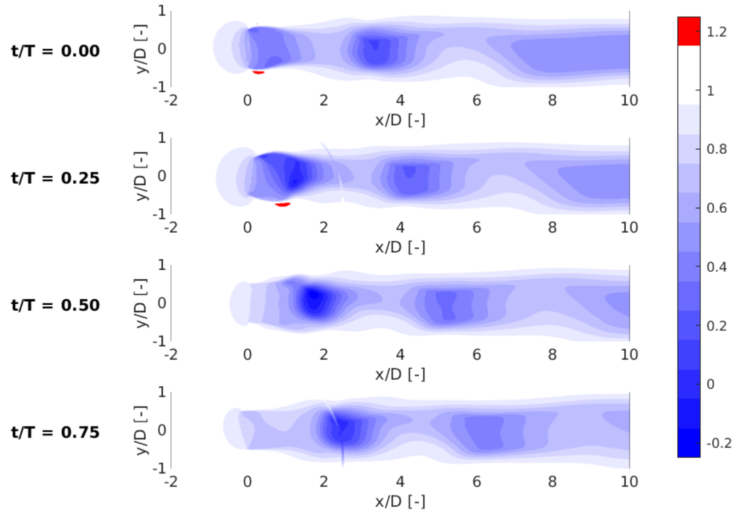

Figure 4.48: Contour of normalized X velocity (U_x/U_∞) for Case19 - $C_T = 0.8$; $\Delta C_T = -0.5$; $\theta_p = 8^o$; $\omega_{red} = 1$

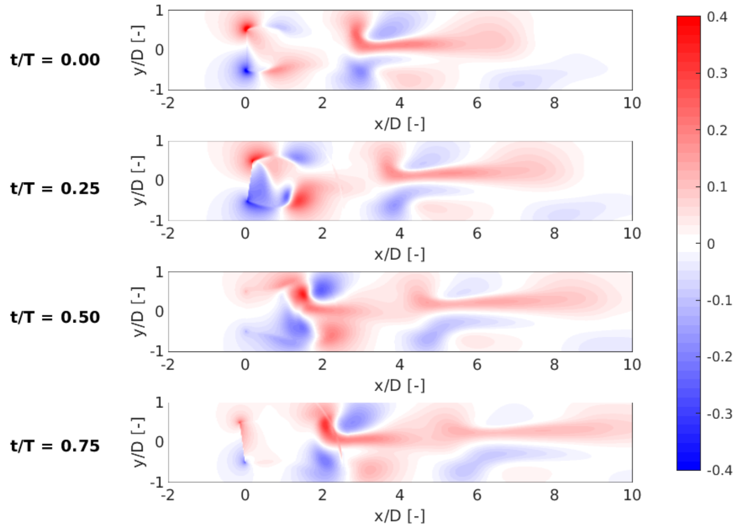

Figure 4.49: Contour of normalized Y vorticity (U_y/U_∞) for Case19 - $C_T = 0.8$; $\Delta C_T = -0.5$; $\theta_p = 8^o$; $\omega_{red} = 1$

The primary difference observed in the U_x contour of case 19 (Figure 4.48) when compared to that of case 16's (Figure 4.39) is that the location of occurrence of turbulent wake states is exactly at 180^o phase difference. This again confirms the fact that the TWS is primarily an effect of the magnitude of change in thrust. Case 19's contour of U_y shows the phase difference in wake dynamics more clearly by its alternating regions with positive and negative U_y values.

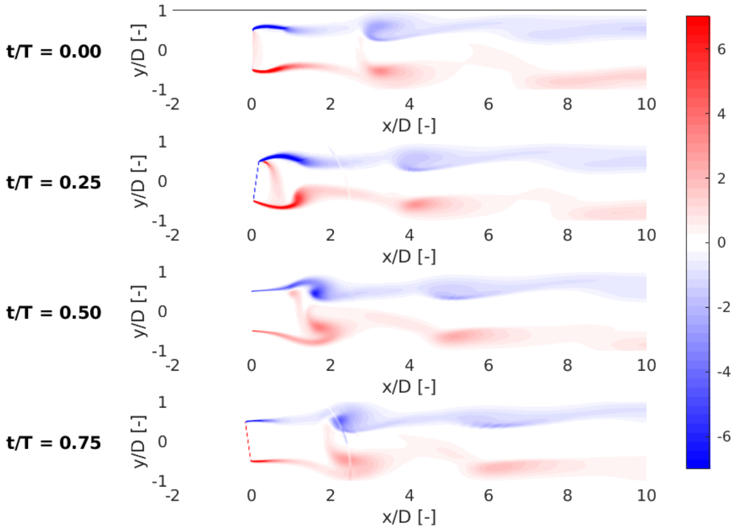

Figure 4.50: Contour of normalized Z vorticity ($\omega_z D/U_\infty$) for Case19 - $C_T = 0.8$; $\Delta C_T = -0.5$; $\theta_p = 8^o$; $\omega_{red} = 1$

In Figure 4.50, it is visible the line vortices that are shed parallel to the actuator disk are stronger in the case with negative dynamic thrust. Despite the 180^o difference in phase of C_T, these vortices are shed at the same phase of the pitching cycle as they did in the case with positive C_T. However, the vortices seem to convect faster compared to the case with positive C_T. Therefore, the influence of these vortices is not expected to be as high as they were with case 16.

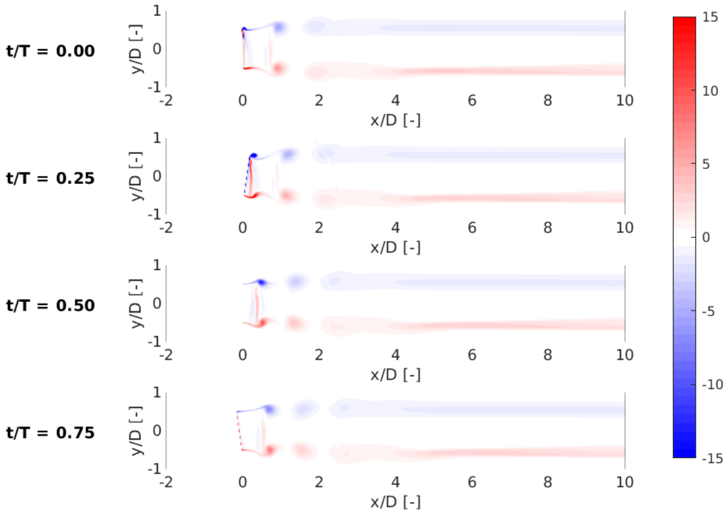

Figure 4.51: Contour of normalized Z vorticity ($\omega_z D/U_\infty$) for Case20 - $C_T = 0.8$; $\Delta C_T = -0.5$; $\theta_p = 8^o$; $\omega_{red} = 5$

Figure 4.51 presents the normalized vorticity contour corresponding to a pitching actuator disk with negative ΔC_T and pitches at a higher frequency ($\omega_{red} = 5$). This vorticity field is again observed to have a higher magnitude than the vorticity field observed in the positive ΔC_T case. This applies to the vortices shed parallel to the actuator disk also. Therefore, their effects on the induction field of the actuator are expected to be more visible in this case.

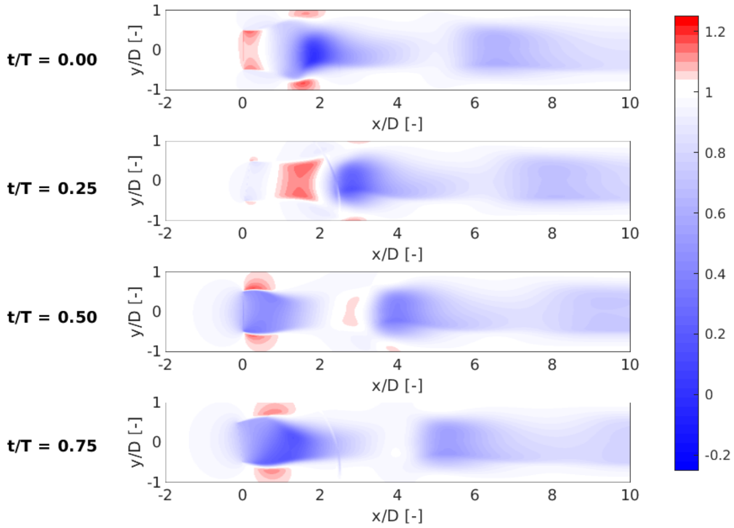

Figure 4.52: Contour of normalized X velocity (U_x/U_∞) for Case22 - $C_T = 0.5$; $\Delta C_T = 1$; $\theta_p = 8^o$; $\omega_{red} = 1$

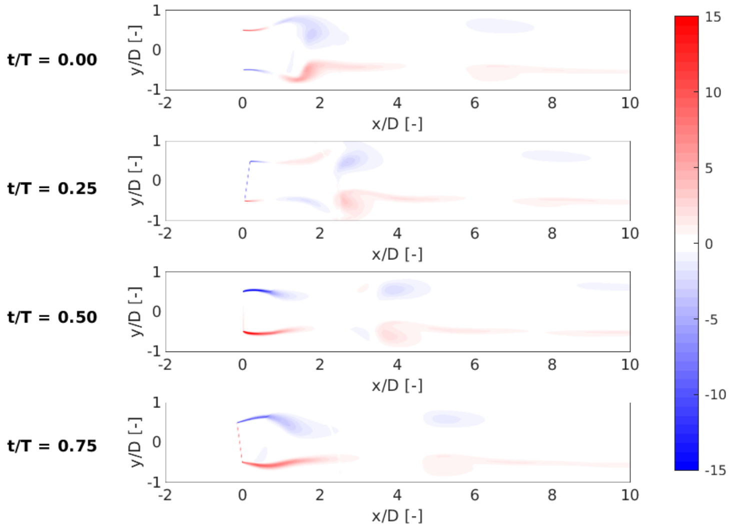

Figure 4.53: Contour of normalized Z vorticity ($\omega_z D/U_\infty$) for Case22 - $C_T = 0.5$; $\Delta C_T = 1$; $\theta_p = 8^o$; $\omega_{red} = 1$

Figure 4.52 and Figure 4.53 respectively present the normalised X velocity and Z vorticity corresponding to case 22 where ΔC_T is greater than baseline C_T. Therefore, the actuator disk will sometimes impose a negative thrust on the flow, thus speeding up the flow when it passes through the actuator. From the normalised U_x contour, it can be seen that the actuator disk is in the propeller state during this phase. The same effect is observed at $t/T = 0$ where the flow is speeding up in wake of the actuator. The occurrence of TWS is visible in this state also due to momentary occurrences of high values of C_T.

Comparison of Pitching rotor aerodynamics with Surging cases

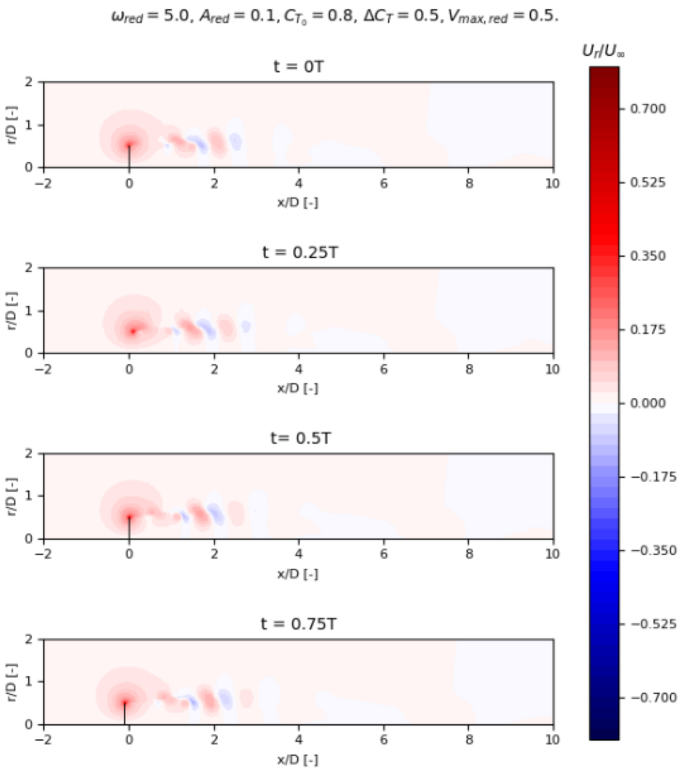

Figure 4.54: Contour of normalized Y velocity (U_x/U_∞) for Case22 - $C_T = 0.8$; $\Delta C_T = 0.5$; $\theta_p = 8^o$; $\omega_{red} = 5$

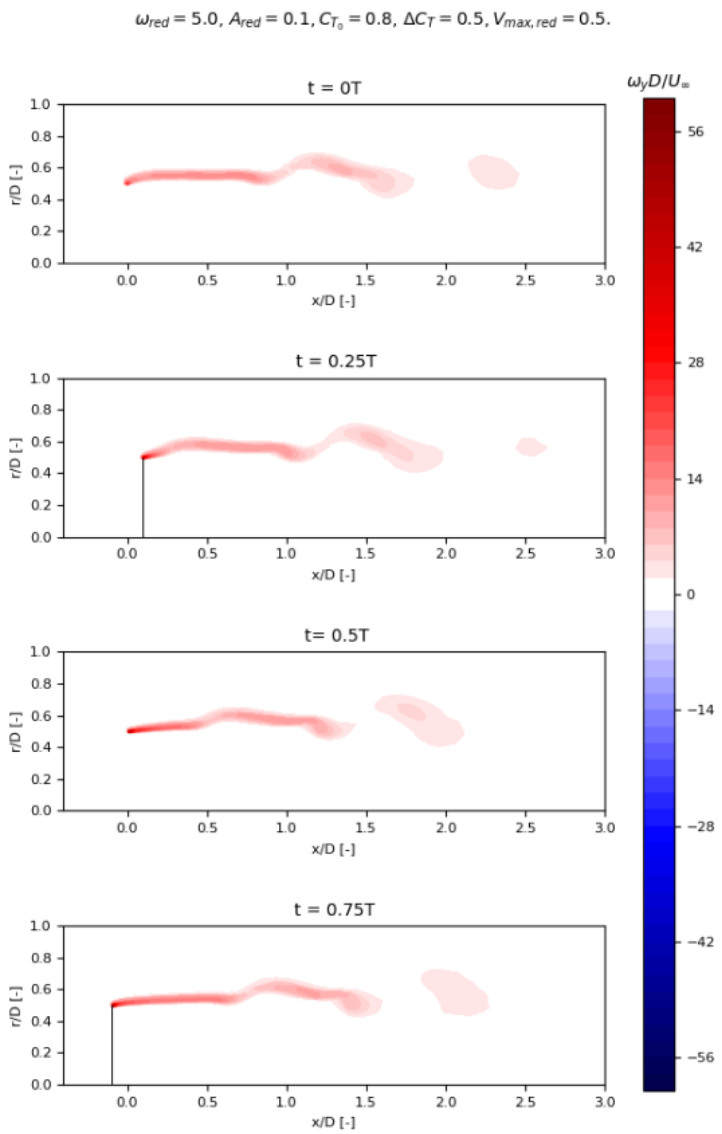

Figure 4.55: Contour of normalized Y vorticity ($\omega_y D/U_\infty$) for Case22 - $C_T = 0.8$; $\Delta C_T = 0.5$; $\theta_p = 8^o$; $\omega_{red} = 5$

Figure 4.54 and Figure 4.55 present the normalised Y velocity and Y vorticity corresponding case 17 in Table 4.2. On comparing these figures with Figure 4.44 and Figure 4.45 respectively, the same observations as done previously are observed in Section 4.2.1 and Section 4.2.2. Even though the tip vortices look slightly more unstable in the case of a surging actuator disk, it still does not possess the vortices that directly influence the induction field as observed in pitching cases.

4.2.4. Dynamic inflow model comparison

In this section, all the cases tabulated in Table 4.2 are tested against the results from the dynamic inflow model presented in Section 3.2.2. A comparative analysis of the induction field calculated from surging actuator disk CFD simulations, pitching actuator disk CFD simulations, and the induction field produced by the dynamic inflow model is done in this section. It should be noted that Ferreira's dynamic inflow model has been developed for surging actuator disks. Therefore, the results produced by the dynamic inflow model are not expected to match perfectly with pitching actuator disk CFD results. However, this comparison will help us understand the differences between these two platform motion types and thus help in developing a model for the pitching actuator disk application.

In all the plots below, the results produced by the pitching actuator CFD model, surging actuator CFD model from [2] and dynamic inflow model [3] are compared and contrasted. To provide a deeper understanding of the results produced by the pitching actuator, both the disk-averaged induction field and the induction field at $r/R = 0$ are presented. It should also be noted that the high degree of instabilities ('wiggliness') that are observed in the a_{avg} plots are slightly exaggerated and may not occur if the method calculating a_{avg} is changed by considering the velocity field throughout the actuator disk's frontal area for induction calculations. As explained in Section 3.1.4, the velocity field along $\phi = 0^o$ only is captured, and those values of inductions are extrapolated to all the other azimuths. However, the effect of those flow normal vortices that arise due to pitching will also have the most significant effect at $\phi = 0^o$. Since the pitching angular velocity will decrease as we move to other azimuths, their strength and thus their influence on the induction field will be lesser at other azimuths. Therefore, it is necessary to keep in mind that the results presented here might be slightly exaggerated than they actually are.

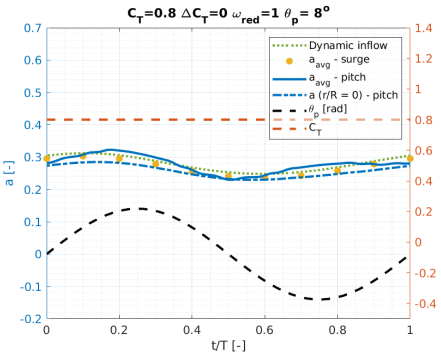

(a) Case 1

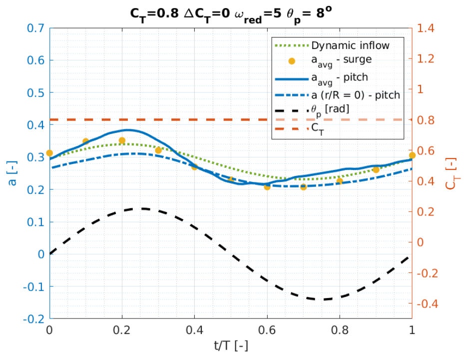

(b) Case 2

Figure 4.56: Comparison of induction field obtained from CFD results and dynamic inflow model - Case 1 and 2 from Table 4.2

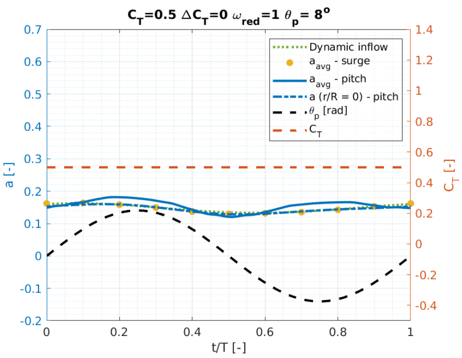

(a) Case 4

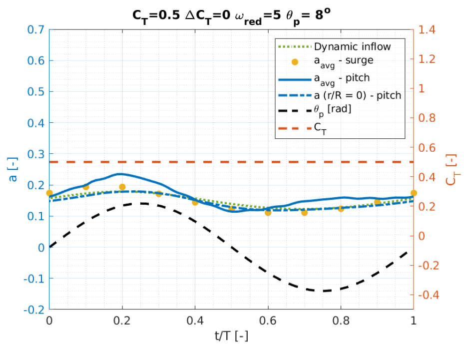

(b) Case 5

Figure 4.57: Comparison of induction field obtained from CFD results and dynamic inflow model - Cases 4 and 5 from Table 4.2

Figure 4.56 and Figure 4.57 present the comparison of the induction field calculated from the CFD model with the results from surging actuator disk and dynamic inflow is presented. These four plots correspond to the cases where the actuator is pitching while the prescribed thrust on the actuator is constant.

It can be observed that the disk-averaged induction field calculated for the surging case and the pitching case come closer at the extreme positions (at $t/T = 0$ and $t/T = 0.5$). At $t/T = 0$ and $t/T = 0.5$, where the surging and pitching cases have similar disk-averaged inductions, the magnitude of inductions calculated from CFD simulations is lower than the ones predicted by the dynamic inflow model. This observation aligns with the inference made in Section 2.4.1 that BEM tends to overpredict the results due to their inability to account for viscosity and vorticity-related effects. However, in between these time stamps, the induction fields do not match and the disk-averaged induction field of the pitching case assumes a higher magnitude than the induction field of surging cases. This can be partially attributed to the wrong method of rotor-averaged induction (a_{avg}) calculation used in this project. Therefore, it should be noted that the effects of tilt on the rotor-averaged induction results are slightly exaggerated. More details on this discrepancy are provided in Appendix C in the appendix.

The influence of the vortices shed due to the tilt of the actuator disk, that are discussed in Section 4.2.1 and Section 4.2.3, is clearly visible in the induction field. The presence of strong vortices in close proximities to the actuator disk is the reason for the higher values of the induction field while the actuator disk is pitching forward and leeward. If the induction field at $r/R = 0$ is observed, its trend closely follows the dynamic inflow model and the result produced by a surging actuator disk. This implies that the center of the actuator disk is largely unaffected by these vortices that are shed due to the tilt of the actuator disk. Therefore it can be concluded that the effect of these vortices on the dynamic response will be more pronounced at the upper and lower edges of the actuator disk than at the middle. This observation backs the fact that the strength of vortices is higher near the edges (due to higher values of ∂f_x). Also, the instability (wiggliness) of the disk-averaged induction plot signifies that the effect of these vortices on the actuator is non-linear.

On comparing the induction field of the low-frequency ($\omega_{red} = 1$) case with that of the high-frequency ($\omega_{red} = 5$) case in Figure 4.56, it is apparent that the discrepancy between surge results and pitch results is higher at the higher frequency. This again reiterates the fact this discrepancy is caused due to the vortex that is shed due to the tilt of the actuator. It is also visible that along with the increase in the magnitude of induction, this vortex introduces a phase lag in the induction field. The point maximum induction is slightly delayed compared to the point where the surge cases' induction fields reach their maximum. However, the pitching actuator results have a negative phase delay when compared to the induction field predicted by the dynamic inflow model.

On observing Figure 4.57, which presents the results of the cases with lower prescribed thrust $C_T = 0.5$, the discrepancy between the induction fields surging actuator and pitching actuator is nearly the same as observed with $C_T = 0.8$. This backs the observation made earlier that the strength of this vortex is decided more by the velocity of pitching than the prescribed thrust on the actuator.

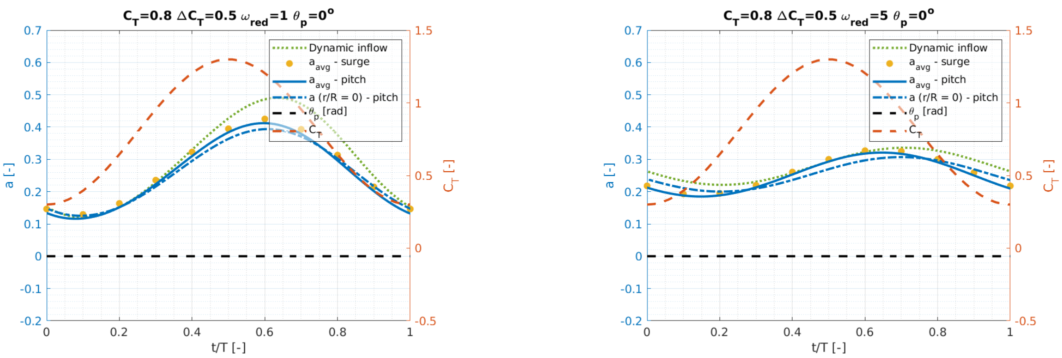

(a) Case 7

(b) Case 8

Figure 4.58: Comparison of induction field obtained from CFD results and dynamic inflow model - Cases 7 and 8 from Table 4.2

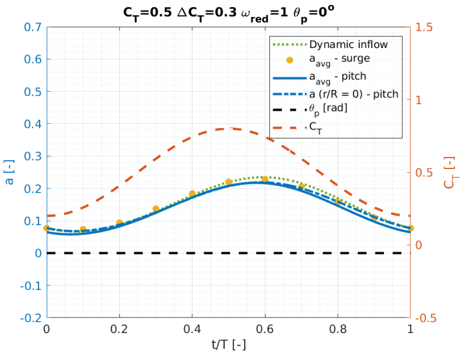

(a) Case 10

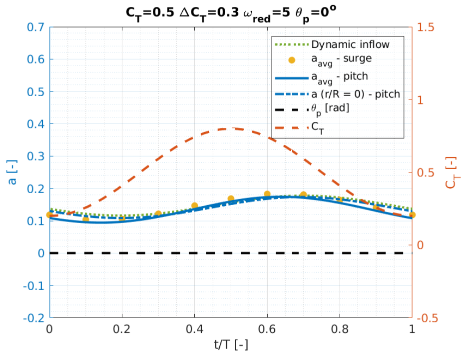

(b) Case 11

Figure 4.59: Comparison of induction field obtained from CFD results and dynamic inflow model - Cases 10 and 11 from Table 4.2

Figure 4.58 and Figure 4.59 present the comparison of induction fields corresponding to still actuator disks with dynamic thrust specification. It is clear that the disk-averaged induction fields corresponding to cases 7 and 8 are not in full agreement with the results predicted by the dynamic inflow model. The induction field of the low-frequency case (case 7) varies more from the corresponding dynamic inflow results. The magnitude of the CFD-predicted induction value is lower than the dynamic inflow model-predicted induction value. This discrepancy is more apparent during the phase where the prescribed C_T increases from the mean value ($t/T = 0.5$ to $t/T = 1$). This is the phase where the strength of tip vortices are higher than the mean value due to higher prescribed C_T. This marks that the dynamic response of tip vortices is not fully captured by the dynamic inflow model and needs to be corrected to properly account for the dynamic response of the tip vortices with higher strengths. The phase lag, in this case, seems to be negative as the peak in induction is observed at an earlier timestep than what the dynamic inflow model predicts. However, it can be noted that the induction field of the pitching actuator disk and that of the surging case are in close agreement. They both show the same lag in dynamic response when compared to the results predicted by the dynamic inflow model.

The induction field at $r/R = 0$ comes closest (with respect to the phase difference) to the result predicted by the dynamic inflow model. This confirms the observation that the influence of tip vortices is the reason behind the phase difference observed in the CFD-predicted induction field. In Section 4.2.2, it was observed that even though vortices are shed due to an imbalance in loading on the actuator disk, their strengths are insignificant compared to the strengths of vortices shed in the cases where the actuator disk was physically moving. Therefore, the non-linear effects observed in Figure 4.56 and Figure 4.57 are not visible in these cases. Also, the actuator disk is not physically moving in cases 7, 8, 10, and 11, they do not come in direct contact with the shed vortices as observed in cases 1, 2, 4, and 5. Thus, the influence of these vortices is not significant enough to cause a change in the induction field of the actuator disk.

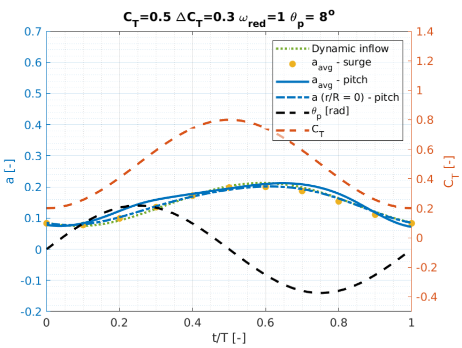

(a) Case 13

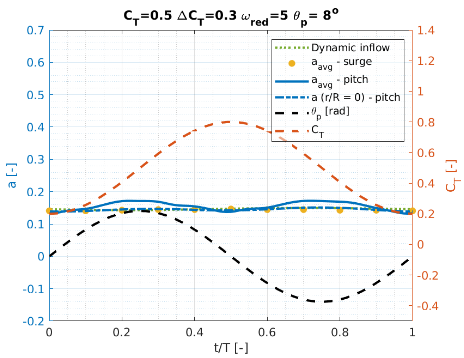

(b) Case 14

Figure 4.60: Comparison of induction field obtained from CFD results and dynamic inflow model - Cases 13 and 14 from Table 4.2

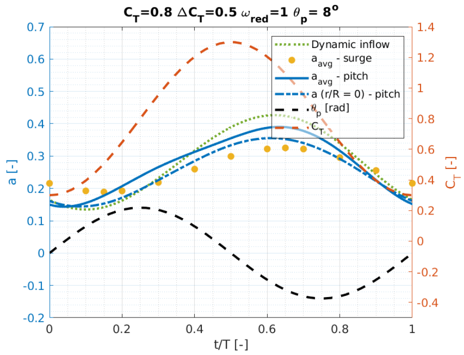

(a) Case 16

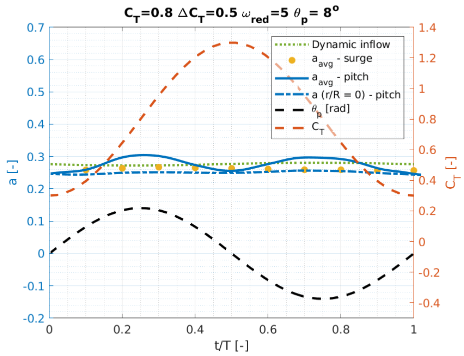

(b) Case 17

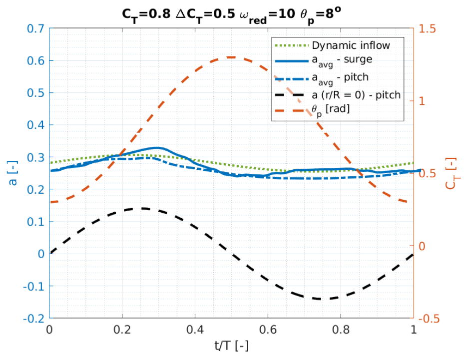

(c) Case 18

Figure 4.61: Comparison of induction field obtained from CFD results and dynamic inflow model - Cases 16, 17 and 18 from Table 4.2

Figure 4.60 and Figure 4.61 show the comparison of induction fields corresponding to the cases where the actuator disk is pitching along with a change in prescribed thrust specification. As expected from a pitching actuator disk, the influence of the vortices shed parallel to the actuator has a significant influence on the disk-averaged induction field. This is marked by the higher values of induction near $t/T = 0.25$ and $t/T = 0.75$. As observed in Figure 4.56 and Figure 4.57, the induction field predicted by $r/R = 0$ comes closer to the result predicted dynamic inflow model. This observation is (again) due to the fact that the strength of these vortices is higher near the edges than at the center. In the case with the highest frequency $\omega_{red} = 10$, the instability ('wiggliness') in the induction field is much more pronounced than in the cases with $\omega_{red} = 1$ and $\omega_{red} = 5$. This further strengthens the claim that the vortices that arise due to pitching motion have a non-linear effect on the induction field.

On comparing the induction field from Figure 4.61, it can be clearly observed that the difference between maximum and minimum values of induction is higher in the pitching case than in the surging case. This effect is also observed in Figure 4.60 but the difference between the induction fields is less pronounced than with the cases with higher thrust. This observation states that the actuator might experience higher fatigue when it is pitching than when it is surging.

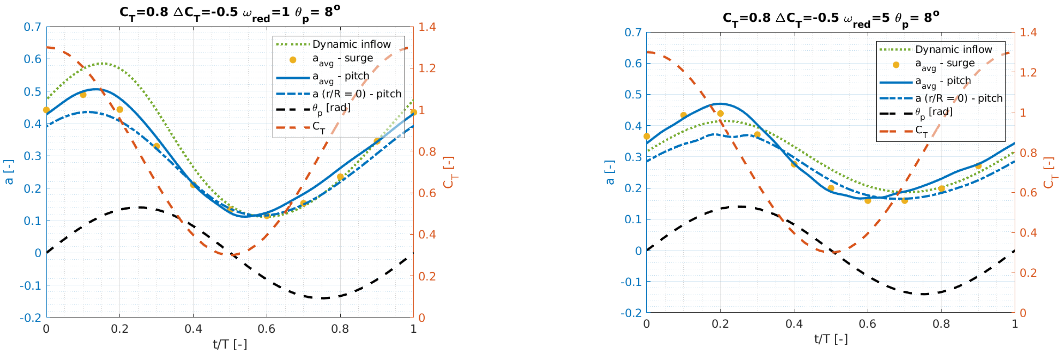

(a) Case 19 **(b)** Case 20

Figure 4.62: Comparison of induction field obtained from CFD results and dynamic inflow model - Cases 19 and 20 from Table 4.2

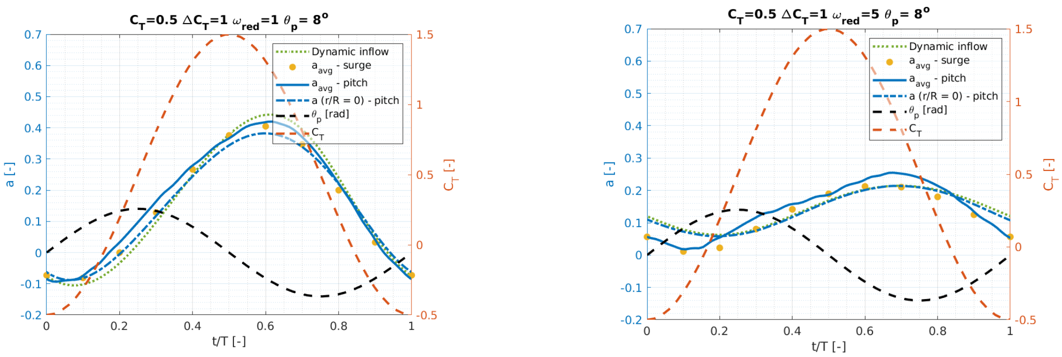

(a) Case 22 **(b)** Case 23

Figure 4.63: Comparison of induction field obtained from CFD results and dynamic inflow model - Cases 22 and 23 from Table 4.2

In extreme loading cases, with negative ΔC_T and with $\Delta C_T > C_T$, the dynamic inflow seems to overpredict the disk-averaged induction values when the actuator is pitching leeward and underpredict when the actuator is pitching forward. On noticing the peaks of inductions predicted by the CFD model and the dynamic inflow model, a visible negative phase delay is also visible in the induction field. However, the pitching actuator's induction field seems to have a positive phase delay with respect to the induction of the surging case. This is in correspondence with the observation made from Figure 4.56 and Figure 4.57.

In both Figure 4.62 and Figure 4.63, the 'wiggliness' in disk-averaged induction is more prominent in the high-frequency case. This is again due to the stronger vortices shed from the actuator disk due to the disk's tilt. As observed with the other cases, the closest agreement between pitching CFD results, dynamic inflow results, and surging CFD results is observed at $t/T = 0$, $t/T = 0.5$, and $t/T = 1$ because of the absence of these vortices.

Deeper analysis on the induction field behaviour

In this section, induction fields along different radial positions are presented to provide a deeper understanding of the non-linear induction response observed in the last section. The radial distribution should give a comprehensive view of which parts of the actuator disk are most affected by the vortex shed due to the actuator disk's tilt.

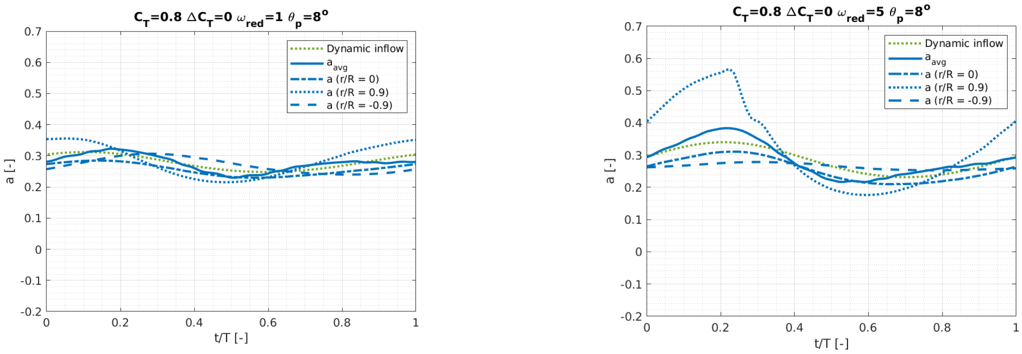

(a) Case 1

(b) Case 2

Figure 4.64: Comparison of induction field at different radial positions with dynamic inflow induction - Cases 1 and 2 from Table 4.2

Figure 4.64 provides the disk-averaged induction field predicted by the CFD model along with the induction field at radial positions $r/R = 0$, $r/R = 0.9$, and $r/R = -0.9$. Please note that cases 1 and 2 simulate pitching actuator disks with constant prescribed thrust. Therefore, the effects observed are purely a result of the actuator disk's motion. As it can be observed from Figure 4.64a, the induction fields corresponding to $r/R = 0$, $r/R = 0.9$, and $r/R = -0.9$ show a stable (without the 'wiggliness' in plots) behaviour hinting that the induction effects are linear at low pitching frequencies. But the disk-averaged induction shows instability to a certain extent. It can also be noted that the induction fields corresponding to the top and bottom extremities ($r/R = 0.9$ and $r/R = -0.9$) are significantly different. Even though vortices of strength comparable to that of the tip vortices are not shed in the low-frequency case, the difference in the induction field between different radial positions is significant enough to display an 'unsteady' behaviour in the disk-averaged induction. Therefore, the unsteadiness in a_{avg} can be attributed to the difference in inductions between different radial positions. With regards to the higher frequency case (Figure 4.64b), the difference in induction fields is more prominent and the induction field at $r/R = 0.9$ shows a non-linear trend between $t/T = 0.25$ and $t/T = 0.5$ where the actuator disk is pitching forward from its leeward extreme position. It is also noteworthy that this is the time period where the actuator disk will (partially) be in its own wake, given that the pitching velocity is high enough.

The phase difference between different radial positions is also prominent in these plots in which the induction field at $r/R = 0$ follows closely the result predicted by the dynamic inflow model. On comparing the phase differences between the induction fields at different radial positions, induction corresponding to $r/R = -0.9$ has a noticeable negative phase delay while induction at $r/R = 0.9$ has a positive phase delay while the phase delay of a_{avg} comes somewhere in between.

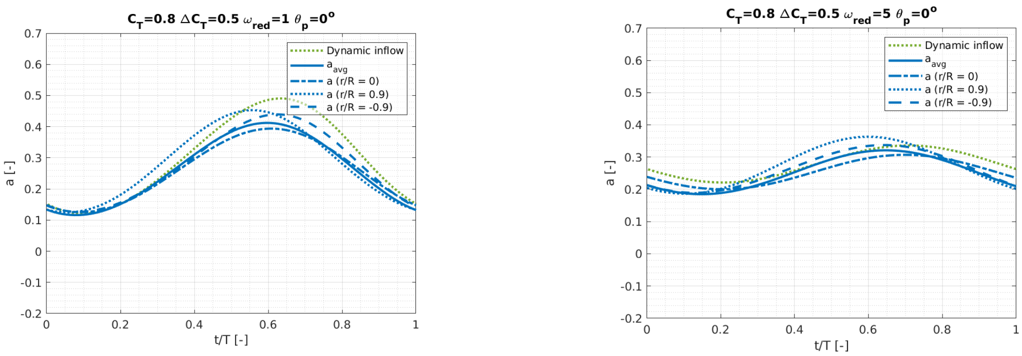

(a) Case 7

(b) Case 8

Figure 4.65: Comparison of induction field at different radial positions with dynamic inflow induction - Cases 7 and 8 from Table 4.2

Figure 4.65 presents the induction field corresponding to the cases with still actuator disk and dynamic thrust. As it is apparent from these plots that the differences in load and phase between the induction fields is not as significant as it was in the cases with moving actuator disks (refer to Figure 4.64). Since these differences are not radical, a_avg also has a smooth profile when compared to the a_avg trend observed with moving actuator disks. Even though the difference is not as pronounced as it was observed in the case set with moving actuators, due to the periodic change in the direction of the prescribed thrust, a difference is observed in both the magnitude and phase difference of the inductions. However, an interesting behaviour is observed with the induction field corresponding to the radial position $r/R = -0.9$. As opposed to Figure 4.64, the induction field at $r/R = -0.9$ show a significant variation in magnitude throughout the cycle while a flatter behaviour was observed in moving cases. Even though the magnitude of inductions is different, the observation with respect to phase difference (with respect to a_avg) is maintained. The induction field at $r/R = -0.9$ has the highest positive phase delay while $r/R = 0.9$ has the highest negative phase delay. On observing Figure 4.65b that has a higher frequency of thrust variation, the induction field corresponding to $r/R = 0$ has the highest positive phase delay.

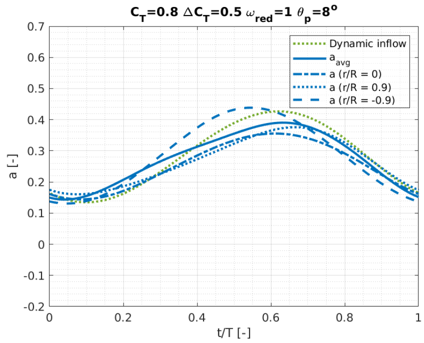

(a) Case 16

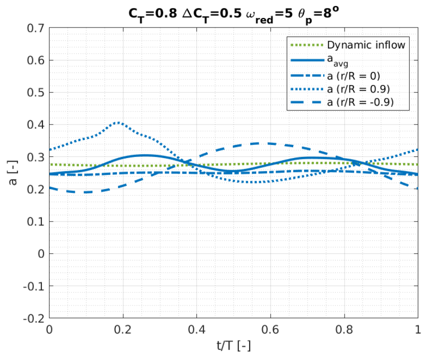

(b) Case 17

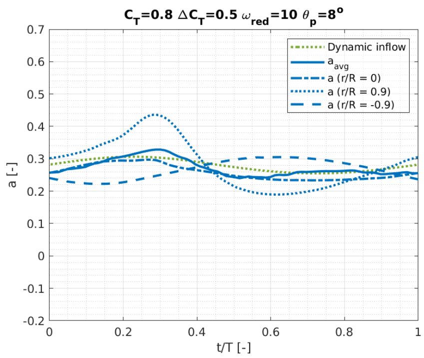

(c) Case 18

Figure 4.66: Comparison of induction field at different radial positions with dynamic inflow induction - Cases 16, 17, and 18 from Table 4.2

Figure 4.66 presents the induction field corresponding to the cases with moving actuator disks with dynamic thrust specification. The observations made on Figure 4.64 about the magnitude and phase difference of induction fields are apparent in this case except for the low-frequency case Figure 4.66a. For the high-frequency cases, the induction field corresponding to $r/R = 0.9$ assumes the highest magnitude and also the highest phase delay. Similar to the observation made in Figure 4.64, the induction field corresponding to $r/R = -0.9$ is nearly out of phase ($\phi = 180^o$) with the induction field at $r/R = 0.9$. The difference between the magnitudes of inductions also seems to increase with increasing frequency which also hints that the non-linearity in $a_avg$nce plots. This backs the claim made in Section 4.2.3 that the strength and thus the influence of the vortex shed due to the tilt of the actuator disk increases with an increase in frequency. An interesting observation made in Figure 4.66c is that the induction field at $r/R = 0$ also shows instabilities at the region between $t/T = 0.25$ and $t/T = 0.5$. This marks that at very high frequencies, these vortices can be strong enough to influence the induction field at the center of the disk too.

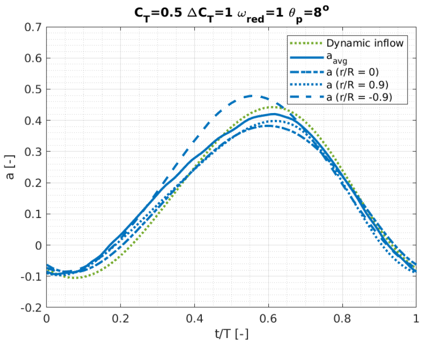

(a) Case 22

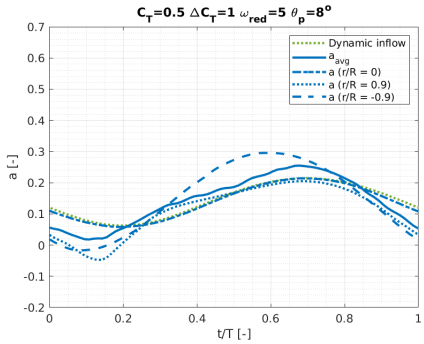

(b) Case 23

Figure 4.67: Comparison of induction field at different radial positions with dynamic inflow induction - Cases 22 and 23 from Table 4.2

The behaviour of inductions seen in Figure 4.66a is observed in both these cases shown in Figure 4.67. The phase difference between dynamic inflow in all the cases seen so far (except for cases 16, 22, and 23) had a trend such that the induction at $r/R = 0.9$ has the highest positive phase delay while the induction field at $r/R = -0.9$ will have the highest negative phase delay. However, in Figure 4.66a and Figure 4.67, the trend of phase delays and the magnitudes of the induction field are both reversed. There is no significant non-linearity in the a_{avg} field also. This shows that, at high values of thrust, the vortices shed parallel to the actuator do not have a significant influence on the induction field. As seen in Figure 4.53, these vortices even though are present in the wake, they are further downstream than it was in cases 2 and 17 where the induction field is dominated by the effects of pitching motion. Therefore, even though these normal vortices are strong enough, they do not bother with the actuator's induction field.

5
Conclusion

In this chapter, the concluding remark on the outcome of this thesis project is presented. In an effort to understand the pitching motion dynamics and the engineering models to model the dynamic response, an extensive literature study was carried out. The inferences of which are provided in Chapter 2. In order to study the aerodynamics of a pitching floating offshore wind turbine, an actuator disk model was created. The actuator disk is assumed to follow a sinusoidal pitching motion and this motion is modeled by employing an Arbitrary Mesh Interface (AMI) method. A detailed explanation of the process of model creation and validation is presented in Chapter 3. Even though it was initially planned to analyse the tip effects also using an actuator line model, considering the time taken to develop and validate an actuator line model, it was decided to proceed with just the actuator disk model.

In Chapter 4, an analysis of the accuracy of yaw models is provided by discussing the steady actuator disk simulations. Following that, a detailed analysis of the aerodynamics of the pitching wind turbine is presented in Section 4.2. The induction field predicted by the CFD model is compared with the results predicted by the dynamic inflow model [3]. In the current section, a summary of the results is made and conclusions are drawn upon the observations made in the results section.

5.1. Summary of the results obtained

The platform pitching motion has a significant influence on the aerodynamics of the FOWT's rotor. Since the relative velocity of inflow air follows a sinusoidal profile, the induction field (along with the other rotor dynamics) also tends to follow a sinusoidal profile. Usage of three different types of simulations helped in identifying the individual effects of actuator motion and thrust exerted by the actuator to a great extent.
Results obtained from the first set of simulations, where the prescribed thrust on the actuator is maintained while the actuator undergoes a pitching motion, show purely the effects of platform motion. They can be summarised as follows:

1. Pitching motion of the actuator gives rise to a meander in the wake. This meandering effect is mainly due to the actuator's pitching motion and the difference in locations at which the tip vortices are shed downstream.
2. Due to the pitching motion, the tip vortices get lumped at the edges during the leeward motion and are shed when the actuator starts pitching forward. Due to the tilt of the actuator disk, these vortices are shed at slightly different positions which adds to the asymmetry of the wake.
3. The gradient of loading ($\partial f_x/\partial y$) due to the tilt of the actuator disk during pitching motion gives rise to extra vorticities that are shed normal to the freestream. These vortices are shed both during forward and leeward pitch motions. The process by which these vortices are created and shed is explained in Section 4.2.1. One of these vortices (the vortex with positive magnitude) is shed during the pitching phase from $t/T = 0.5$ to $t/T = 0$ while the other vortex with negative magnitude is shed during the remaining half of the cycle.
4. The strength of these vortices is high and comes close to the strength of the tip vortices. But the strength of the positive vortex seems to be slightly higher than the negative vortex. This is due to

the difference in angular velocities (and thus the relative velocities) between the top and bottom edges of the actuator disk. The strength of these vortices increases with an increase in pitching frequency (i.e. with the pitching velocity V_{max}).

5. The actuator disk is very close to these vortices and sometimes crosses these vortices while pitching leeward. Therefore, they have a significant effect on the induction field of the actuator. This can be seen clearly in the induction field comparison plots presented in Section 4.2.4. These vortices, regardless of their direction (+ve or -ve), lead to an increase in the induction values, and their effects are most pronounced while the actuator is between the extreme positions.
6. These vortices have higher strengths near the actuator's edges and lower strengths near the center (at $r/R = 0$). Thus, they tend to have more significant effects near the actuator's edges than at the center.
7. These vortices have a significant effect on the phase delay of the induction fields too. The induction field corresponding to the lower edge ($r/R = -0.9$) has the highest negative phase delay while the induction corresponding to the upper edge ($r/R = 0.9$) has the highest positive phase delay when compared with the induction field of a surging actuator.
8. Since the vortices get stronger as the pitching velocity increases, the agreement between pitching CFD results, surging CFD, and the dynamic inflow results is better at low frequencies and gets worse at higher frequencies.
9. Complex wake states such as TWS are not observed in these cases because the thrust response was not high enough. Therefore, as long as the thrust response is low enough and the pitching frequency is high enough, TWS will not occur in an actuator pitching a constant thrust.

Results corresponding to a still actuator disk help us identify the effect of thrust specification on the pitching rotor's aerodynamics and the induction field. These results can be summarised as follows:

1. Due to a smaller gradient of forces on the actuator disk and the absence of pitching dynamics, the wake also undergoes lesser meandering but is not absent.
2. TWS was observed in low-frequency cases when the prescribed thrust goes above a value of $C_T = 1$. This marks the need for special empirical corrections to predict the wake characteristics when the rotor is expected to reach such high values of thrusts.
3. Wake meandering is observed in this case also but has a phase shift close to 180^o with the wake pattern observed in the case with a physically pitching actuator disk. This leads to the conclusion that the wake meandering dynamics are positively influenced by the motion.
4. The vortices that are shed due to the gradient in loading can be seen in the case of a still actuator disk too. But the magnitude of these vortices is much lesser compared to the vortices observed in the moving actuator disk case.
5. Since these vortices are not strong enough, their influence on the induction field is largely absent. The induction field of the pitching actuator disk is in good agreement with the results predicted by the dynamic inflow model and thus comes close to the surging CFD results also.

The last set of simulations simulates an actuator disk that pitches physically with a dynamic prescribed thrust. Highlights of the results obtained are as follows:

1. Since the thrust on the actuator disk momentarily goes above $C_T = 1$, TWS occurs in this case too.
2. The vortices that are shed parallel to the actuator disk due to the motion of the actuator disk seem to have different strengths than they possessed in the cases with constant thrust. The strength of the negative vorticity increases while the strength of the positive vorticity decreases. Thus, regardless of the type of simulation, a strong gradient in loading persists on the actuator disk due to its pitching motion.
3. Even though the thrust specification is also varied according to the pitching dynamics, the vortices that are shed due to the tilt have a significant influence at higher frequencies. Therefore, the agreement between dynamic inflow results, surging CFD, and pitching CFD is good at low frequencies. But at higher frequencies, the pitching CFD shows significant disagreement with both these results.

4. TWS state was observed to occur in low-frequency cases but is absent in high-frequency cases. In low-frequency cases, the flow had enough time to adapt to the thrust actuation and is not largely influenced by the kinematic effects of pitching motion due to low pitching velocity. Since the effect of pitching motion is high, the flow does not have time to adapt to the thrust response and is affected more by the pitching motion. Thus, a more chaotic wake without TWS and VRS states is observed at high frequencies.

5.2. Answers to the research questions

- **What is the influence of pitching platform motion on the rotor aerodynamics of a FOWT?** The primary influences of the pitching motion are the effects that arise due to the dynamic tilt of the actuator disk. This introduces an artificial meandering of the wake with significant regions of upwash and downwash in the wake region. The tilt in the actuator disk also leads to a new set of vortices being shed from the rotor region due to a gradient in the force field. These vortices are nearly as strong as the tip vortices and are close to the induction region of the actuator disk. Since the actuator disk is moving, they sometimes tend to fall within the regions with high vorticity. Therefore, these vortices have a complex effect on the induction field of the actuator disk. These vortices affect both the magnitude of the inductions and also the phase delay of the induction fields. Due to this reason, the induction field near the bottom edge seems to have a negative phase delay (when compared with the inductions predicted by the surging CFD model) and the phase delay slowly increases for the induction fields near the top edge. The induction field near the top edge of the actuator has the highest positive phase delay. It was also observed that the induction field corresponding to the upper part of the actuator disk experiences the highest effect of pitching motion (marked by the highest difference in induction magnitudes in a pitching cycle). This part also shows the highest instability due to the vortices shed normally to the flow.

  – **Can these actuator disk models be utilized for studying the aerodynamics of a pitching FOWT? If that's the case, which model better predicts the aerodynamics of pitching FOWTs – Is it better to use a model with a stationary rotor and a non-uniform load prescription or a model with a dynamic rotor and uniform loading?**

    Given their capability to account for the effects of dynamic tilting, the actuator disk model is capable of producing accurate enough results in the case of a pitching FOWT. The effects of rotor tilt are captured accurately. But the unsteadiness effects predicted using an actuator disk may not exactly represent the effects that might arise in a finite-bladed rotor case because an actuator disk is continuous along the radial axis. In the case of an actuator disk simulation, the effects of rotor tilt are applied to the maximum extent (at $\Psi = 0^o$ and $\Psi = 180^o$) throughout the rotor span. However, the effect of tilt experienced in reality by the finite blades will be lesser in magnitude when they are present in azimuths other than $\psi = 0^o$ or $\psi = 180^o$. Therefore, the effect of rotor tilt observed in the case of an actuator disk is expected to be exaggerated and also is expected to be slightly higher than the effects that will be observed in a blade-resolved CFD model. The effects also vary and become more unsteady depending on the phase difference, TSR, and pitching frequency of the rotor. Also, the vortices that arise due to tilt might interact with the finite tip and hub vortices that can be captured using an actuator line model. Thus, an actuator disk model is capable enough to understand the broad (macro) effects of pitching motion and probably also to conduct wind farm scale studies. However, an actuator line model will provide a more representative view of the effects of pitching in a FOWT.

    Since this is one of the first studies on the induction field of a pitching wind turbine, there are not many publications to compare the obtained results with. Therefore, the relevance of the three types of actuator disk models discussed in this thesis is not known for sure. However, the third method where both the actuator disk and the prescribed load are dynamic provides the closest representation of the induction field and thrust response recorded by past research. Therefore, it is recommended to use the third method to create a simple and representative model of a pitching FOWT.

- **What are the essential differences between a pitching actuator disk and a surging actuator**

disk with respect to the induction field and near wake aerodynamics?

The first difference observed between pitching and surging actuator disks is with the wake. A surging actuator produces an unstable wake that is symmetric along the rotor axis but the pitching cases produce a meandering wake. The most important difference observed in the case of a pitching actuator is the presence of vortices normal to the freestream. Since the rotor does not tilt when an actuator surges, the gradient of normal force ($\partial f_x/\partial y$) is insignificant. However, when the actuator is pitching this gradient is steep enough to shed vortices that are nearly as strong as the vortices shed from the edges. Since the actuator is pitching continuously, the actuator sometimes comes in contact with these vortices. Thus these vortices have a complex effect on the induction field of the actuator. The strength of these vortices increases when the pitching frequency of the actuator disk marking that they are primarily an effect of the actuator's pitching. The dynamic response due to the vortex that is shed due to the rotor's tilt seems to vary radially in the case of a pitching actuator. The induction field corresponding to the lower edge of the actuator disk $r/R < 0$ has a negative phase delay while the inductions corresponding to the upper edge $r/R > 0$ seem to have a positive phase delay. This behaviour will not be seen in a surging case as the only source of a dynamic effect are the vortices that are shed due to rotor tilt and these vortices are not shed in the case of a surging actuator disk because of axisymmetric loading.

– **Can the dynamic inflow model developed for surging wind turbines [3] be used for pitching cases also? If not, what needs to be considered for developing a new dynamic inflow model?**

  No, the dynamic inflow model created for a surging actuator cannot be applied to all the pitching cases yet. When the pitching amplitude and frequency are low enough such that there is no notable gradient in the force field of the actuator disk, the dynamic inflow model is capable of producing good results. However, when there is a significant gradient in the force field (due to whatever reason), the dynamic inflow model fails to capture the full effects. The vortices that are shed due to the gradient in the actuator's loading are the reason behind the claim. The dynamic inflow model accurately predicts the induction field of a still actuator disk with dynamic loading because the vortices shed due to the gradient in axial loading of the actuator disk do not have a significant influence on the induction field. However, in the cases where the actuator disk is physically moving, these vortices have a complex non-linear effect on the induction field which is not captured by the dynamic inflow model. Therefore, the dynamic inflow model needs to be modified to take these vortices into account. These vortices tend to affect both the value of induction and also the phase delay of the induction field.

- **How accurate are the yaw correction models to be applied for pitching actuator disk cases?**

  The yaw correction models are tested only on the steady-state results where the tilt of the actuator disk is constant. Since the tip corrections are not applied to the induction field predicted by the engineering models, only the slopes of the induction fields were considered to check the accuracy. With regards to that, White and Blake's model [103] shows good correspondence with the CFD results. Since the model does not capture the tip effects, which Oye's model [51] does, Oye's model's method of calculating Coleman's constant ($K(\chi)$) was changed to the method used by White and Blake. This new model shows a better agreement with the CFD results than all the other original models discussed in this thesis. Therefore, with appropriate tip corrections, White and Blake's model is capable of predicting yawed rotor's induction fields.

5.3. Recommendations for future work

This thesis attempted to analyze the aerodynamics of a pitching FOWT using a more simple actuator disk model. However, an actuator disk model is initially created with an assumption of uniform load on the actuator. Since that is not the case with a pitching rotor, the effects of tilt might not be captured to the fullest extent. The complex interaction between finite tip vortices and the vortices that arise due to the tilt of the rotor is not captured in an actuator disk model. Since the strength of these vortices (that are shed due to the rotor's tilt) is close to that of the tip vortices and the effect of the vortices is already observed to be non-linear, it is more beneficial to study their interaction in depth. Therefore, it is recommended to carry out an actuator line simulation of a pitching wind turbine to capture these non-linear effects in detail. It is also recommended to compare the results predicted by the actuator disk model with the results of the actuator line model. If the discrepancy between the results predicted by the actuator line model and the actuator disk model is not significant, then the actuator disk model can be recommended for its modelling simplicity.

It is will be more beneficial to use an actuator line model with airfoil data as the influence of tilt varies with the radial position. Since the strength of the vortices that are shed normally to freestream depends on the gradient of loading on the actuator line, it is essential to capture the thrust response of the rotor accurately. Using an actuator line model with airfoil data will provide a much more realistic idea of a pitching wind turbine because the vortices that are shed due to the rotor's tilt can influence the angle of attack of the inflow. This leads to a more accurate prediction of the loads on the actuator and thus a more accurate prediction of the vortices that are shed due to imbalances in the loading of the rotor. From the inferences made from past research, it was identified the pitching dynamics (amplitude and frequency) do not have the same effect on the rotor always. The behaviour observed at low TSRs is different from the behaviour observed at high TSRs as Wen [43] indicates. Using an actuator line model can help us understand this phenomenon better and account for the effects of TSR also while designing an appropriate engineering model to predict pitching FOWT dynamics.

The method of calculating the disk-averaged induction in this thesis is not entirely accurate. The method used in this project captures the induction field at different radial positions along $\Psi = 0^o$ and $\Psi = 180^o$ and assumes the same induction throughout that annulus. That is, the elements of the same annulus that are in different azimuthal positions are assumed to have the same induction value as the element at $\Psi = 0^o$ or $\Psi = 180^o$ has. This method is definitely representative of the induction values of an actuator disk in tilt but is not 100% accurate. The part of the annuli that are in between $\Psi = 0^o$ and $\Psi = 180^o$ will have a lower impact of tilt than the elements that are along the vertical. Therefore, the effects of rotor tilt on the disk-averaged induction in Section 4.2.4 are slightly exaggerated than they actually are. Therefore, it is recommended to capture the induction field across the whole actuator disk to calculate the disk-averaged induction.

Bibliography

[1] C.-H. K. Wu and V.-T. Nguyen, "Aerodynamic simulations of offshore floating wind turbine in platform-induced pitching motion," *Wind Energy*, vol. 20, no. 5, pp. 835–858, 2017.

[2] A. Sala, "Cfd study of induction and finite blade effect on a floating horizontal-axis wind turbine," 2021.

[3] C. Ferreira, W. Yu, A. Sala, and A. Vire, "Dynamic inflow model for a floating horizontal axis wind turbine in surge motion," *Wind Energy Science Discussions*, pp. 1–22, 2021.

[4] T. Tran, D. Kim, and J. Song, "Computational fluid dynamic analysis of a floating offshore wind turbine experiencing platform pitching motion," *Energies*, vol. 7, no. 8, p. 5011–5026, 2014.

[5] T. T. Tran and D. H. Kim, "The aerodynamic interference effects of a floating offshore wind turbine experiencing platform pitching and yawing motions," *Journal of Mechanical Science and Technology*, vol. 29, no. 2, pp. 549–561, 2015.

[6] D. M. Eggleston and F. Stoddard, "Wind turbine engineering design," 1987.

[7] J. N. Sørensen, W. Z. Shen, and X. Munduate, "Analysis of wake states by a full□field actuator disc model," *Wind Energy*, vol. 1, no. 2, p. 73–88, 1998.

[8] M. Jeon, S. Lee, and S. Lee, "Unsteady aerodynamics of offshore floating wind turbines in platform pitching motion using vortex lattice method," *Renewable Energy*, vol. 65, pp. 207–212, 2014.

[9] T. Burton, N. Jenkins, D. Sharpe, and E. Bossanyi, *Wind energy handbook*. John Wiley & Sons, 2011.

[10] P. J. Moriarty and A. C. Hansen, "Aerodyn theory manual," National Renewable Energy Lab., Golden, CO (US), Tech. Rep., 2005.

[11] A. Suzuki, *Application of dynamic inflow theory to wind turbine rotors*. The University of Utah, 2000.

[12] L. A. Martínez-Tossas, M. J. Churchfield, and S. Leonardi, "Large eddy simulations of the flow past wind turbines: actuator line and disk modeling," *Wind Energy*, vol. 18, no. 6, pp. 1047–1060, 2015.

[13] X. Shen, P. Hu, J. Chen, X. Zhu, and Z. Du, "The unsteady aerodynamics of floating wind turbine under platform pitch motion," *Proceedings of the Institution of Mechanical Engineers, Part A: Journal of Power and Energy*, vol. 232, no. 8, pp. 1019–1036, 2018.

[14] V. Leble and G. Barakos, "10-mw wind turbine performance under pitching and yawing motion," *Journal of Solar Energy Engineering*, vol. 139, no. 4, p. 041003, 2017.

[15] B. Wen, X. Dong, X. Tian, Z. Peng, W. Zhang, and K. Wei, "The power performance of an offshore floating wind turbine in platform pitching motion," *Energy*, vol. 154, pp. 508–521, 2018.

[16] A. Ortolani, G. Persico, J. Drofelnik, A. Jackson, and M. S. Campobasso, "High-fidelity calculation of floating offshore wind turbines under pitching motion," in *Turbo Expo: Power for Land, Sea, and Air*, vol. 84249. American Society of Mechanical Engineers, 2020, p. V012T42A012.

[17] W. Shi, J. Jiang, K. Sun, and Q. Ju, "Aerodynamic performance of semi-submersible floating wind turbine under pitch motion," *Sustainable Energy Technologies and Assessments*, vol. 48, p. 101556, 2021.

[18] K. Sivalingam, A. Bahuguni, J. Gullman-Strand, P. Davies, and V. Tan NGUYEN, “Effects of platform pitching motion on floating offshore wind turbine (fowt) rotor,” in *Offshore Technology Conference*. OnePetro, 2015.

[19] A. Ortolani, G. Persico, J. Drofelnik, A. Jackson, and M. S. Campobasso, “Cross-comparative analysis of loads and power of pitching floating offshore wind turbine rotors using frequency-domain navier-stokes cfd and blade element momentum theory,” in *Journal of Physics: Conference Series*, vol. 1618, no. 5. IOP Publishing, 2020, p. 052016.

[20] [Online]. Available: https://unfccc.int/sites/default/files/english_paris_agreement.pdf

[21] “A european green deal,” Apr 2022. [Online]. Available: https://ec.europa.eu/info/strategy/priorities-2019-2024/european-green-deal_en

[22] “Wind energy today.” [Online]. Available: https://windeurope.org/about-wind/wind-energy-today/

[23] W. Musial and S. Butterfield, “Future for offshore wind energy in the united states: Preprint.” [Online]. Available: https://www.osti.gov/biblio/15007876

[24] J. M. Jonkman, “Dynamics of offshore floating wind turbines-model development and verification,” *Wind Energy*, vol. 12, no. 5, p. 459–492, 2009.

[25] W. E. HERONEMUS, “Pollution-free energy from offshore winds,” *8th Annual Conference and Exposition, Marine Technology Society, Sep. 11-13, 1972, Washington, D. C.*, 1972. [Online]. Available: https://ci.nii.ac.jp/naid/10029324950/en/

[26] T. Sebastian and M. Lackner, “Characterization of the unsteady aerodynamics of offshore floating wind turbines,” *Wind Energy*, vol. 16, no. 3, p. 339–352, 2012.

[27] J. M. Jonkman, M. L. Buhl Jr *et al.*, “Fast user’s guide,” *Golden, CO: National Renewable Energy Laboratory*, vol. 365, p. 366, 2005.

[28] J. Dong and A. Viré, “Comparative analysis of different criteria for the prediction of vortex ring state of floating offshore wind turbines,” *Renewable Energy*, vol. 163, p. 882–909, 2021.

[29] C. Lienard, R. Boisard, and C. Daudin, “Aerodynamic behavior of a floating offshore wind turbine,” *AIAA Journal*, vol. 58, no. 9, pp. 3835–3847, 2020.

[30] H. Lee and D.-J. Lee, “Effects of platform motions on aerodynamic performance and unsteady wake evolution of a floating offshore wind turbine,” *Renewable Energy*, vol. 143, p. 9–23, 2019.

[31] A. Rezaeiha and D. Micallef, “Wake interactions of two tandem floating offshore wind turbines: Cfd analysis using actuator disc model,” *Renewable Energy*, vol. 179, pp. 859–876, 2021.

[32] R. Corniglion, J. Harris, C. Peyrard, and M. Capaldo, “Comparison of the free vortex wake and actuator line methods to study the loads of a wind turbine in imposed surge motion,” in *Journal of Physics: Conference Series*, vol. 1618, no. 5. IOP Publishing, 2020, p. 052045.

[33] B. Schliffke, S. Aubrun, and B. Conan, “Wind tunnel study of a “floating” wind turbine’s wake in an atmospheric boundary layer with imposed characteristic surge motion,” in *Journal of Physics: Conference Series*, vol. 1618, no. 6. IOP Publishing, 2020, p. 062015.

[34] S. Mancini, K. Boorsma, M. Caboni, M. Cormier, T. Lutz, P. Schito, and A. Zasso, “Characterization of the unsteady aerodynamic response of a floating offshore wind turbine to surge motion,” *Wind Energy Science*, vol. 5, no. 4, pp. 1713–1730, 2020.

[35] S. N. Rodriguez and J. W. Jaworski, “Strongly-coupled aeroelastic free-vortex wake framework for floating offshore wind turbine rotors. part 2: Application,” *Renewable Energy*, vol. 149, pp. 1018–1031, 2020.

[36] R. Kyle, Y. C. Lee, and W.-G. Früh, “Propeller and vortex ring state for floating offshore wind turbines during surge,” *Renewable Energy*, vol. 155, pp. 645–657, 2020.

[37] K. Kopperstad, K. Shoele, and R. Kumar, “A combined experimental and numerical study of the floating wind turbines,” in *2018 Applied Aerodynamics Conference*, 2018, p. 3828.

[38] J. Kim and H. Shin, “Validation of a 750 kw semi-submersible floating offshore wind turbine numerical model with model test data, part ii: Model-ii,” *International Journal of Naval Architecture and Ocean Engineering*, vol. 12, pp. 213–225, 2020.

[39] H. Ahn and H. Shin, “Experimental and numerical analysis of a 10 mw floating offshore wind turbine in regular waves,” *Energies*, vol. 13, no. 10, p. 2608, 2020.

[40] Y. Fang, L. Duan, Z. Han, Y. Zhao, and H. Yang, “Numerical analysis of aerodynamic performance of a floating offshore wind turbine under pitch motion,” *Energy*, vol. 192, p. 116621, 2020.

[41] R. Bezzina, T. Sant, and D. Micallef, “Modelling the aerodynamics of a floating wind turbine model using a cfd-based actuator disc method,” in *International Conference on Offshore Mechanics and Arctic Engineering*, vol. 59353. American Society of Mechanical Engineers, 2019, p. V001T01A003.

[42] T. Sant and D. Micallef, “Disparity analysis for three floating wind turbine aerodynamic codes in comparison,” in *International Conference on Offshore Mechanics and Arctic Engineering*, vol. 59353. American Society of Mechanical Engineers, 2019, p. V001T01A001.

[43] B. Wen, Q. Zhang, S. Wei, X. Tian, X. Dong, and Z. Peng, “Comparisons between the typical wind shear and the wind shear induced by platform pitch motion for an offshore floating wind turbine,” in *International Conference on Offshore Mechanics and Arctic Engineering*, vol. 51319. American Society of Mechanical Engineers, 2018, p. V010T09A059.

[44] L. Lin, K. Wang, and D. Vassalos, “Detecting wake performance of floating offshore wind turbine,” *Ocean Engineering*, vol. 156, pp. 263–276, 2018.

[45] T. T. Tran and D.-H. Kim, “A cfd study into the influence of unsteady aerodynamic interference on wind turbine surge motion,” *Renewable Energy*, vol. 90, pp. 204–228, 2016.

[46] R. Farrugia, T. Sant, and D. Micallef, “A study on the aerodynamics of a floating wind turbine rotor,” *Renewable energy*, vol. 86, pp. 770–784, 2016.

[47] F. S. Stoddard, “Momentum theory and flow states for windmills,” *Wind Technology Journal*, vol. 1, pp. 3–9, 1978.

[48] H. Glauert, “Airplane propellers,” in *Aerodynamic theory*. Springer, 1935, pp. 169–360.

[49] D. M. Pitt and D. A. Peters, “Theoretical prediction of dynamic-inflow derivatives,” 1980.

[50] H. Glauert, “A general theory of the autogyro,” HM Stationery Office, Tech. Rep., 1926.

[51] S. Øye, “Induced velocities for rotors in yaw,” in *Proceedings of the Sixth IEA Symposium*. Energy Research Centre of the Netherlands Petten, 1992, pp. 1–5.

[52] R. P. Coleman, A. M. Feingold, and C. W. Stempin, “Evaluation of the induced-velocity field of an idealized helicoptor rotor,” NATIONAL AERONAUTICS AND SPACE ADMINISTRATION HAMPTON VA LANGLEY RESEARCH CENTER, Tech. Rep., 1945.

[53] J. Schepers, “An engineering model for yawed conditions, developed on basis of wind tunnel measurements,” in *37th Aerospace Sciences Meeting and Exhibit*, 1999, p. 39.

[54] H. Glauert, *The analysis of experimental results in the windmill brake and vortex ring states of an airscrew*. HM Stationery Office, 1926.

[55] L. Prandtl and A. Betz, *Vier Abhandlungen zur Hydrodynamik und Aerodynamik*. Universitätsverlag Göttingen, 2010, vol. 3.

[56] M. L. Buhl Jr, “New empirical relationship between thrust coefficient and induction factor for the turbulent windmill state,” National Renewable Energy Lab.(NREL), Golden, CO (United States), Tech. Rep., 2005.

[57] H. Snel and J. Schepers, *Investigation and modelling of dynamic inflow effects*. Netherlands Energy Research Foundation ECN, 1993.

[58] S. Øye, "Unsteady wake effects caused by pitch–angle changes," in *IEA R&D WECS Joint Action on Aerodynamics of Wind Turbines, 1st Symposium*, 1986, pp. 58–79.

[59] S. Ø ye, "A simple vortex model of a turbine rotor," 1990.

[60] H. Snel and J. Schepers, "Joint investigation of dynamic inflow effects and implementation of an engineering method," 1995.

[61] M. Campobasso, M. Yan, J. Drofelnik, A. Piskopakis, and M. Caboni, "Compressible reynolds-averaged navier-stokes analysis of wind turbine turbulent flows using a fully-coupled low-speed preconditioned multigrid solver," in *Turbo Expo: Power for Land, Sea, and Air*, vol. 45660. American Society of Mechanical Engineers, 2014, p. V03BT46A010.

[62] N. Troldborg, F. Zahle, P.-E. Réthoré, and N. Sorensen, "Comparison of the wake of different types of wind turbine cfd models," in *50th AIAA Aerospace Sciences Meeting including the New Horizons Forum and Aerospace Exposition*, 2012, p. 237.

[63] J. N. Sørensen and C. W. Kock, "A model for unsteady rotor aerodynamics," *Journal of wind engineering and industrial aerodynamics*, vol. 58, no. 3, pp. 259–275, 1995.

[64] J. Sørensen, W. Shen, and X. Munduate, "Analysis of wake states by a full-field actuator disc model," *Wind Energy: An International Journal for Progress and Applications in Wind Power Conversion Technology*, vol. 1, no. 2, pp. 73–88, 1998.

[65] N. Troldborg, "Actuator line modeling of wind turbine wakes," 2009.

[66] J. N. Sorensen and W. Z. Shen, "Numerical modeling of wind turbine wakes," *J. Fluids Eng.*, vol. 124, no. 2, pp. 393–399, 2002.

[67] R. Mikkelsen *et al.*, "Actuator disc methods applied to wind turbines," Ph.D. dissertation, PhD thesis, Technical University of Denmark, 2003.

[68] R. F. Mikkelsen, J. N. Sørensen, and N. Troldborg, "Prescribed wind shear modelling with the actuator line technique," in *2007 European Wind Energy Conference and Exhibition*, 2007.

[69] R. Mikkelsen, J. N. Sørensen, S. Øye, and N. Troldborg, "Analysis of power enhancement for a row of wind turbines using the actuator line technique," in *Journal of Physics: Conference Series*, vol. 75, no. 1. IOP Publishing, 2007, p. 012044.

[70] S. Ivanell, J. N. Sørensen, R. Mikkelsen, and D. Henningson, "Numerical analysis of the tip and root vortex position in the wake of a wind turbine," in *Journal of Physics: Conference Series*, vol. 75, no. 1. IOP Publishing, 2007, p. 012035.

[71] F. Zahle, "Wind turbine aerodynamics using an incompressible overset grid method," 2006.

[72] G. Tampier, C. Troncoso, and F. Zilic, "Numerical analysis of a diffuser-augmented hydrokinetic turbine," *Ocean engineering*, vol. 145, pp. 138–147, 2017.

[73] C. G. Speziale, "Turbulence modeling for time-dependent rans and vles: a review," *AIAA journal*, vol. 36, no. 2, pp. 173–184, 1998.

[74] C. Laborde-Boutet, F. Larachi, N. Dromard, O. Delsart, and D. Schweich, "Cfd simulation of bubble column flows: Investigations on turbulence models in rans approach," *Chemical Engineering Science*, vol. 64, no. 21, pp. 4399–4413, 2009.

[75] C. Yin, J. Wu, and D. Wan, "Model and full scale vlcc resistance prediction and flow field analysis based on iddes method," in *The 26th International Ocean and Polar Engineering Conference*. OnePetro, 2016.

[76] P. Spalart, “Comments on the feasibility of les for wings, and on hybrid rans/les approach, advances in dns/les,” in *Proceedings of 1st AFOSR International Conference on DNS/LES, 1997*, 1997.

[77] P. R. Spalart, S. Deck, M. L. Shur, K. D. Squires, M. K. Strelets, and A. Travin, “A new version of detached-eddy simulation, resistant to ambiguous grid densities,” *Theoretical and computational fluid dynamics*, vol. 20, no. 3, pp. 181–195, 2006.

[78] A. K. Travin, M. L. Shur, P. R. Spalart, and M. K. Strelets, “Improvement of delayed detached-eddy simulation for les with wall modelling,” 2006.

[79] W. Riéra, L. Castillon, J. Marty, and F. Leboeuf, “Inlet condition effects on the tip clearance flow with zonal detached eddy simulation,” in *Turbo Expo: Power for Land, Sea, and Air*, vol. 55249. American Society of Mechanical Engineers, 2013, p. V06CT42A003.

[80] H. Hu, M. Khosravi, and P. Sarkar, “An experimental investigation on the aeromechanic performance and wake characteristics of a wind turbine model subjected to pitch motions,” in *34th Wind Energy Symposium*, 2016, p. 1997.

[81] S. Rockel, E. Camp, J. Schmidt, J. Peinke, R. B. Cal, and M. Hölling, “Experimental study on influence of pitch motion on the wake of a floating wind turbine model,” *Energies*, vol. 7, no. 4, pp. 1954–1985, 2014.

[82] I. Bayati, M. Belloli, L. Bernini, and A. Zasso, “Wind tunnel validation of aerodyn within lifes50+ project: imposed surge and pitch tests,” in *Journal of Physics: Conference Series*, vol. 753, no. 9. IOP Publishing, 2016, p. 092001.

[83] W. Lu, A. Robertson, J. Jonkman, Y.-H. Yu, A. Koop, A. B. Nadal, H. Li, E. E. Bachynski-Polic, R. Pinguet, W. Shi *et al.*, “Oc6 phase ib: Validation of the cfd predictions of difference-frequency wave excitation on a fowt semisubmersible,” 2021.

[84] X. Shen, J. Chen, P. Hu, X. Zhu, and Z. Du, “Study of the unsteady aerodynamics of floating wind turbines,” *Energy*, vol. 145, pp. 793–809, 2018.

[85] T.-T. Tran and D.-H. Kim, “The platform pitching motion of floating offshore wind turbine: A preliminary unsteady aerodynamic analysis,” *Journal of Wind Engineering and Industrial Aerodynamics*, vol. 142, pp. 65–81, 2015.

[86] J. Jonkman and M. Buhl, “Development and verification of a fully coupled simulator for offshore wind turbines,” in *45th AIAA Aerospace Sciences Meeting and Exhibit*, 2007, p. 212.

[87] H. Johlas, L. Martínez-Tossas, M. Lackner, D. Schmidt, and M. Churchfield, “Large eddy simulations of offshore wind turbine wakes for two floating platform types,” in *Journal of Physics: Conference Series*, vol. 1452, no. 1. IOP Publishing, 2020, p. 012034.

[88] M. Karimirad, “Modeling aspects of a floating wind turbine for coupled wave–wind-induced dynamic analyses,” *Renewable Energy*, vol. 53, pp. 299–305, 2013.

[89] T. J. Larsen and A. M. Hansen, “How 2 hawc2, the user’s manual,” *target*, vol. 2, no. 2, 2007.

[90] J. M. Jonkman, A. Robertson, and G. J. Hayman, “Hydrodyn user’s guide and theory manual,” *National Renewable Energy Laboratory*, 2014.

[91] T. Sebastian and M. Lackner, “Analysis of the induction and wake evolution of an offshore floating wind turbine,” *Energies*, vol. 5, no. 4, pp. 968–1000, 2012.

[92] H. Jasak, A. Jemcov, Z. Tukovic *et al.*, “Openfoam: A c++ library for complex physics simulations,” in *International workshop on coupled methods in numerical dynamics*, vol. 1000. IUC Dubrovnik Croatia, 2007, pp. 1–20.

[93] J. M. Jonkman, G. Hayman, B. Jonkman, R. Damiani, and R. Murray, “Aerodyn v15 user’s guide and theory manual,” *NREL Draft Report*, 2015.

[94] D. Apsley and P. Stansby, “Unsteady thrust on an oscillating wind turbine: comparison of blade-element momentum theory with actuator-line cfd,” *Journal of Fluids and Structures*, vol. 98, p. 103141, 2020.

[95] M. Hamlaoui, A. Smaili, I. Dobrev, M. Pereira, H. Fellouah, and S. Khelladi, “Numerical and experimental investigations of hawt near wake predictions using particle image velocimetry and actuator disk method,” *Energy*, vol. 238, p. 121660, 2022.

[96] P. R. Spalart and C. L. Rumsey, “Effective inflow conditions for turbulence models in aerodynamic calculations,” *AIAA journal*, vol. 45, no. 10, pp. 2544–2553, 2007.

[97] [Online]. Available: https://gmsh.info/

[98] “Description.” [Online]. Available: https://www.openfoam.com/documentation/guides/latest/man/createBaffles.html

[99] M. O. HANSEN, *Aerodynamics of wind turbines*. Earthscan, 2008.

[100] A. Rajan and F. L. Ponta, “A novel correlation model for horizontal axis wind turbines operating at high-interference flow regimes,” *Energies*, vol. 12, no. 6, p. 1148, 2019.

[101] Á. Jiménez, A. Crespo, and E. Migoya, “Application of a les technique to characterize the wake deflection of a wind turbine in yaw,” *Wind energy*, vol. 13, no. 6, pp. 559–572, 2010.

[102] N. Troldborg, M. Gaunaa, and S. Guntur, “Modelling the influence of yaw using a simple vortex rotor model,” *EWEC, Copenhagen*, pp. 1–5, 2012.

[103] F. White and B. B. Blake, “Improved method predicting helicopter control response and gust sensitivity.” American Helicopter Society, 1979.

listings color

frame=tb, language=Java, aboveskip=3mm, belowskip=3mm, showstringspaces=false, columns=flexible, basicstyle=, numbers=none, numberstyle=, keywordstyle=, commentstyle=, stringstyle=, breaklines=true, breakatwhitespace=true, tabsize=3

A
The discarded model

Initially, it was planned to develop a fully orthogonal mesh and introduce the movement of actuation disk by modifying the OpenFOAM library **actuationDiskSource**. However, this was not fully suitable because there were very small discontinuities observed on the actuator disk which led to extra and unwanted flow seepage through the actuator disk.

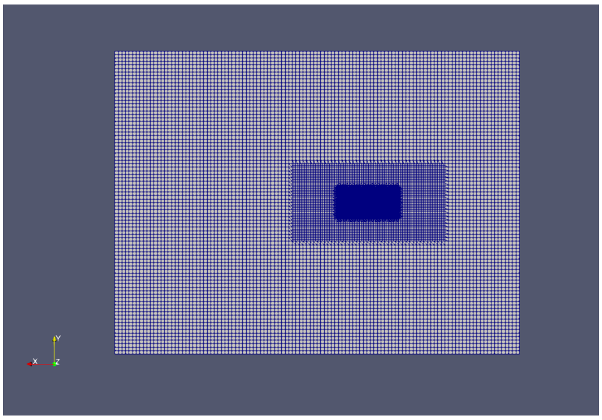

Figure A.1: Orthogonal mesh grid created initially

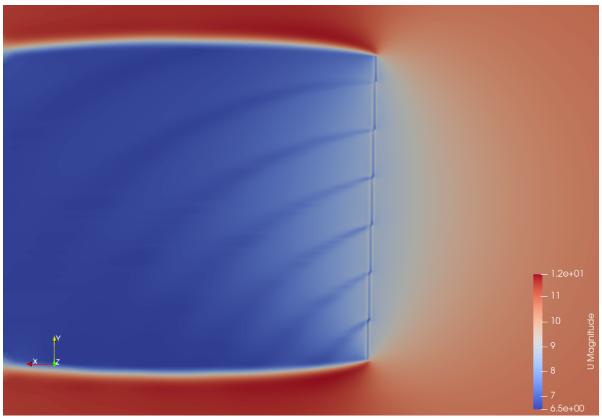

Figure A.2: Visualization of U_x contour on a pitching actuator disk

As it can be observed in Figure A.1, the mesh created was fully orthogonal, and only additional refinement regions were added near the actuator disk region to improve resolution. Since the cells were fully orthogonal, when the actuator disk pitched or even if yawed, the cell selection using **topoSet** utility was not continuous. Since the **topoSet** utility selects the cells which have their centres within the specified area, whenever cells from different columns were selected, the region between these two columns of cells does not impart any momentum to the flow and leads to a flow discontinuity. This is the exact same phenomenon that is observed in Figure A.2. Since the actuator disk is slightly inclined with the Y axis, topoSet utility is unable to select a single row of cells and rather selects bunches of cells from different cell columns. The curved streaks downstream of the actuator disk are the effect of the discontinuous selection of actuation cells.

B

Calibration of post-processing code

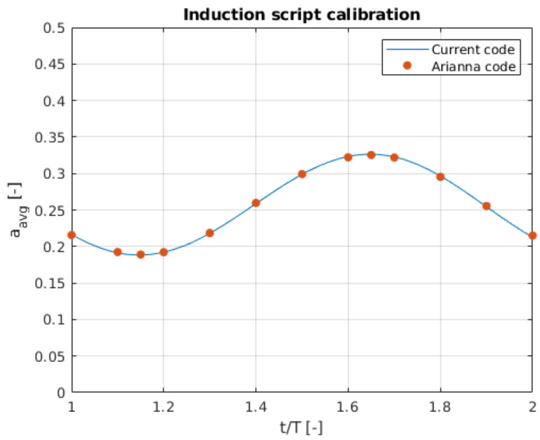

Figure B.1: Comparison between results predicted by the current code and reference results from [2]

Case compared - Ct = 0.8; delCt = 0.5; freq = 8.75Hz; static AD.

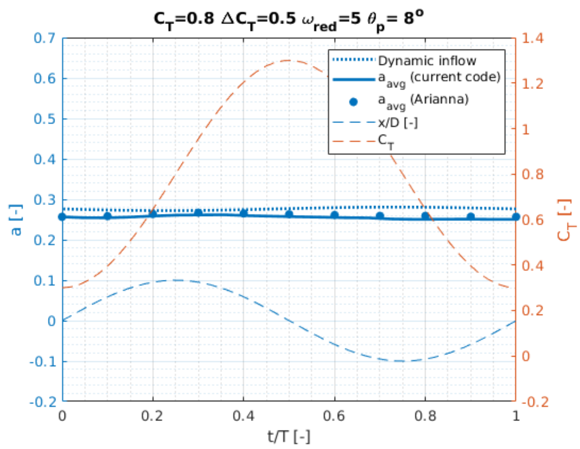

Figure B.2: Comparison between results predicted by the current code and reference results from [2]

Case compared - Ct = 0.8; delCt = 0.5; freq = 8.75Hz; dynamic surging AD.

In order to make a proper comparison between the actuator disk surging case and the pitching case, the post-processing code needs to be calibrated to reproduce the same results produced by the surging case. The codes used to calculate the inductions are highly sensitive to the extent to which the interpolation is done. Therefore, to conduct an accurate and representative study, the calibration of codes is necessary.

In order to achieve that, a case from [2] is re-run by the author and is post-processed using the previous iteration of the code. Since the values of induction factors produced are highly sensitive to the extent of interpolation, this length was iteratively changed to obtain the results that match with the induction field predicted by Sala[2] in her thesis report.

C

Why the rotor-averaged induction (a_{avg}) calculation method needs to be modified?

The method used for calculating the rotor averaged induction considers only the region corresponding to $\phi = 0^o$ and extrapolates the same induction values to the regions corresponding to all the other azimuths ($\phi \neq 0^o$). This method works perfectly for a non-tilted actuator disk where the induction field is just a function of radial position. That is, in a non-tilted actuator, the induction factor corresponding to $\phi = 0^o$ is equal to $\phi \neq 0^o$.

However, in the case of a tilted actuator disk, the induction field varies with both the radial position and the azimuthal position. The effect of tilt gradually decreases as the azimuthal position goes down from $\phi = 0^o$ to $\phi = 90^o$. Therefore, extrapolation in the case of a tilted actuator disk will lead to over-prediction of the effects of tilt/yaw. This rudimentary mistake did not cross the author's attention until the project neared its conclusion. Due to time constraints, it was too late to rectify the problem and modify the results accordingly. Therefore, in this section, a comparative analysis of the proper method of average induction calculation and the method used in this project is provided. In the proper method, the rotor-averaged induction is calculated by considering the velocities corresponding to the whole actuator disk. This method does not extrapolate data but rather directly reads the data from CFD results.

Table C.1 provides the values of a_{avg} calculated using the proper (new) method and calculated using the original method (used in this thesis) for actuator disks in steady yaw. The difference, even though is not significant enough to show unphysical results, it is still there. The discrepancies in the case of the pitching actuator disk can be expected to be much higher effects because of the presence of a strong vortex that is purely a result of the dynamic tilting. Therefore, it is highly recommended to use the new method for future calculations.

Table C.1: Values of a_{avg} calculated using the proper (new) method and the original method

Yaw angle	Proper method	Used method	Error (%)
-10	0.2639	0.2685	1.7132
-5	0.2694	0.2713	0.7003

D
Mesh deformation and its effects

It should be noted that the unphysical trend observed in the contour plots enclosed by the red box in Figure D.1 is purely numerical and should be disregarded. Since the computational domain employs an interface mesh, there is a layer of cells that undergo deformation when the master domain undergoes oscillatory rotation (pitching motion). Figure D.2 attempts to show the layer of cells that undergo deformation in the computational domain. Since these cells will have the maximum deformation when the actuator disk is at the extremities ($t/T = 0.25$ and $t/T = 0.75$), contour plots corresponding to these two time steps will possess this unphysical behavior which can be disregarded.

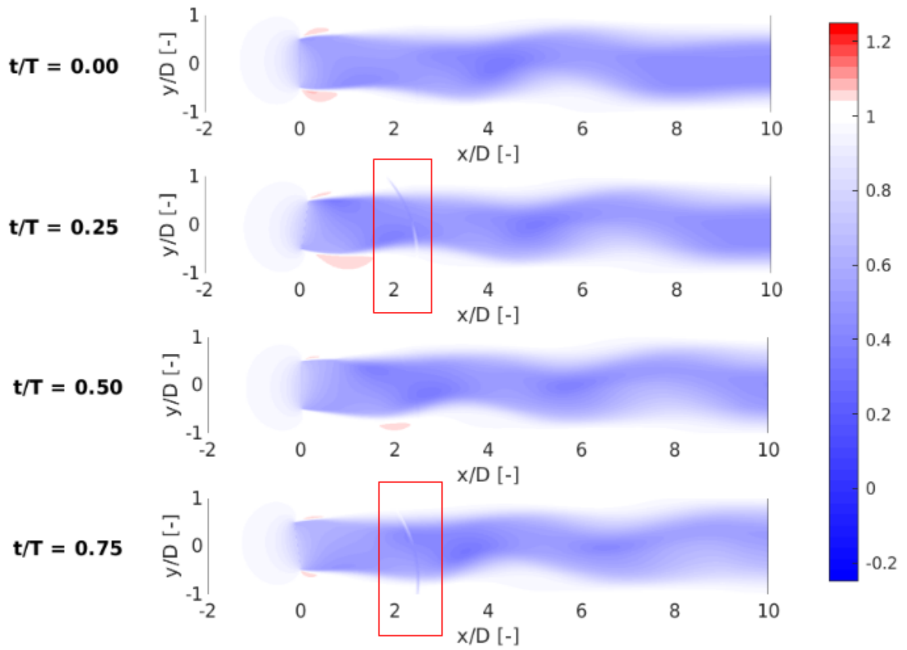

Figure D.1: Contour of U_x to show the unphysical behaviour

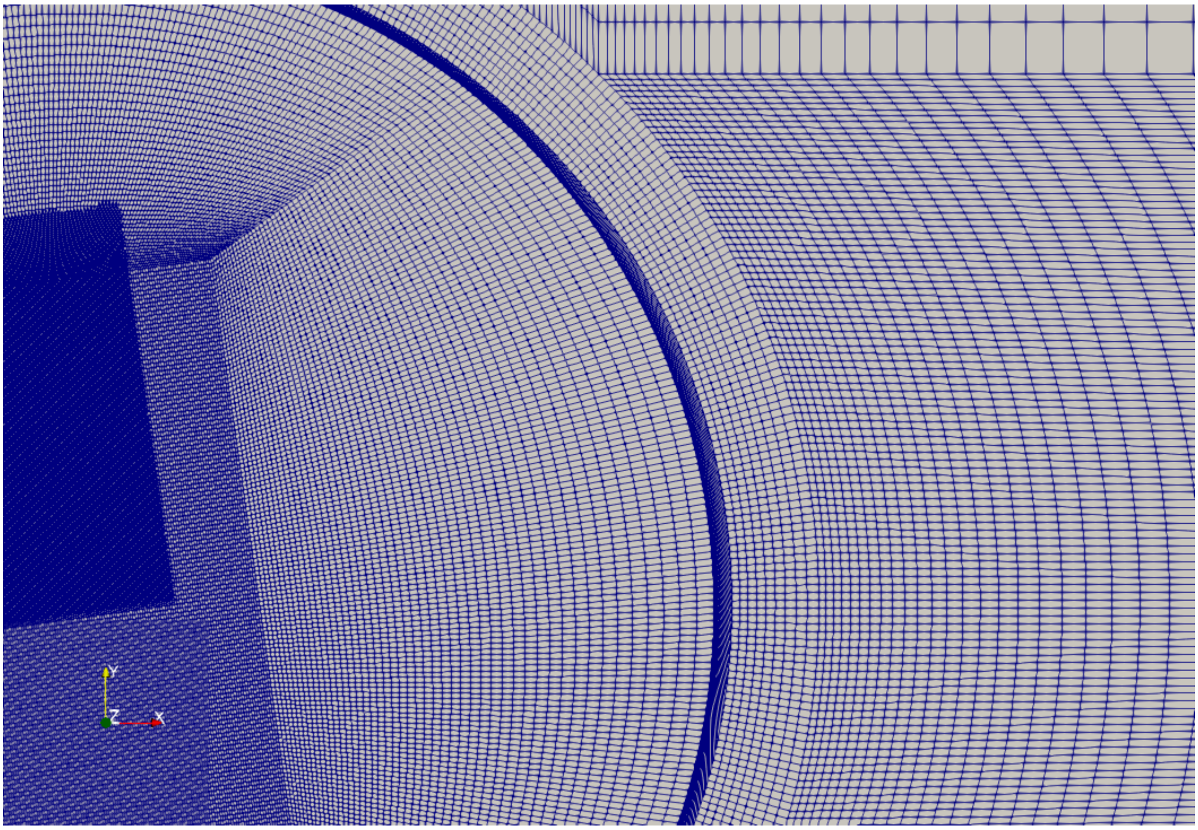

Figure D.2: Visualisation of the computational grid with highly deformed cells at the interface

E

Modified actuator disk library

```
/*---------------------------------------------------------------------------*\
  =========                 |
  \\      /  F ield         | OpenFOAM: The Open Source CFD Toolbox
   \\    /   O peration     |
    \\  /    A nd           | www.openfoam.com
     \\/     M anipulation  |
-------------------------------------------------------------------------------
    Copyright (C) 2011-2016 OpenFOAM Foundation
    Copyright (C) 2020 ENERCON GmbH
    Copyright (C) 2018-2020 OpenCFD Ltd
-------------------------------------------------------------------------------
License
    This file is part of OpenFOAM.

    OpenFOAM is free software: you can redistribute it and/or modify it
    under the terms of the GNU General Public License as published by
    the Free Software Foundation, either version 3 of the License, or
    (at your option) any later version.

    OpenFOAM is distributed in the hope that it will be useful, but WITHOUT
    ANY WARRANTY; without even the implied warranty of MERCHANTABILITY or
    FITNESS FOR A PARTICULAR PURPOSE.  See the GNU General Public License
    for more details.

    You should have received a copy of the GNU General Public License
    along with OpenFOAM.  If not, see <http://www.gnu.org/licenses/>.

\*---------------------------------------------------------------------------*/

#include "unsteadyCT_temp.H"
#include "fvMesh.H"
#include "fvMatrix.H"
#include "volFields.H"
#include "mathematicalConstants.H"

// * * * * * * * * * * * * * Private Member Functions  * * * * * * * * * * * //

template<class AlphaFieldType, class RhoFieldType>
void Foam::fv::unsteadyCT_temp::calc
```

```
(
    const AlphaFieldType& alpha,
    const RhoFieldType& rho,
    fvMatrix<vector>& eqn
)
{
    switch (forceMethod_)
    {
        case forceMethodType::FROUDE:
        {
            calcFroudeMethod(alpha, rho, eqn);
            break;
        }

        case forceMethodType::VARIABLE_SCALING:
        {
            calcVariableScalingMethod(alpha, rho, eqn);
            break;
        }

        default:
            break;
    }
}


template<class AlphaFieldType, class RhoFieldType>
void Foam::fv::unsteadyCT_temp::calcFroudeMethod
(
    const AlphaFieldType& alpha,
    const RhoFieldType& rho,
    fvMatrix<vector>& eqn
)
{
    const vectorField& U = eqn.psi();
    vectorField& Usource = eqn.source();
    const scalarField& cellsV = mesh_.V();

    // Compute upstream U and rho, spatial-averaged over monitor-region
    /*vector Uref(Zero);
    scalar rhoRef = 0.0;
    label szMonitorCells = monitorCells_.size();

    for (const auto& celli : monitorCells_)
    {
        Uref += U[celli];
        rhoRef = rhoRef + rho[celli];
    }
    reduce(Uref, sumOp<vector>());
    reduce(rhoRef, sumOp<scalar>());
    reduce(szMonitorCells, sumOp<label>());

    if (szMonitorCells == 0)
    {
        FatalErrorInFunction
            << "No cell is available for incoming velocity monitoring."
```

```
            << exit(FatalError);
    }

    Uref /= szMonitorCells;
    rhoRef /= szMonitorCells;

    const scalar Ct = sink_*UvsCtPtr_->value(mag(Uref));
    const scalar Cp = sink_*UvsCpPtr_->value(mag(Uref));

    if (Cp <= VSMALL || Ct <= VSMALL)
    {
        FatalErrorInFunction
           << "Cp and Ct must be greater than zero." << nl
           << "Cp = " << Cp << ", Ct = " << Ct
           << exit(FatalIOError);
    }

    // (BJSB:Eq. 3.9)
    const scalar a = 1.0 - Cp/Ct;
    const scalar T = 2.0*rhoRef*diskArea_*magSqr(Uref & diskDir_)*a*(1 - a);

    for (const label celli : cells_)
    {
        Usource[celli] += ((cellsV[celli]/V())*T)*diskDir_;
    }

    if
    (
        mesh_.time().timeOutputValue() >= writeFileStart_
     && mesh_.time().timeOutputValue() <= writeFileEnd_
    )
    {
        Ostream& os = file();
        writeCurrentTime(os);

        //os  << Uref << tab << Cp << tab << Ct << tab << a << tab << T << tab
            //<< endl;

          os  << Uref << tab << Ct << tab << x1 << tab << x2
            << tab << T <<
            endl;
    }*/
}


template<class AlphaFieldType, class RhoFieldType>
void Foam::fv::unsteadyCT_temp::calcVariableScalingMethod
(
    const AlphaFieldType& alpha,
    const RhoFieldType& rho,
    fvMatrix<vector>& eqn
)
{
    const vectorField& U = eqn.psi();
    vectorField& Usource = eqn.source();
    const scalarField& cellsV = mesh_.V();
```

```
    // Monitor and average monitor-region U and rho
    vector Uref(Zero);
    scalar rhoRef = 0.0;
    label szMonitorCells = monitorCells_.size();

    //for (const auto& celli : monitorCells_) // commented by Sudharsan
    //{
        //Uref += U[celli]; //commented by Sudharsan
        //rhoRef = rhoRef + rho[celli]; //commented by Sudharsan

    //}
    //reduce(Uref, sumOp<vector>()); //commented by Sudharsan
    //reduce(rhoRef, sumOp<scalar>()); //commented by Sudharsan
    //reduce(szMonitorCells, sumOp<label>()); //commented by Sudharsan


    /*if (szMonitorCells == 0) //Added by Sudharsan
    {
        FatalErrorInFunction
            << "No cell is available for incoming velocity monitoring."
            << exit(FatalError);
    }*/

   //Uref /= szMonitorCells; //commented by Sudharsan
    Uref = Umon_;
    const scalar magUref = mag(Uref);
    //rhoRef /= szMonitorCells; commented by Sudharsan
rhoRef= rhomon_;


    // Monitor and average U and rho on actuator disk
    vector Udisk(Zero);
    scalar rhoDisk = 0.0;
    scalar totalV = 0.0;

    // for (const auto& celli : cells_)

    const pointField& ctrs = mesh_.cellCentres(); //added by Sudharsan. From cylinderToCell.C
    scalar t = mesh_.time().value(); //added by Sudharsan. From turbinesFoam/actuatorLineSource.C
    /*const scalar t =    //Added by Sudharsan. From writeFile.C
     (
         useUserTime_
       ? fileObr_.time().timeOutputValue()
       : fileObr_.time().value()
     );*/


    Info << "t:" << t << endl;

    for (const auto& celli : cells_)
    {

Udisk += U[celli]*cellsV[celli];
rhoDisk += rho[celli]*cellsV[celli];
        totalV += cellsV[celli];
```

```
 }


  reduce(Udisk, sumOp<vector>());
  reduce(rhoDisk, sumOp<scalar>());
  reduce(totalV, sumOp<scalar>());

  if (totalV < 0)
  {
      FatalErrorInFunction
          << "No cell in the actuator disk."
          << exit(FatalError);
  }

  Udisk /= totalV;
  const scalar magUdisk = mag(Udisk);
  rhoDisk /= totalV;

  if (mag(Udisk) < SMALL)
  {
      FatalErrorInFunction
          << "Velocity spatial-averaged on actuator disk is zero." << nl
          << "Please check if the initial U field is zero."
          << exit(FatalError);
  }

  // Interpolated thrust/power coeffs from power/thrust curves
  //const scalar Ct = sink_*UvsCtPtr_->value(magUref);


  // Modifications added by Sudharsan


const scalar Ct = sink_*(UvsCtPtr_->value(magUref) - ...
delta_Ct_*cos(constant::mathematical::twoPi*frequency_Ct_*t + phase_Ct_));
scalar theta_p = Amp_p_ * sin(constant::mathematical::twoPi*freq_p_*t);
// angles calculated in radians
vector diskDir_(cos(theta_p), -sin(theta_p), 0);

  Info << "Ct:" << Ct << endl;
  Info << "Disk_dir:" << diskDir_ << endl;

  const scalar Cp = sink_*UvsCpPtr_->value(magUref);

  //if (Cp <= VSMALL || Ct <= VSMALL)
  //{
  //    FatalErrorInFunction
  //       << "Cp and Ct must be greater than zero." << nl
  //       << "Cp = " << Cp << ", Ct = " << Ct
  //       << exit(FatalIOError);
  //}

  // Calibrated thrust/power coeffs from power/thrust curves (LSRMTK:Eq. 6)
  const scalar CtStar = Ct*sqr(magUref/magUdisk);
  const scalar CpStar = Cp*pow3(magUref/magUdisk);
```

```
    // Compute calibrated thrust/power (LSRMTK:Eq. 5)
     //const scalar T = 0.5*rhoRef*diskArea_*magSqr(Udisk & diskDir_)*CtStar;
    //const scalar P = 0.5*rhoRef*diskArea_*pow3(mag(Udisk & diskDir_))*CpStar;


    const scalar T = 0.5*rhoRef*diskArea_*sqr(magUref)*Ct;
    const scalar P = 0.5*rhoRef*diskArea_*pow3(magUref)*Cp;

    //end of part modified by Sudharsan

    for (const label celli : cells_)
    {
        Usource[celli] += (cellsV[celli]/totalV*T)*diskDir_;
    }

    if
    (
        mesh_.time().timeOutputValue() >= writeFileStart_
     && mesh_.time().timeOutputValue() <= writeFileEnd_
    )
    {
        Ostream& os = file();
        writeCurrentTime(os);

    }
}
// ************************************************************************* //
```

F
Additional figures

F.1. Case 5

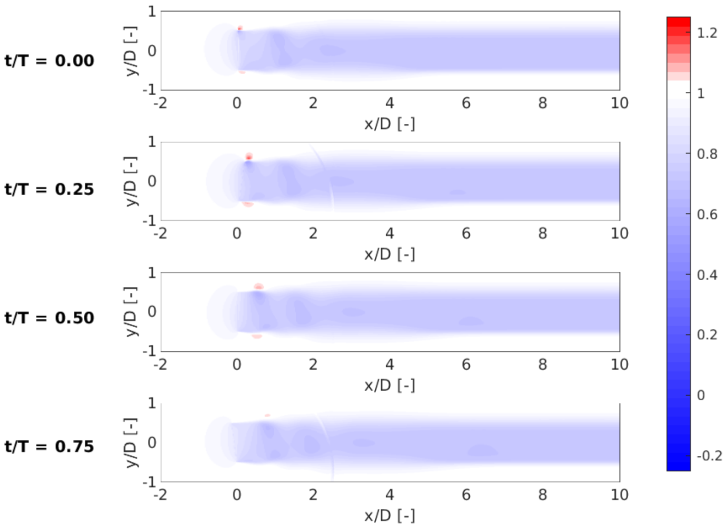

Figure F.1: Contour of normalized X velocity for Case5 - $C_T = 0.5$; $\Delta C_T = 0$; $\theta_p = 8^o$; $\omega_{red} = 5$

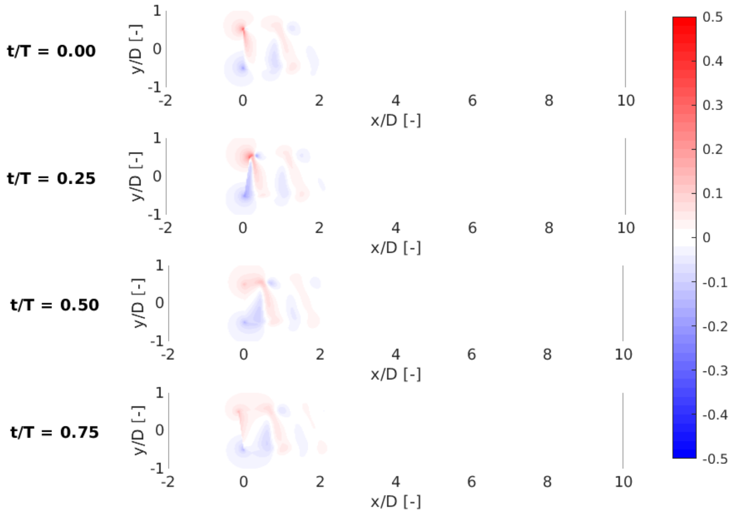

Figure F.2: Contour of normalized Y velocity for Case5 - $C_T = 0.5$; $\Delta C_T = 0$; $\theta_p = 8^o$; $\omega_{red} = 5$

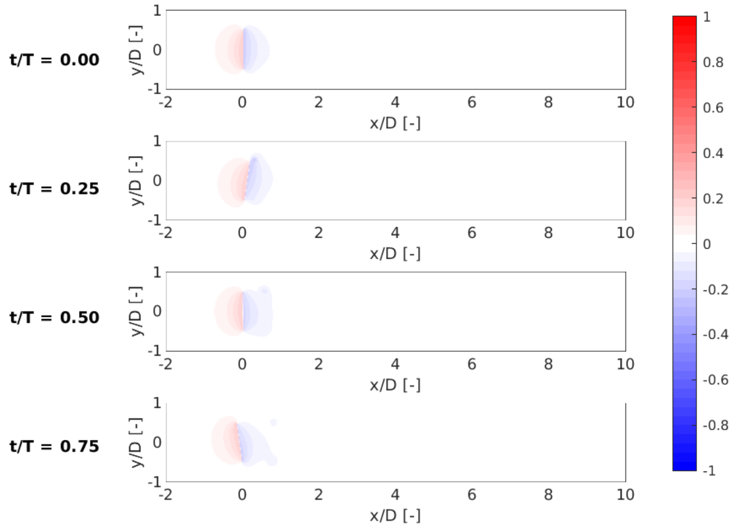

Figure F.3: Contour of normalized pressure for Case5 - $C_T = 0.5$; $\Delta C_T = 0$; $\theta_p = 8^o$; $\omega_{red} = 5$

F.2. Case 10

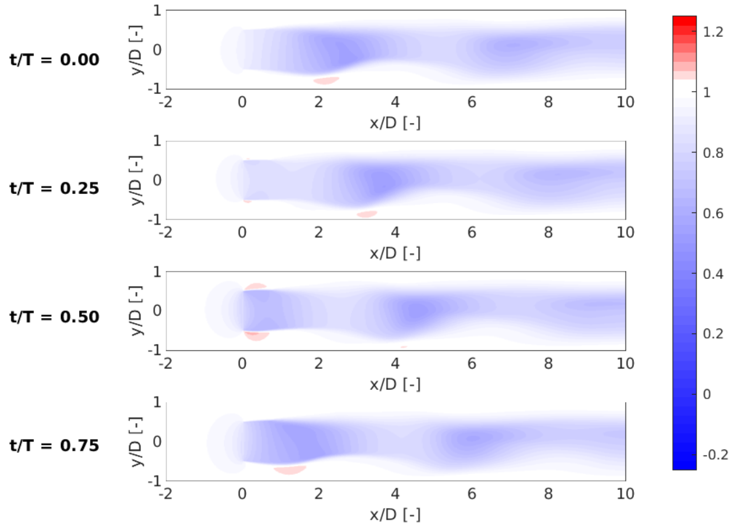

Figure F.4: Contour of normalized X velocity for Case10 - $C_T = 0.5$; $\Delta C_T = 0.3$; $\theta_p = 0^o$; $\omega_{red} = 1$

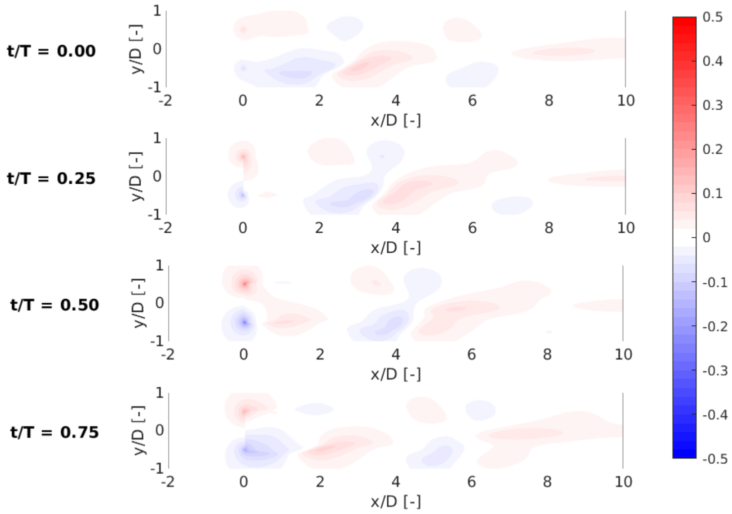

Figure F.5: Contour of normalized Y velocity for Case5 - $C_T = 0.5$; $\Delta C_T = 0.3$; $\theta_p = 0^o$; $\omega_{red} = 1$

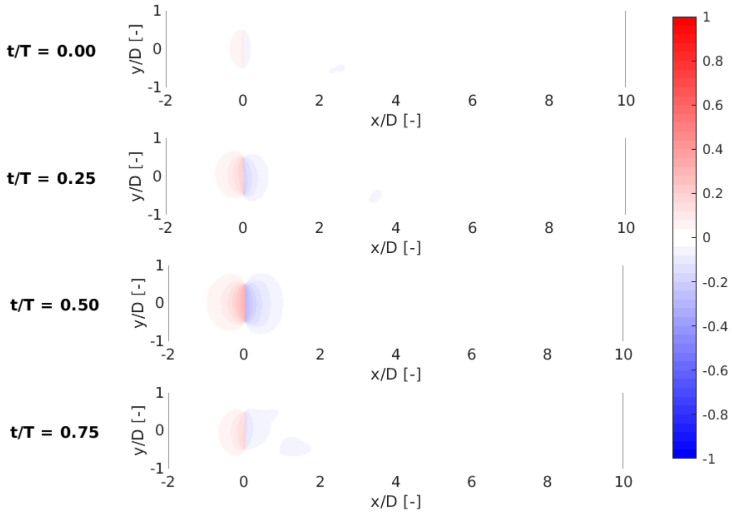

Figure F.6: Contour of normalized pressure for Case10 - $C_T = 0.5$; $\Delta C_T = 0.3$; $\theta_p = 0^o$; $\omega_{red} = 1$

F.3. Case 11

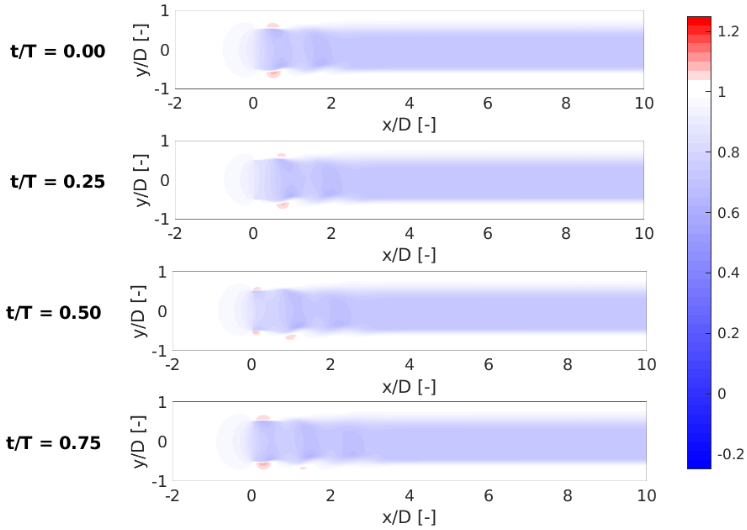

Figure F.7: Contour of normalized X velocity for Case11 - $C_T = 0.5$; $\Delta C_T = 0.3$; $\theta_p = 0^o$; $\omega_{red} = 5$

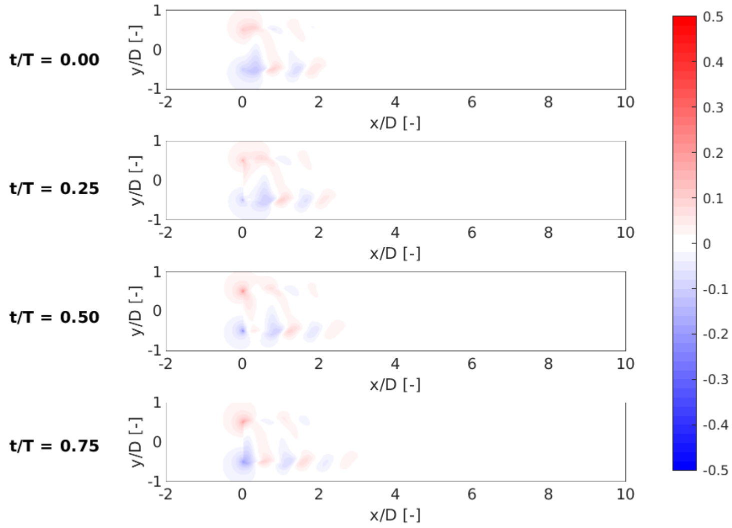

Figure F.8: Contour of normalized Y velocity for Case11 - $C_T = 0.5$; $\Delta C_T = 0.3$; $\theta_p = 0^o$; $\omega_{red} = 5$

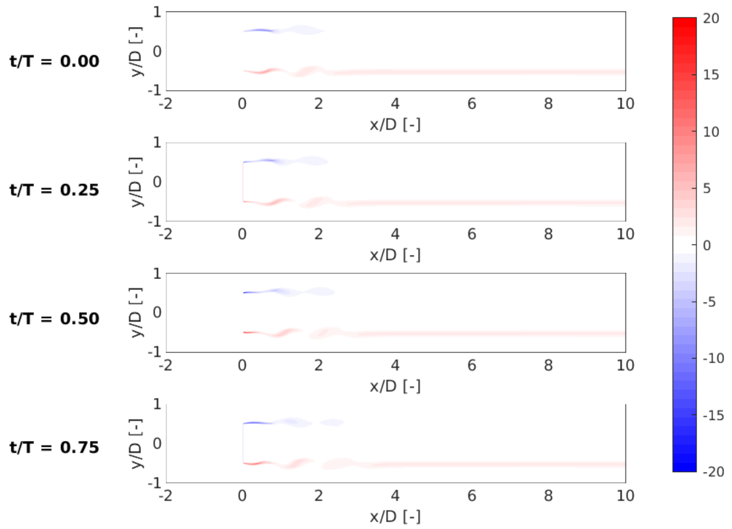

Figure F.9: Contour of normalized Z vorticity for Case11 - $C_T = 0.5$; $\Delta C_T = 0.3$; $\theta_p = 0^o$; $\omega_{red} = 5$

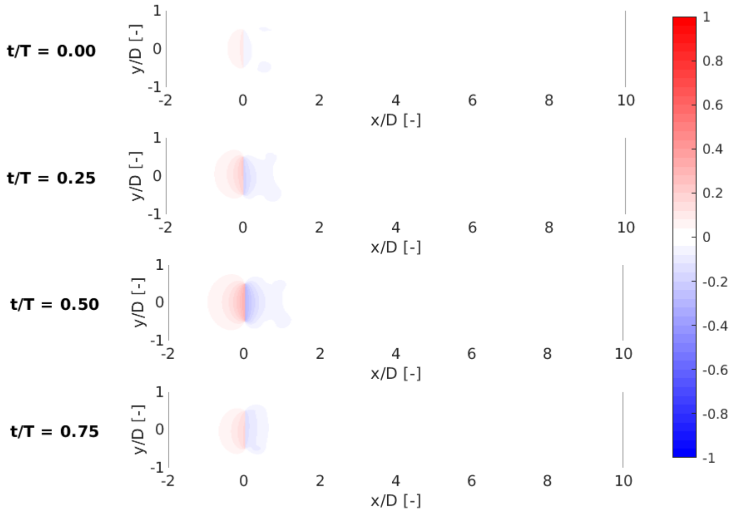

Figure F.10: Contour of normalized pressure for Case11 - $C_T = 0.5$; $\Delta C_T = 0.3$; $\theta_p = 0^o$; $\omega_{red} = 5$

F.4. Case 13

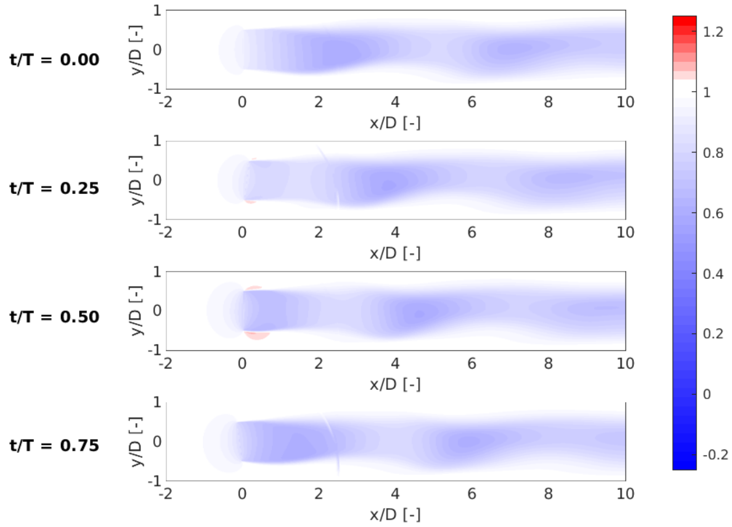

Figure F.11: Contour of normalized X velocity for Case13 - $C_T = 0.5$; $\Delta C_T = 0.3$; $\theta_p = 8^o$; $\omega_{red} = 1$

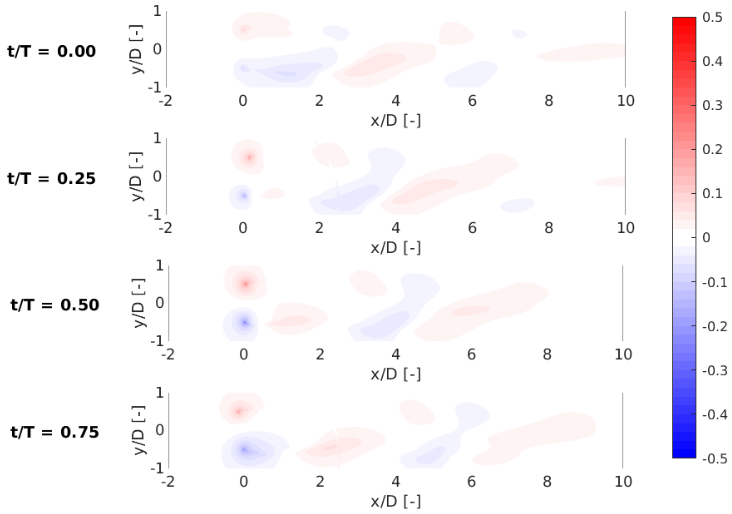

Figure F.12: Contour of normalized Y velocity for Case13 - $C_T = 0.5$; $\Delta C_T = 0.3$; $\theta_p = 8^o$; $\omega_{red} = 1$

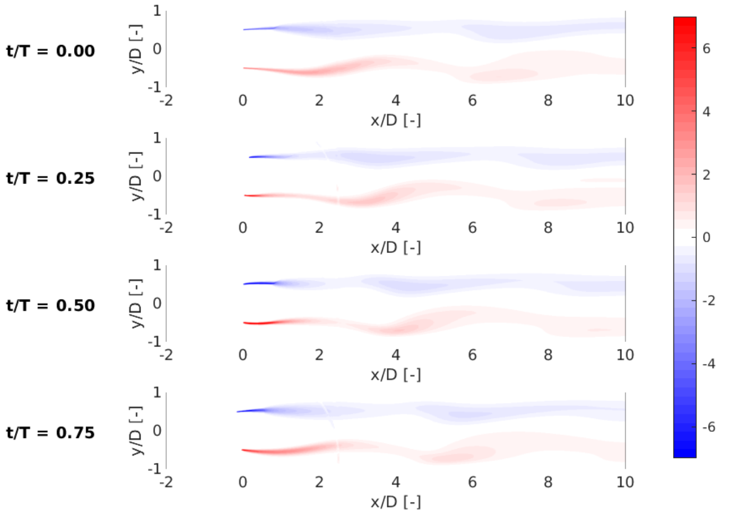

Figure F.13: Contour of normalized Y velocity for Case13 - $C_T = 0.5$; $\Delta C_T = 0.3$; $\theta_p = 8^o$; $\omega_{red} = 1$

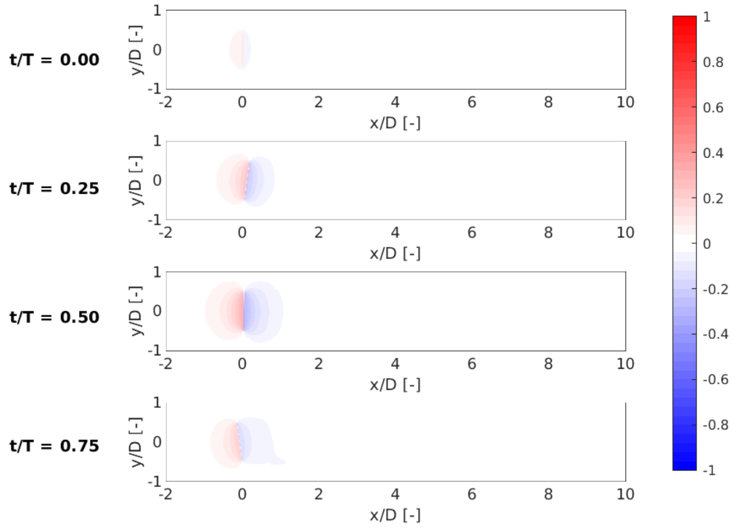

Figure F.14: Contour of normalized Y velocity for Case13 - $C_T = 0.5$; $\Delta C_T = 0.3$; $\theta_p = 8^o$; $\omega_{red} = 1$

F.5. Case 14

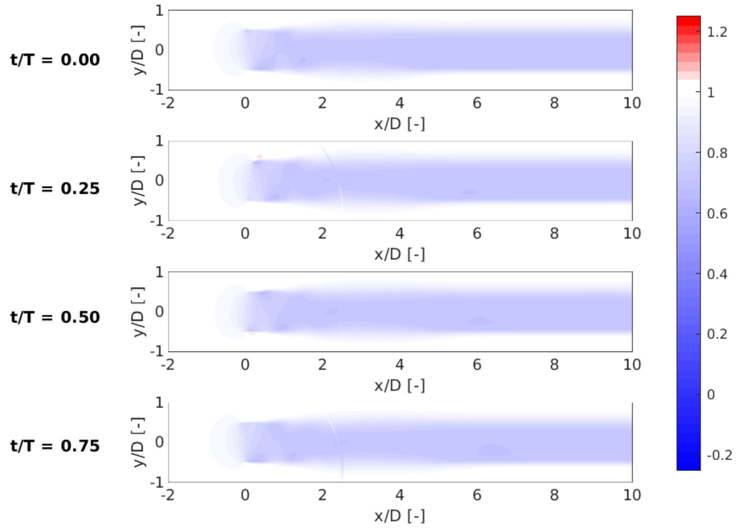

Figure F.15: Contour of normalized X velocity for Case14 - $C_T = 0.5$; $\Delta C_T = 0.3$; $\theta_p = 8^o$; $\omega_{red} = 5$

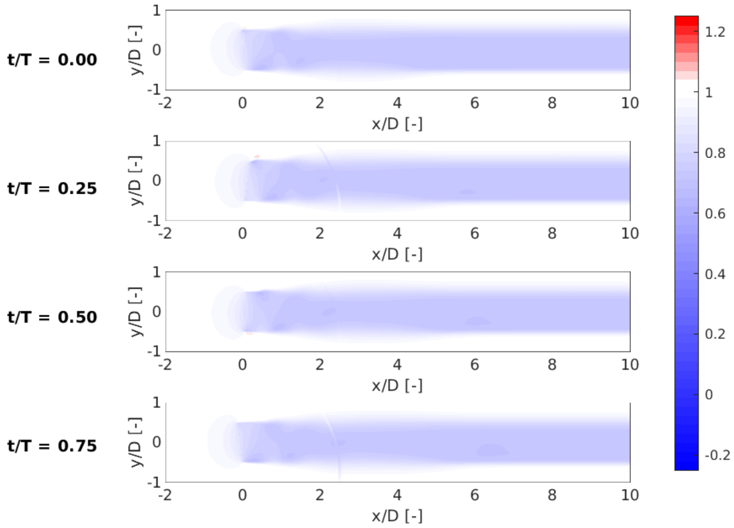

Figure F.16: Contour of normalized Y velocity for Case14 - $C_T = 0.5$; $\Delta C_T = 0.3$; $\theta_p = 8^o$; $\omega_{red} = 5$

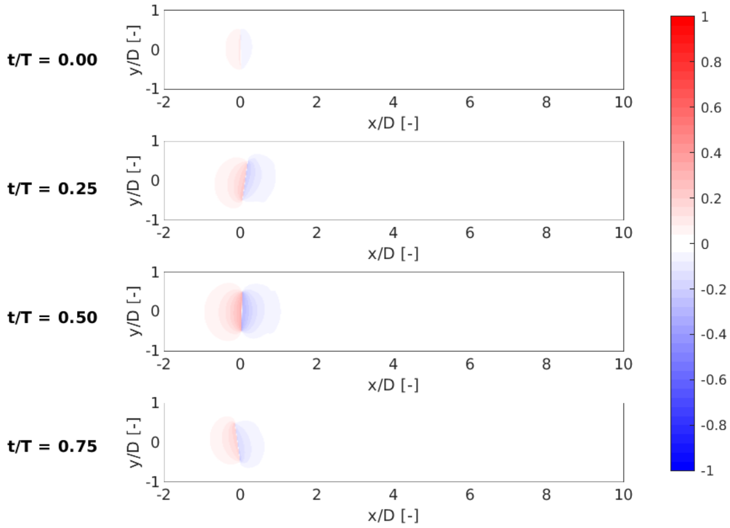

Figure F.17: Contour of normalized pressure for Case14 - $C_T = 0.5$; $\Delta C_T = 0.3$; $\theta_p = 8^o$; $\omega_{red} = 5$

F.6. Case 16

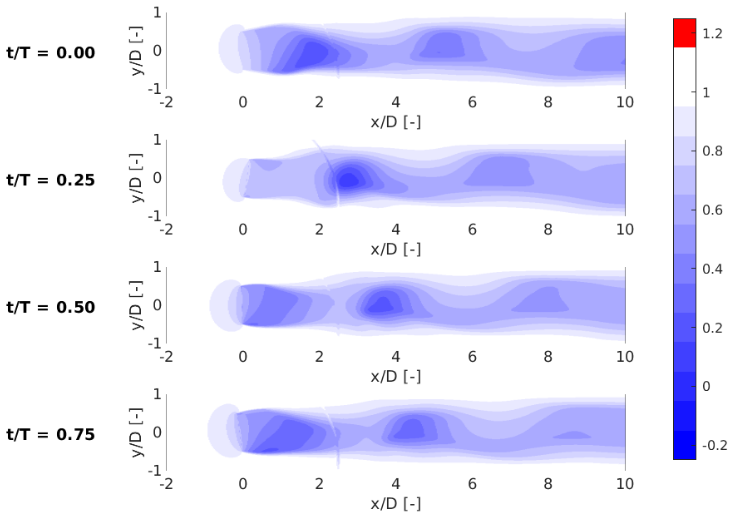

Figure F.18: Contour of normalized X velocity for Case16 - $C_T = 0.8$; $\Delta C_T = 0.5$; $\theta_p = 8^o$; $\omega_{red} = 1$

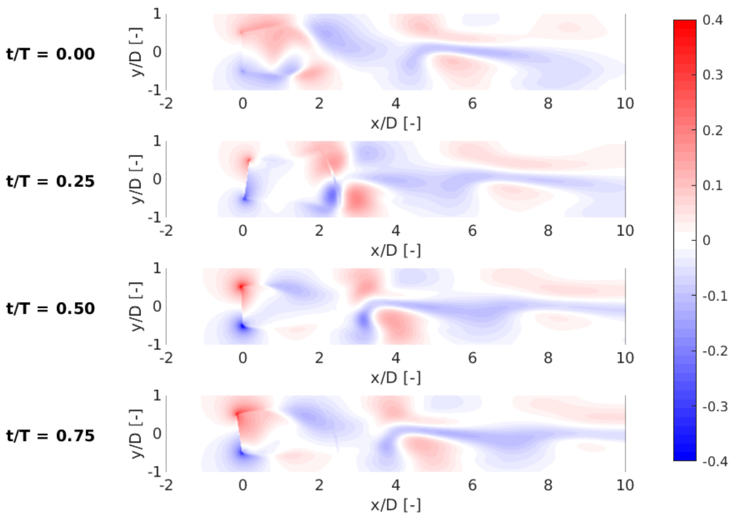

Figure F.19: Contour of normalized Y velocity for Case16 - $C_T = 0.8$; $\Delta C_T = 0.5$; $\theta_p = 8^o$; $\omega_{red} = 1$

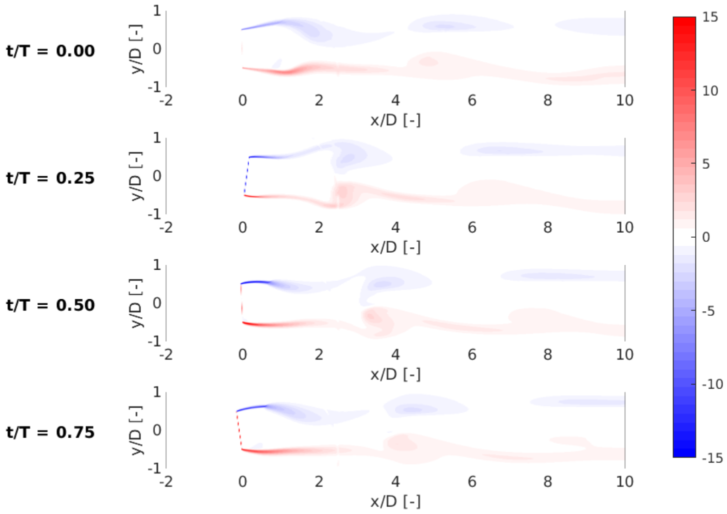

Figure F.20: Contour of normalized Z vorticity for Case16 - $C_T = 0.8$; $\Delta C_T = 0.5$; $\theta_p = 8^o$; $\omega_{red} = 1$

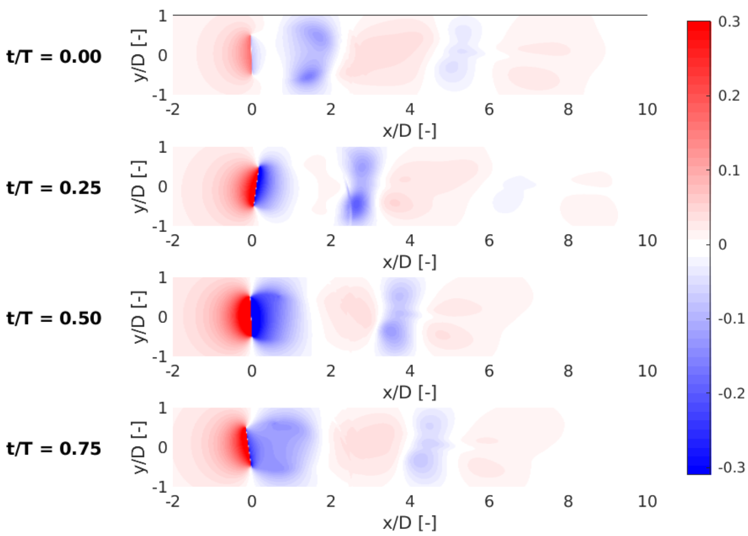

Figure F.21: Contour of normalized pressure for Case16 - $C_T = 0.8$; $\Delta C_T = 0.5$; $\theta_p = 8^o$; $\omega_{red} = 1$

F.7. Case 19

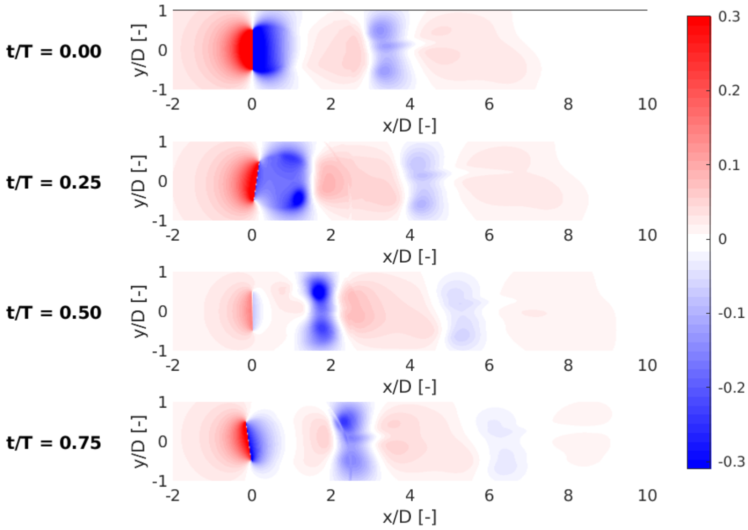

Figure F.22: Contour of normalized pressure for Case19 - $C_T = 0.8$; $\Delta C_T = -0.5$; $\theta_p = 8^o$; $\omega_{red} = 1$

F.8. Case 22

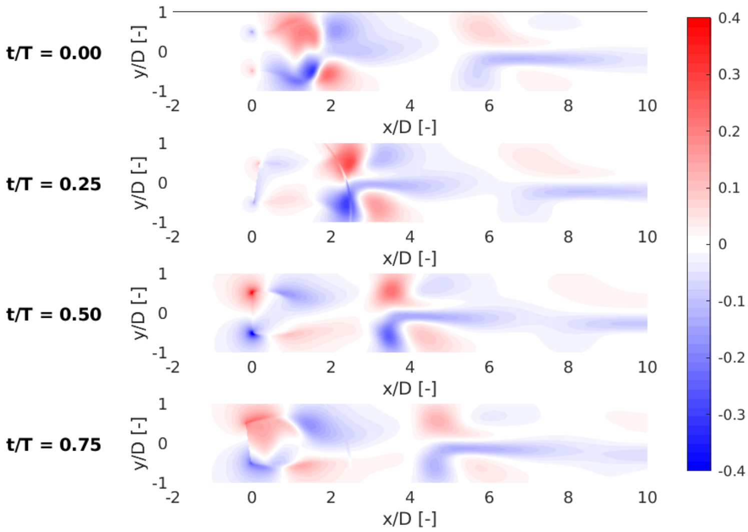

Figure F.23: Contour of normalized Y velocity for Case 22- $C_T = 0.5$; $\Delta C_T = 1$; $\theta_p = 8^o$; $\omega_{red} = 1$

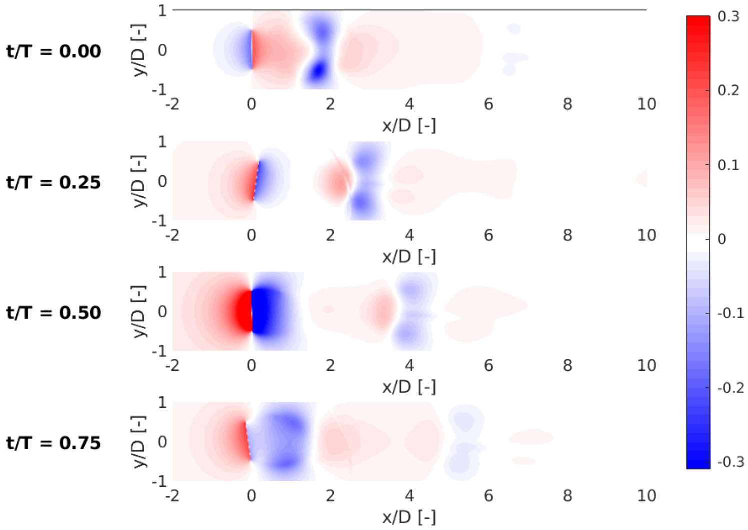

Figure F.24: Contour of normalized pressure for Case 22- $C_T = 0.5$; $\Delta C_T = 1$; $\theta_p = 8^o$; $\omega_{red} = 1$

F.9. Case 23

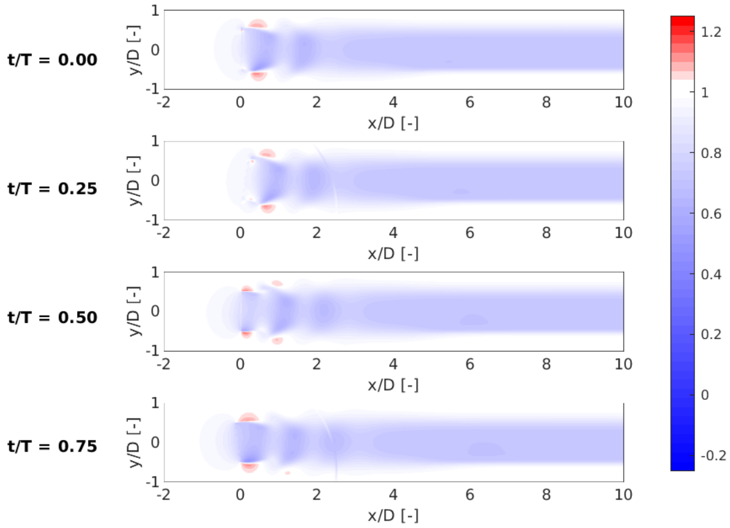

Figure F.25: Contour of normalized X velocity for Case 23- $C_T = 0.5$; $\Delta C_T = 1$; $\theta_p = 8^o$; $\omega_{red} = 5$

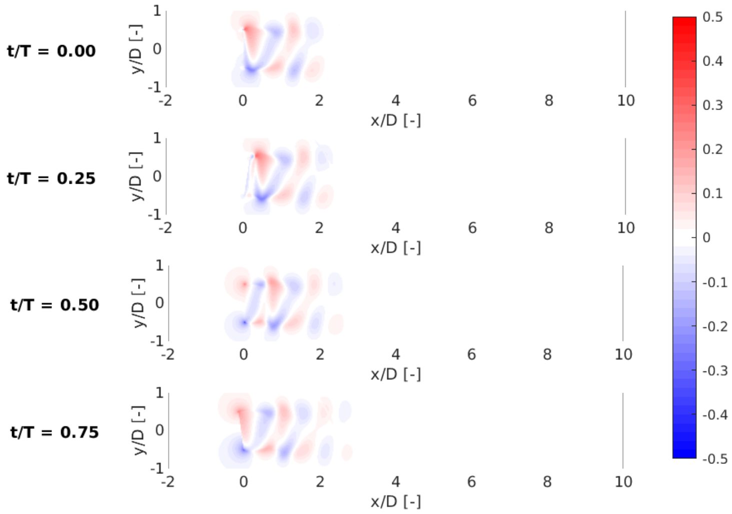

Figure F.26: Contour of normalized Y velocity for Case 23- $C_T = 0.5$; $\Delta C_T = 1$; $\theta_p = 8^o$; $\omega_{red} = 5$

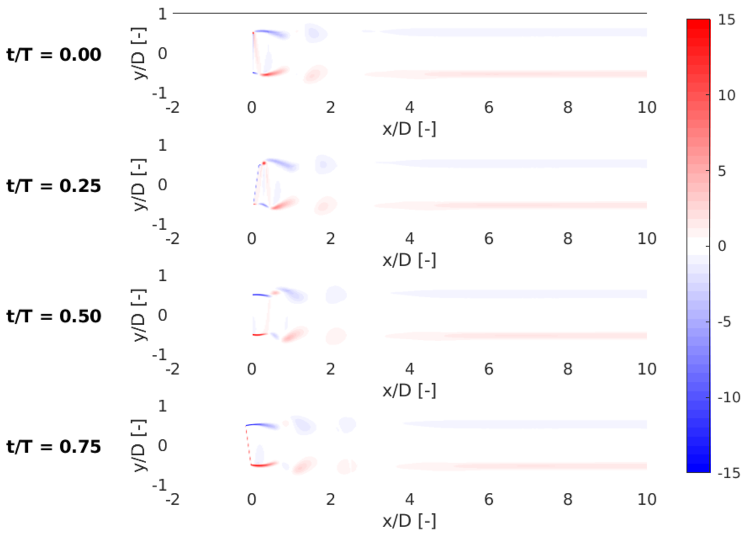

Figure F.27: Contour of normalized Z vorticity for Case 23- $C_T = 0.5$; $\Delta C_T = 1$; $\theta_p = 8^o$; $\omega_{red} = 5$

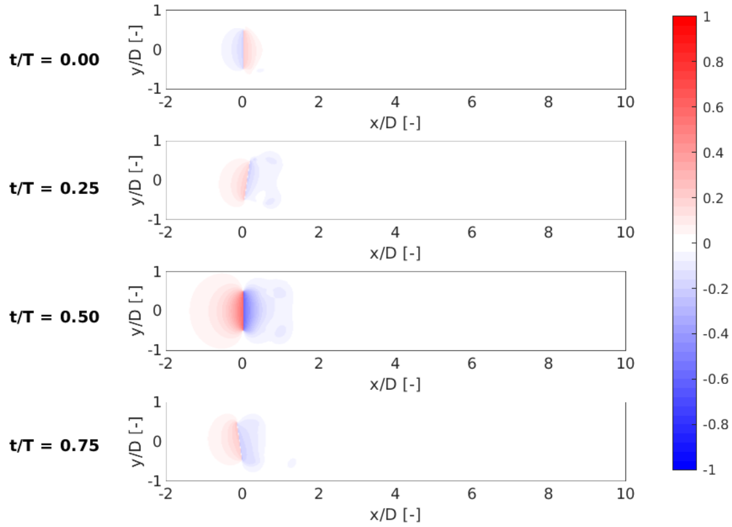

Figure F.28: Contour of normalized pressure for Case 23- $C_T = 0.5$; $\Delta C_T = 1$; $\theta_p = 8^o$; $\omega_{red} = 5$